Technische Universität München
TUM School of Natural Sciences

2D measurements of filament temperatures and densities at the plasma boundary

Daniel Wendler

Vollständiger Abdruck der von der TUM School of Natural Sciences der Technischen Universität München zur Erlangung eines Doktors der Naturwissenschaften (Dr. rer. nat.) genehmigten Dissertation.

Vorsitz: Prof. Dr. Alejandro Ibarra

Prüfende der Dissertation:

1. Priv.-Doz. Dr. Gregor Birkenmeier
2. Prof. Dr. Peter Fierlinger

Die Dissertation wurde am 06.02.2024 bei der Technischen Universität München eingereicht und durch die TUM School of Natural Sciences am 05.06.2024 angenommen.

Technische Universität München
TUM School of Natural Sciences

2D measurements of filament temperatures and densities at the plasma boundary

Author: Daniel Wendler
Supervisor: Priv.-Doz. Dr. Gregor Birkenmeier
Advisor: Dr. Michael Griener

Digital submission date: January 25th, 2024

Abstract

In magnetic confinement fusion, energy is produced by the fusion of light nuclei. To initiate the nuclear reaction, the Coloumb repulsion, resulting from the positive charge of both atomic nuclei, has to be overcome. This is done by heating the fuel to high temperatures. As a consequence, a plasma forms, in which turbulence and other instabilites can emerge. As a result of these processes, coherent structures, called filaments, appear at the plasma boundary, the so called scrape-off layer, where the magnetic field lines are connected to the plasma-facing components. As convective structures, these filaments greatly enhance the transport perpendicular to the magnetic field of particles and energy towards the wall of the fusion device. The transport reduces the power flux to the divertor and redistributes it to different parts, preventing overloading of the most stressed components in future fusion devices. Precise measurements in present-day devices are important to understand the physical mechanisms involved in this filamentary transport. Understanding filaments would allow the design of favorable plasma scenarios.

Fast measurement techniques, such as the thermal helium beam diagnostic, which measures the emitted line intensity from locally injected helium, are needed to measure filaments and their properties. The interaction between the diagnostic response and the filament is studied in this thesis, using synthetic filaments to better understand the measurement signal. This study shows that the intensity perturbation differs in amplitude and shape from the underlying filament, and is mainly influenced by the filament density. Based on the collisional radiative model used for this study, a reconstruction algorithm is implemented that gains the filament electron temperature, density, and size from an input intensity.

This algorithm reconstructs filament properties from conditionally averaged two-dimensional experimental data, showing a relative perturbation amplitude for the electron temperature and density on the order of 70 %. Analysis of a time series for the first time done in the co-moving frame of the filament, shows that the temperature and density values of the filament decrease with time. By relating this decrease to theoretical models, it is found that the temperature decays via parallel heat conduction in the given scenario. For the density, the decay is explained by convective transport parallel to the magnetic field. In addition to the averaged filaments, individual filaments are analyzed. The mean value of the individual filaments is for the temperature and position consistent with the conditional averaging result.

Zusammenfassung

Bei der Fusion mit magnetischem Einschluss wird Energie durch die Verschmelzung leichter Atomkerne erzeugt. Um die Kernreaktion in Gang zu setzen, muss die Abstoßung der beiden positiv geladenen Kerne überwunden werden. Dies geschieht durch Erhitzen des Brennstoffs auf hohe Temperaturen, wodurch ein Plasma entsteht, in welchem Turbulenzen und andere Instabilitäten auftreten können. Als Folge der Vorgänge bilden sich am Rand des Plasmas kohärente Strukturen, die Filamente genannt werden. Filamente sorgen für Konvektion und verstärken den Transport von Teilchen und Energie senkrecht zum Magnetfeld in Richtung der Wand erheblich. Dieser Transport reduziert den Wärmefluss zum Divertor und verteilt ihn auf einen größeren Wandbereich, um eine Überlastung der am stärksten belasteten Komponenten in zukünftigen Fusionsanlagen zu vermeiden. Genaue Messungen in heutigen Fusionsanlagen sind wichtig, um die physikalischen Mechanismen des Filamenttransports zu verstehen. Ein besseres Verständnis würde es ermöglichen, daraufhin optimierte Plasmaszenarien zu entwerfen.

Die Messung von Filamenten und deren Eigenschaften erfordert schnelle Messmethoden, wie die Heliumstrahldiagnostik, bei welcher die Intensität der von lokal eingeblasenem Helium emittierten Spektrallinien gemessen wird. In dieser Arbeit wird die Wechselwirkung zwischen dem Messsignal und Filamenten untersucht, wobei zunächst synthetische Filamente zum besseren Verständnis verwendet werden. Die Ergebnisse zeigen, dass sich die Intensitätsstörung in Amplitude und Form vom zugrunde liegenden Filament unterscheidet und hauptsächlich von der Filamentdichte beeinflusst wird. Basierend auf dem in dieser Studie verwendeten Stoß-Strahlungsmodell wird ein Rekonstruktionsalgorithmus implementiert, der die Temperatur, Dichte und Größe der Filamente aus den Intensitäten bestimmt.

Der Algorithmus rekonstruiert Filamenteigenschaften aus konditionell gemittelten experimentellen Daten, wobei gezeigt wird, dass die Elektronentemperatur und -dichte eine relative Störamplitude in der Größenordnung von 70 % haben. Die Analyse eines Zeitintervalls, die zum ersten Mal im mitbewegenden System des Filaments durchgeführt wurde, zeigt, dass die Temperatur und Dichte des Filaments mit der Zeit abnehmen. Setzt man dies mit analytischen Modellen in Relation, stellt man fest, dass die Temperatur in dem gegebenen Szenario durch parallele Wärmeleitung abnimmt. Für die Dichte wird der Abfall durch konvektiven Transport parallel zum Magnetfeld erklärt. Zusätzlich zu den gemittelten Filamenten werden auch einzelne Filamente analysiert, deren Mittelwert für die Temperatur und Position konsistent mit dem konditionell gemittelten Ergebnis ist.

Contents

1. Introduction

1.1. Nuclear fusion

Climate change severely affects human and natural habitats, caused by increased greenhouse gases in the atmosphere such as CO2 [1]. To combat and mitigate climate change, CO2-neutral energy sources are needed. At the same time, there is an increasing energy demand [2].

One possible energy source for the future is nuclear fusion. It is based on nuclear reactions in which the difference in binding energy between products and reactants releases energy. This binding energy per nucleon is displayed in Figure 1.1 and shows a maximum of the binding energy around ^{62}Ni [3].

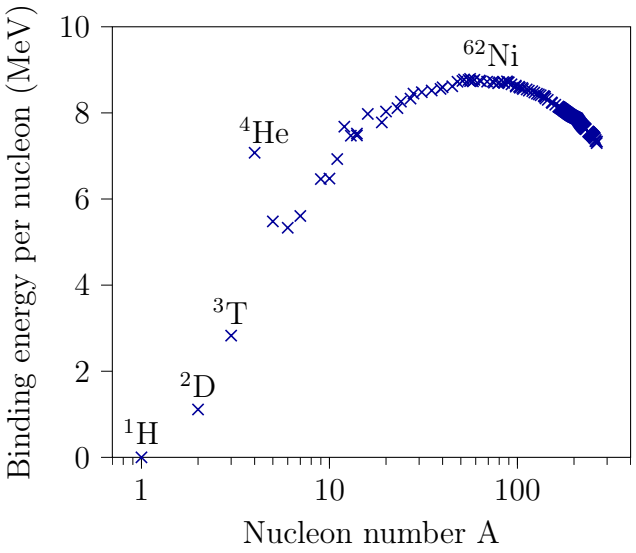

Figure 1.1.: The binding energy per nucleon [3]. By fusion of light elements, the binding energy per nucleon increases, leading to an energy release of the reaction. In contrast, very heavy elements can release energy by splitting into lighter elements (nuclear fission). Both processes are only possible up to the maximum of the binding energy around ^{62}Ni, where no more exothermic reactions are possible.

The consequence of the mass dependency of the binding energy behavior is that heavier nuclei can release energy by splitting into two smaller nuclei (nuclear fission). Lighter elements can release energy by fusing two nuclei (nuclear fusion).

The most promising reaction for energy production by fusion on earth is the deuterium (^{2}D or ^{2}H) and tritium (^{3}T or ^{3}H) fusion. Both are heavy isotopes of hydrogen, with ^{2}D having one neutron and ^{3}T having two neutrons in addition to the proton. The reaction, given as

$$^2\mathrm{D}^+ + \ ^3\mathrm{T}^+ \rightarrow \ ^4\mathrm{He}^{2+} + \mathrm{n} + 17.6\,\mathrm{MeV},$$

has a significantly higher energy release and reaction cross section compared to other fusion reactions [4]. Deuterium occurs in the natural isotope mixture of water, while the radioactive tritium shall be bred from lithium in the fusion reactor itself [5, 6].

To fuse two light nuclei, the Coulomb barrier of the positively charged nuclei, which is effectively lowered by the tunnel effect [7], must be overcome. Very high temperatures[1] are required to overcome this barrier, so the reaction can only take place in plasmas.

To achieve self-sustaining fusion, the energy losses of the plasma must be compensated by the fusion power generated by the plasma. The Lawson criterion describes this condition [10] and is given as the following triple product[2]

$$n \cdot T_\mathrm{i} \cdot \tau_\mathrm{E} \geq 3 \cdot 10^{21}\,\mathrm{keV\,s\,m^{-3}}, \tag{1.1}$$

consisting of the density n, the ion temperature T_i and the energy confinement time τ_E. The energy confinement time is the ratio between the energy content of the plasma and its energy loss.

Due to plasma temperatures on the order of several keV[3], fusion plasma cannot be confined in solid-state vessels, as materials cannot withstand these temperatures. Therefore, the fusion conditions for a plasma can be preserved by three different confinement processes:

- Gravitational confinement:
  In stars like our Sun, gravity confines the plasma, reducing the energy and particle losses of the plasma and preserving the fusion conditions in the core [11, 12].

[1] Proof for an alternative fusion concept, called cold fusion, has not yet been found to have a positive energy output [8, 9].

[2] The value of the triple product depends on the nuclear reaction and is given here for the ^{2}D + ^{3}T reaction.

[3] In magnetic fusion, temperatures are measured in electronvolts (eV), which are related to thermal energy by the Boltzmann constant. 1 eV corresponds to 11 605 K.

- Inertial confinement:
  Small pellets are compressed to a tiny fraction of their initial size for inertial fusion, which ignites the fusion. The concept is that the fusion reaction is so fast that it burns the fuel before the plasma begins to expand [13, 14]. The inertia of the particles, therefore, achieves the fusion conditions. Experiments at the National Ignition Facility (NIF), the largest inertial confinement fusion facility, have achieved a record fusion yield, exceeding the Lawson criterion [15, 16].

- Magnetic confinement:
  Magnetic confinement uses magnetic fields to confine the plasma, creating closed particle orbits for the plasma species. The leading concepts are the stellarator [17, 18, 19] and the tokamak.

All experiments described in this thesis were carried out on the ASDEX Upgrade tokamak. Therefore, the tokamak concept is described in more detail in Section 1.2.

1.2. Tokamaks

The most frequently used and advanced concept for magnetic confinement is the tokamak. Igor Tamm and Andrey Sakharov developed it in the Soviet Union, and it is the acronym for "Toroidalnaya Kamera i Magnitnaya Katushka" (Toroidal Chamber and Magnetic Coil) [20, 21, 22, 23].

1.2.1. Basic magnetic field geometry

In principle, the tokamak consists of two magnetic fields. External coils generate a toroidal magnetic field B_ϕ. In addition, a transformer induces a voltage that drives the plasma current I_p, also in the toroidal direction. Due to the excellent electric conductivity of the plasma, only a few volts are sufficient to drive a plasma current in the range of several megaamperes. This plasma current generates a poloidal magnetic field B_θ, which is weaker than the toroidal field. The combination of both magnetic fields results in screwed magnetic field lines. The composition of the magnetic field is displayed in figure 1.2.

Following a magnetic field line in the tokamak, it will return to its point of origin after a certain periodicity. This periodicity is used to describe the relative relationship of the two magnetic fields using the safety factor q_s [25], which is

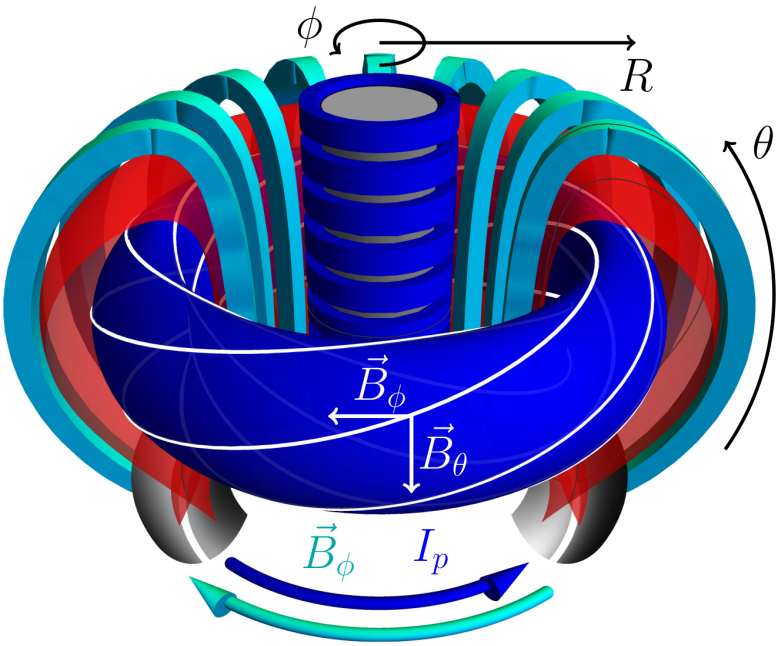

Figure 1.2.: Schematic figure of a tokamak. The magnetic field is composed of the toroidal field B_ϕ and the poloidal field B_θ. The major radius from the tokamak center to the magnetic axis R and the toroidal angle ϕ and poloidal angle θ are indicated. The blue arrow indicates the plasma current I_p. Image from [24]

described in the approximation of a linear tokamak as

$$q_s = \frac{\text{number of toroidal turns}}{\text{number of poloidal turns}} = \frac{a}{R}\frac{B_\phi}{B_\theta}. \tag{1.2}$$

The minor radius a describes the radius of the magnetic axis to the Last Closed Flux Surface (LCFS), and the major radius R corresponds to the radius from the toroidal axis, sitting at the torus center, to the magnetic axis. A plasma cross-section, showing these quantities, can be seen in Figure 1.3. The LCFS separates the confined region, where the magnetic field lines close with a certain periodicity, and the scrape-off layer (SOL), where the field lines hit the plasma-facing components (PFC) after a certain distance. All three quantities are displayed in Figure 1.3a. The physics in the scrape-off layer is further explained in section 2.1.

For a pressure gradient perpendicular to the magnetic field lines, the equilibrium condition in the confined region is given as [26]

$$\nabla p = \vec{j} \times \vec{B}, \tag{1.3}$$

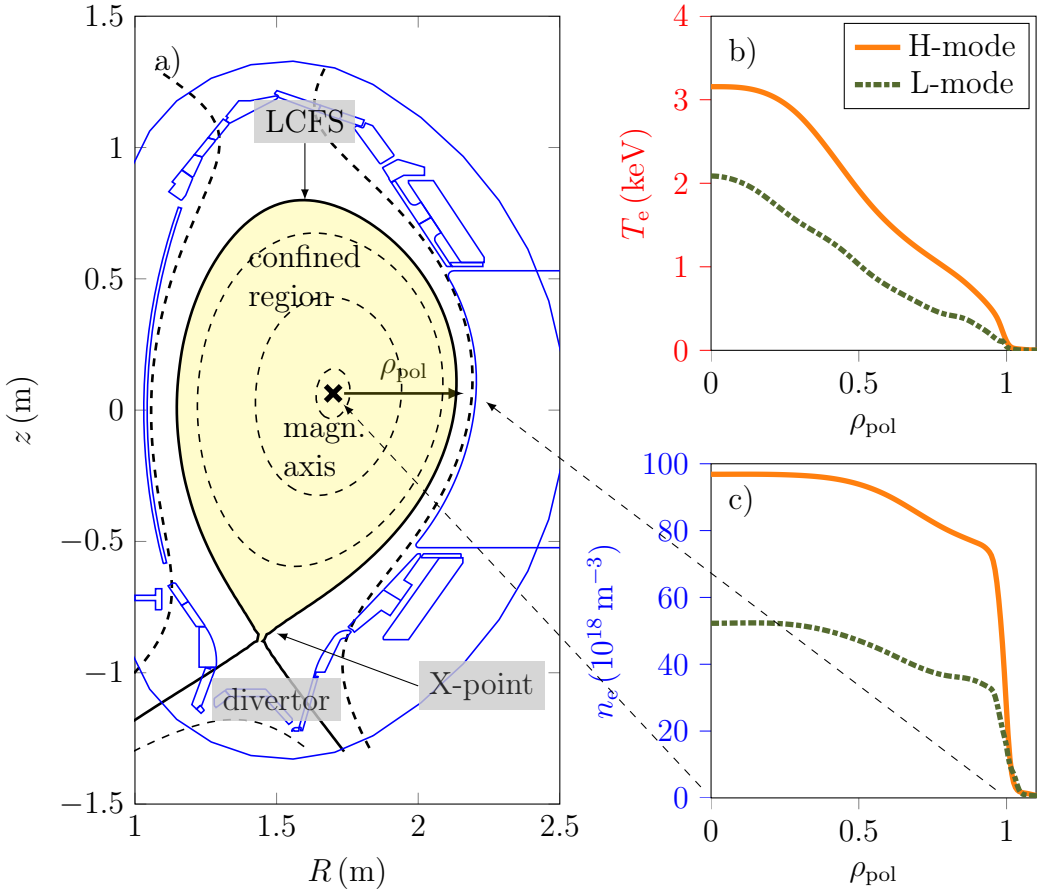

Figure 1.3.: The figure shows in a) the poloidal cross-section of the magnetic equilibrium (#40425, $t = 2.0\,\mathrm{s}$) by displaying several flux surfaces (dashed lines). In b), electron temperature of an H-mode (#36300, $t = 3.6\,\mathrm{s}$) and an L-mode (#34918, $t = 3.0\,\mathrm{s}$) discharge are compared. The analog comparison for the electron density can be seen in c).

with the current density j and the total magnetic field $\vec{B}$. As a result, the pressure p is constant along each magnetic field line, resulting in concentric magnetic flux surfaces with constant pressure. Based on the poloidal magnetic flux Ψ, the normalized poloidal magnetic flux coordinate (ρ_{pol}) is defined as

$$\rho_{\mathrm{pol}} = \sqrt{\frac{\Psi - \Psi_{\mathrm{magn.axis}}}{\Psi_{\mathrm{LCFS}} - \Psi_{\mathrm{magn.axis}}}}, \tag{1.4}$$

with $\Psi_{\mathrm{magn.axis}}$ the poloidal flux at the magnetic axis and Ψ_{LCFS} the flux at the LCFS. By definition, the normalized poloidal magnetic flux coordinate is 0 at the magnetic axis and 1 at the LCFS.

A magnetic X-point can be created through additional poloidal field coils, leading to the divertor configuration. In the divertor configuration, the LCFS is also called separatrix. A plasma cross-section with a divertor configuration is displayed in Figure 1.3a.

Besides the magnetic configuration, tokamak plasmas can be categorized into different operation regimes. The two most important plasma operation regimes are the low-confinement mode (L-mode) and high-confinement mode (H-mode) [27]. Initially, they have been heuristically divided by the energy confinement time τ_E, which is about a factor of 2 higher for H-mode than for L-mode [28]. The transition from L-mode to H-mode is achieved by increasing the heating power above a critical threshold [29, 30]. The access to H-mode is faciliated in a diverted plasma, and, consequently, the H-mode was discovered in a diverted plasma [31]. The comparison between temperature and density profiles in L-mode and H-mode can be seen in Figure 1.3b and 1.3c.

1.2.2. ASDEX Upgrade

All experiments for this thesis were performed at ASDEX Upgrade (AUG). The tokamak was built at the Max-Planck-Institut für Plasmaphysik in Garching, Germany, and is the successor of ASDEX (Axial Symmetric Divertor EXperiment) [32]. ASDEX Upgrade has been in operation since 1991 and performs typically a nine-month experimental campaign each year, performing 2-3 experimental days per week. To date, a total of 41570 discharges have been performed at AUG, which are identified by a sequential shot number, denoted as "#shot number".
The technical parameters of AUG are given in Table 1.1.

Table 1.1.: Key parameters of ASDEX Upgrade [33, 34]

NBI heating	$P_{\mathrm{NBI}} =$	20 MW
ECRH heating	$P_{\mathrm{ECRH}} =$	6 MW
ECRH heating	$P_{\mathrm{ICRH}} =$	6 MW
max. toroidal B field	$B_\phi =$	3.1 T
max. current	$I_\mathrm{p} =$	1.6 MA
max. discharge time	$t_{\mathrm{max}} =$	10 s
major plasma radius	$R =$	1.65 m
minor plasma radius	$a =$	0.5 m
energy confinement time	$\tau_E =$	< 0.2 s

The heating systems for AUG are the neutral beam injection (NBI), which deliver a power of up to 20 MW [35, 34]. In addition, the electron cyclotron

resonance heating (ECRH) and ion cyclotron resonance heating (ICRH) heating systems deliver a power of 6 MW each [34]. Due to power supply restrictions, the maximum combined heating power is limited to 27 MW [34].
The toroidal magnetic field has a strength of up to 3.1 T, with the toroidal field generated by 16 water-cooled copper coils. The heat up of these coils sets the maximum pulse length to 10 s. The maximum plasma current is limited to $I_p = 1.6$ MA. The plasma has a major radius R of 1.65 m, and a minor horizontal radius a of 0.5 m. Since 2007, all plasma-facing components (PFC) are made from tungsten [36]. The main plasma ions are deuterium, being replaced by hydrogen or helium usually for a few weeks per campaign. Because of its radioactivity, tritium cannot be used, so no significant fusion power is generated at AUG. Currently, the Joint European Torus (JET) is the only tokamak that operates with deuterium and tritium [37].

1.3. Scope of this thesis

A common feature in both operation regimes, the L-mode and H-mode, is the presence of filaments. Filaments are structures created by different processes, appearing in all known plasma regimes [38, 39, 40].

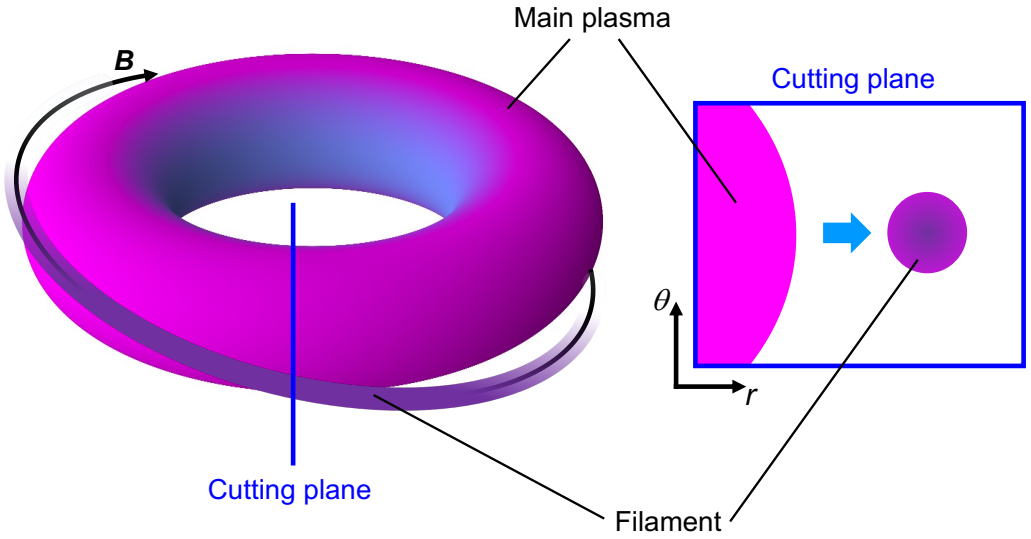

Figure 1.4.: A filament along a magnetic field line is displayed for a schematic torus. The size of the poloidal cross-section is small compared to the extension along the magnetic field line. Image from [41]

These structures are aligned with the magnetic field and appear in the SOL, which can be seen in Figure 1.4. The extension along the magnetic field line is much larger than the size perpendicular to the magnetic field. Filaments have a higher temperature and density than the background, which together with the radial propagation of the filament results in convective transport. This filamentary heat transport distributes the heat load to different plasma-facing components. This can reduce the heat load in the divertor to an acceptable level, but there is a risk of overloading other components. Filaments and their properties are described in more detail in Chapter 2. Accurate measurements of filament temperature, density, and velocity are required to predict filament heat fluxes. This is done with the thermal helium beam diagnostic, which is explained in Chapter 3. To better understand the diagnostic response on the filaments, synthetic filaments are studied in Chapter 4. The reconstruction of synthetic filaments, comparing a static and a dynamic collisional radiative model, is performed in Chapter 5. In Chapter 6, the results of experimentally measured filaments are compared with analytical models of scrape-off layer transport in order to asses a potential impact of filaments on wall components. Finally, the thesis concludes with a summary and outlook.

2. Filaments in the scrape-off layer

In this chapter, the scrape-off layer is briefly introduced, in which the filaments appear. This focuses, besides the filamentary transport, on the steady-state transport. Both transport processes must be balanced to prevent heat overload for future fusion devices. Filaments and their properties are then described in more detail. This includes their formation, their propagation, and phenomena related to filaments.

2.1. Transport and heat exhaust in the scrape-off layer

The scrape-off layer (SOL) is the region outside the LCFS. Unlike the confined region, the magnetic field lines in the SOL are open, ending at plasma-facing components (PFC). A schematic plasma cross section is shown in Figure 2.1. We define the connection length L_c as the distance along a 3D magnetic field line from a given upstream point (in red) to any material surface, here the outer target. The upstream position is by defintion the location where the particles start to flow towards the target. For simplicity, the upstream position is often chosen to be at the low field side (LFS) (region radially outward from the magnetic axis, which has a weaker magnetic field) midplane (horizontal plane at the position of the magnetic axis). To avoid these definitional uncertainties, we refer to twice the connection length as the length of the magnetic field connecting the inner to the outer target. This leads to the following definition [42]:

$$2L_\mathrm{c} \approx 2\pi R\sqrt{\frac{1+\kappa_\epsilon^2}{2}}q_\mathrm{s}, \tag{2.1}$$

with the ellipticity/elongation of the poloidal cross section κ_ϵ, the safety factor q_s and the major radius R. The SOL can be seen as a contact layer between the confined region and the PFC. Therefore, the heat exhaust is regulated through the SOL, as well as the impurity dynamics and the neutral particle fuelling [43].

The plasma in the confined region is heated by auxiliary heating sources and the intrinsically generated fusion power. The resulting heat is transported outwards,

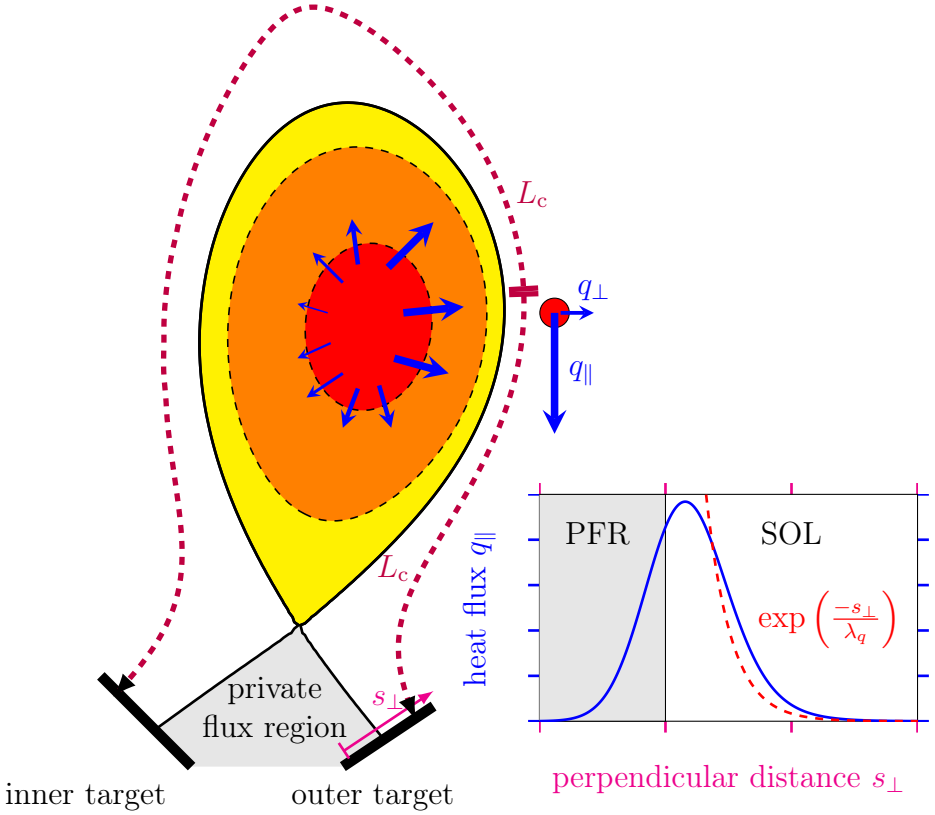

Figure 2.1.: Schematic view of the power fluxes in the confined plasma and the SOL. From the confined region (yellow to red region), heat is transported outwards. In the SOL, the heat is dominantly transported towards the divertor, resulting in an exponential profile for the target heat flux. A heat flux profile along the target coordinate $s_\perp$ is shown on the right. The connection length L_c is defined as the distance from the upstream position (red point) along the magnetic field line to the target. The private flux region (PFR) is located between the inner and outer divertor and below the X-point, containing no hot plasma.

being reduced by radiative losses. This resulting power goes through the SOL to the divertor target and other PFCs. A schematic drawing of the power fluxes can be seen in Figure 2.1.

For a stable plasma, the heat flux can be divided into a steady (diffusive) and a transient (convective) part. The transient part is dominated by the filaments, discussed in the following sections. The SOL is divided into a near-SOL, the region between the separatrix and a profile decay length, which is introduced in Section 2.1.2. Further out is the far-SOL. The near-SOL is dominated by the steady

transport, while the far-SOL is dominated by the filamentary transport.

2.1.1. Steady-state heat fluxes

For the steady heat flux, the particle and power flux parallel to the magnetic field dominates the weaker perpendicular transport. Therefore, we focus on the parallel heat flux in the following. The parallel heat flux can be described analytically by the two-point model, which uses one-dimensional analytical formulas to describe the profiles along the magnetic field lines between the target and an upstream position. The model starts with the Spitzer-Haerm heat flux for the electron conduction, given as [43, 44]

$$q_{\parallel}^{\text{cond.}} = -\kappa_0 T_{\text{e}}^{5/2} \frac{dT_{\text{e}}}{ds_{\parallel}}. \tag{2.2}$$

Here $\kappa_0 T_{\text{e}}^{5/2}$ is the thermal conductivity, with the coefficient $\kappa_{0,\text{e}} = 2000\,\text{W}\,\text{m}^{-1}\,\text{eV}^{-7/2}$ for the electrons and $\kappa_{0,\text{i}} = 60\,\text{W}\,\text{m}^{-1}\,\text{eV}^{-7/2}$ for the ions. The parallel distance along the field line is $s_{\parallel}$, being 0 at the upstream position and L_{c}, the connection length, at the target position.

Equating the heat flux with the ratio of the total heat flux P_{SOL} divided by the SOL cross-section $A_{q,\parallel}$, $q_{\parallel} = \frac{P_{\text{SOL}}}{A_{q,\parallel}}$, one can integrate the temperature along the field line, which results in

$$T\left(s_{\parallel}\right) = \left[T_{\text{t}}^{7/2} + \frac{7}{2}\frac{\left(P_{\text{SOL}}/A_{q,\parallel}\right)\ \left(L_{\text{c}} - s_{\parallel}\right)}{\kappa_0}\right]^{2/7}, \tag{2.3}$$

with the target temperature T_{t}. This regime is called *conduction limited* and is a simple solution of the two-point model [43].

Besides conductive transport, heat is also transported via convection. No pressure gradient is required for this type of transport. The parallel heat flux reads in the convective case [43]

$$q_{\parallel}^{\text{conv.}} = \frac{5}{2} T_{\text{e}} n_{\text{e}} v_{\text{e}}. \tag{2.4}$$

Here the electrons move with the velocity v_{e}, which is typically assumed as the ion sound speed $c_{\text{s}} = \sqrt{\frac{T_{\text{e}} + \gamma T_{\text{i}}}{m_{\text{i}}}}$ using the adiabatic coefficient γ. For 1D cases discussed later, γ is chosen to be 3 (for f degrees of freedom, $\gamma = \frac{2+f}{f}$). In contrast to the conduction case described in Equations 2.2 and 2.3, the plasma can be regarded as isothermal at a magnetic field line. This regime is called *sheath connected* and typically occurs in a tokamak for low heating powers.

2.1.2. SOL profiles

In addition to the parallel heat flux, weaker transport occurs perpendicular to the flux surfaces. For an assumed purely conductive transport, the power flux perpendicular to the magnetic field reads as

$$q_\perp = n_\mathrm{e}\chi_\perp \frac{dT_\mathrm{e}}{ds_\perp}, \tag{2.5}$$

with the anomalous heat conduction coefficient $K_\perp = n_\mathrm{e}\chi_\perp$ and the perpendicular distance $s_\perp$. This can be used to determine the decay lengths, using a diffusive ansatz with exponentially decaying profiles for the perpendicular temperature and heat flux [45, 46],

$$\begin{aligned} T_\mathrm{e}\left(s_\perp\right) &= T_{\mathrm{e},0} \cdot \exp\left(-s_\perp/\lambda_{T_\mathrm{e}}\right), \\ q_\parallel\left(s_\perp\right) &= q_{\parallel,0} \cdot \exp\left(-s_\perp/\lambda_{q_\parallel}\right). \end{aligned}$$

Both, temperature and heat flux are parametrized with a decay length λ_{T_e} and $\lambda_{q_\parallel}$ and an offset value of $T_{\mathrm{e},0}$ and $q_{\parallel,0}$, respectively. A $q_\parallel$ profile with this exponential parametrization can be seen in Figure 2.1. The decay of the parallel heat flux profile depends on the perpendicular transport, which is related to the power fall-off length $\lambda_{q_\parallel}$ as

$$\lambda_{q_\parallel} = L_\mathrm{c}\sqrt{e n_\mathrm{e}\chi_\perp/\kappa_{0,e}T_\mathrm{e}^{5/2}}. \tag{2.6}$$

This leads in the *conduction limited* case to the following relation [47, 43]:

$$\lambda_{T_\mathrm{e}} = \frac{7}{2}\lambda_{q_\parallel}. \tag{2.7}$$

In realistic tokamak geometry, the decay lengths λ_{T_e} and $\lambda_{q_\parallel}$ need to be multiplied with a flux expansion factor f_x, counting for the change in poloidal separation of different flux surfaces. In L-mode and H-mode experiments, good agreement for the analytical ratio between the temperature and power decay lengths has been found [47, 48]. The heat flow in the SOL flowing from the midplane to the target comes into contact with the private flux region (PFR) in the divertor, see Figure 2.1. There is cold plasma in the PFR, so heat diffuses from the SOL into the PFR. This diffusion affects the heat flux profile at the target, resulting in the following heat flux profile [49]

$$q_\parallel\left(s_\perp\right) = \frac{q_{\parallel,\mathrm{sep}}}{2}\exp\left(\left(\frac{S}{2\lambda_{q_\parallel}}\right)^2 - \frac{s_\perp}{\lambda_{q_\parallel}}\right)\mathrm{erfc}\left(\left(\frac{S}{2\lambda_{q_\parallel}}\right) - \frac{s_\perp}{S}\right).$$

$q_{\parallel,\mathrm{sep}}$ is the normalization for the heat flux, and the S-Parameter is a measure of the diffusion. To compare the profiles at the midplane and in the divertor, $\lambda_{q_\parallel}$ must be multiplied by the flux expansion factor. Here erfc is defined as $erfc = 1 - \mathrm{erf}$. An exemplaric profile is displayed in blue in Figure 2.1.

2.1.3. Heat exhaust

The power decay length $\lambda_{q_\parallel}$ has been related to global plasma parameters, using a multi-machine scaling [49], resulting in power fall-of lengths in the order of mm and stationary peak power fluxes of up to $10\,\mathrm{MW\,m^{-2}}$ for the International Thermonuclear Experimental Reactor (ITER) [50, 51]. Due to the high heat fluxes, the surface of the PFC heats up, posing the risk of melting and increased sputtering, seriously damaging the material and increasing erosion [52, 53]. The heat flux must be kept below the maximum heat flux of about $10\,\mathrm{MW\,m^{-2}}$ under all operation conditions, which is still a challenge.

This heat exhaust challenge remains to be fully solved for future devices [54]. Reducing the heat flow into the divertor is therefore a major effort. In the confined region, higher radiation can decrease the heat flow into the SOL, as in the X-Point radiator (XPR) regime [55]. The core radiation in this regime, and in any other, must be carefully controlled since radiation inside the confined region reduces the fusion power, making it more difficult to reach the Lawson criterion (see eq. 1.1) [56]. In the SOL, the maximum heat load can be reduced by increasing the deposition area through geometric effects. On the other side, the heat flux can be reduced in the SOL on its parallel way to the divertor. One mechanism reducing the divertor power load is the detachment, where a layer of neutrals in front of the divertor plates causes recombination and creates radiation, which reduces the heat flux on the targets [57]. Another possibility is to raise λ_q by high filamentary transport, which is further discussed in Section 2.5.

2.2. Filament characteristics

Plasma filaments are coherent plasma structures with a higher density than the surrounding plasma and an independent motion, appearing in the SOL. These structures have only a small expansion perpendicular to the magnetic field ($\approx$ cm) and a large extension along the field lines ($\approx 10\,\mathrm{m}$). A schematic drawing of a filament can be seen in Figure 1.4.

Filaments occur in all plasma regimes and are caused near the separatrix by different processes described in Section 2.3 [38]. In L-mode, filaments are also called "blobs". After formation, filaments move radially outwards, leading to convective particle and energy transport. This radial propagation can be described

by analytical blob models (see section 2.4). Depending on the filament type, filaments reach radial propagation velocities between several hundred to several thousand $\mathrm{m\,s^{-1}}$ [40]. Filaments appear with a mean occurrence rate of 10 Hz to 1000 kHz, depending on the plasma scenario and the creation mechanism [58, 59]. In simulations, it was shown that the size in the poloidal cross-section is restricted due to multiple processes. The Kelvin-Helmholtz instability sets a lower limit for small blobs, while large filaments are prone to curvature-driven instabilities. The most stable blob size is in the order of several ion gyro radii ρ_s [38].

2.3. Filament formation

Depending on the tokamak operating regime, filaments are created by different processes. In the L-mode, one mechanism essential to create blobs is the edge turbulence. These turbulent structures in the confined region evolve over multiple steps into a coherent structure in the SOL, known as a blob [60, 61]. Besides this, a small density perturbation in the SOL can evolve into a comparably large filament due to the conducting-wall instability [60]. Blobs have a relatively small pressure perturbation, resulting in a small magnetic signature [62].

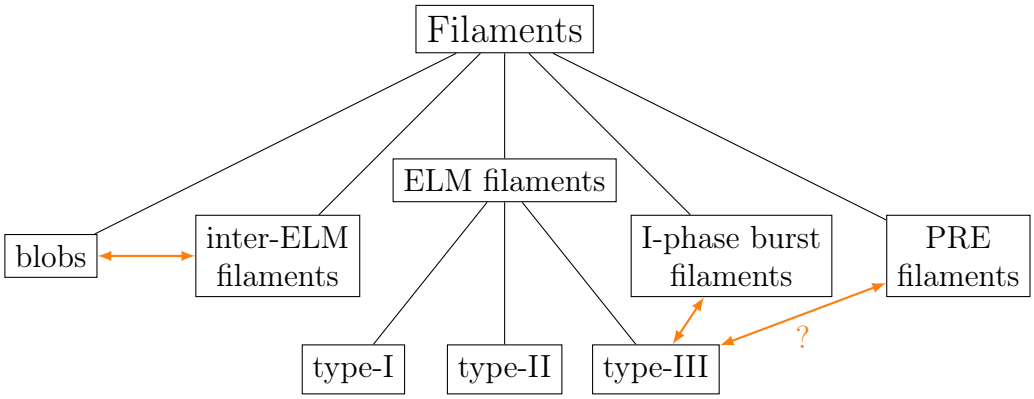

Figure 2.2.: Relations between filament types originating from different mechanisms. Orange arrows indicate a (possible) similarity between different filament types. For PREs and type-III ELMs, many characteristics are similar, besides the power dependency of the filament frequency.

In H-mode, enhanced filamentary transport is created by edge localized modes (ELMs). ELMs are magnetohydrodynamic (MHD) instabilities, going along with a strong magnetic signature, that creates stochastic bursts, with an average repetition frequency in the range of tens of Hz to several hundred Hz [59]. They are phenomenologically classified into three categories, depending on the relation between the repetition frequency and the heating power. Type-I-ELMs have an increasing

frequency with the heating power, while the filament frequency of type-III-ELMs decreases with heating power. In addition, type-III-ELMs have a magnetic precursor. For type-II-ELMs, there is no information about the power dependency of the ELM frequency or precursors, but they only appear at high triangularity and elongation [59].

Since type-II and type-III ELMs cannot always be clearly distinguished, they are often grouped together under the term small ELMs [63, 64, 65]. In comparison to other filaments, ELM filaments, especially that of type-I, are hotter, denser, faster, and larger, which can be seen in the pedestal energy that drops by up to 30 % during an ELM-crash [66, 40]. Due to their high thermal energy, type-I ELMs likely will overload the wall materials in larger tokamaks, resulting in erosion by sputtering and melting [52, 54]. Accordingly, scenarios without type-I ELMs are needed for future fusion power plants [67, 63]. From a theoretical understandying, type-I ELMs are explained by peeling-ballooning modes [68], while small ELMs might be explained by a ballooning unstable region close to the separatrix [69]. In addition to ELM-filaments, inter-ELM-filaments are observed in H-mode, which are more similar to blobs [39, 40, 70].

In the I-mode [71, 72], a regime consisting of an L-mode density profile and an H-mode temperature profile, an additional mechanism for the filament formation is observed . At high heating powers, pedestal relaxation events (PREs) appear, causing intermittent bursts, ejecting filaments, and leading to a loss of the pedestal energy in the order of 1 %. These PREs are presumably linked to the presence of the weekly coherent mode (WCM), an edge instability, occurring at several kHz and with a perpendicular wave number of the structure in the order of several cm^{-1} [73]. Besides in I-mode, the WCM is also observed in L-mode [73, 74], but there its implication on filaments is so far unclear.

The I-phase is a regime that appears close to the transition from L-mode to H-mode (L-H transition) [75, 76, 30]. At the plasma edge, magnetic fluctuations are measured, going along with bursts as a result of temporary flattened temperature and density profiles around the separatrix [77, 75]. These I-phase bursts can appear very periodic or intermittently [78, 41] and are similar to type-III ELMs [79, 30].

A graph showing different types of filaments associated with different formation processes is displayed in figure 2.2. Orange arrows indicate similarities, as mentioned above, between various processes in the graph. When comparing PREs and type-III ELMs, they have many similar characteristics, but differ in the power dependency of the occurrence frequency [80].

2.4. Analytical models for filament propagation

For the theoretical understanding of filaments, analytical models have been developed in order to describe the filament velocity depending on the filament size and local plasma parameters [81]. These models describe the filament by an internal polarization, which causes the convective motion by means of the $E \times B$ drift. To explain this polarization and how it is balanced, different processes are taken into account within the models. A schematic drawing of the filament with different current closure schemes, which will be discussed in the following, can be seen in figure 2.3.

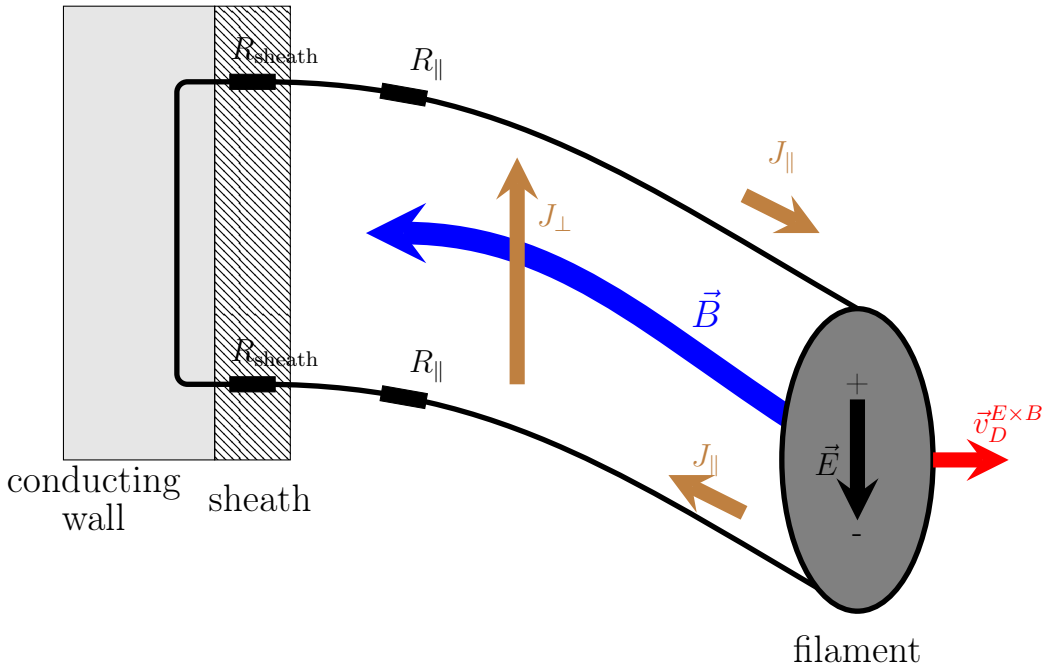

Figure 2.3.: The blob equivalent circuit, describing the orientation of the electric field and different balancing mechanisms. The filament potential causes an $E \times B$ drift, moving the filament perpendicular to the magnetic field. R_{sheath} is the resisitivity in the plasma sheath in front of the PFC, and $R_{\parallel}$ is a resisitivity parallel to the magnetic field line. $J_{\parallel}$ and $J_{\perp}$ are the parallel and perpendicular electric currents.

2.4.1. Creation of the polarization

All models start with the charge conservation, given inside the filament as

$$-\nabla \cdot \vec{J_\perp} = \nabla_\parallel J_\parallel.$$

The generation of perpendicular current, denoted as $J_\perp$, within the filament occurs due to charge separation resulting from charge-separating drifts (see appendix A.1). These drift motions are typically attributed to either the curvature and gradient of the magnetic field, known as the curvature and ∇B drift, arising from the magnetic field geometry, or the diamagnetic drift, resulting from the pressure gradient in the filament.

These processes can be expressed as a unified force density vector $\vec{F}$. This force density is subsequently incorporated into the polarization equation, as described in reference [82]:

$$\nabla \frac{d}{dt}\left(\frac{nMc^2}{B^2}\nabla_\perp \Phi\right) = \nabla_\parallel J_\parallel + \frac{c}{B}\vec{b} \cdot \nabla \times \vec{F}. \tag{2.8}$$

Here M is the ion mass, n is the plasma density, B is the magnetic field strength, c is the speed of light, and $\vec{b} = \frac{\vec{B}}{B}$ is the orientation of the magnetic field. The filament potential Φ is typically a dipole describing a vertical charge separation, which results in a $\vec{E} \times \vec{B}$ drift. For the potential Φ it is balanced by the closure of the parallel currents, while the external force $\vec{F}$ increases the potential by its charge separation drifts.

2.4.2. Balancing of the filament potential

The filament potential Φ is balanced over the parallel currents $J_\parallel$, which closes the set of equations. For these closure schemes, the three important cases are the inertial regime, the sheath limited/sheath dissipation regime, and the collisional regime [83, 82, 84].

- In the *inertial regime*, the parallel currents are so weak that they are neglected, whereby the polarization is only balanced by the inertia term of the polarization equation, which manifests as the ion polarization drift.
- In the *sheath dissipation regime*, the polarization is balanced by the currents flowing parallel to the magnetic field lines, leading to a shorting in the wall. The parallel currents in this case are limited by the resistance of the plasma sheath R_{sheath}.
- In the *collisional regime*, the parallel resistivity is increased due to collisions, which exceeds the sheath resistance. The polarization is balanced by the parallel resistivity.

All three current closure processes can be seen in figure 2.3. Most of the filament diagnostics are capable of measuring the velocity and size of filaments to high accuracy. Therefore, the filament models are used to determine a theoretical relation between both measured quantities. For the inertial regime, the relation between velocity and size reads [83]

$$\left|\frac{v_b}{c_s}\right| = \sqrt{(1+\tau_\mathrm{i})\,\frac{\delta_b}{R}\tilde{P}_\mathrm{e}}, \tag{2.9}$$

with the radial blob velocity v_b , the ion sound speed c_s, the major radius R, normalized filament pressure $\tilde{P}_\mathrm{e}$, the ion-to-electron temperature ratio τ_i and the filament size δ_b perpendicular to $\vec{B}$.

In the sheath dissipation regime, the relation between the velocity and size results [83]

$$\left|\frac{v_b}{c_s}\right| = (1+\tau_\mathrm{i})\left(\frac{L_\mathrm{c}}{R}\right)\left(\frac{\rho_s}{\delta_b}\right)^2\tilde{P}_\mathrm{e}, \tag{2.10}$$

with the parallel connection length L_c and the gyro radius $\rho_s = \frac{\sqrt{T_\mathrm{e} m_\mathrm{i}}}{eB}$.

The scaling in the collisional regime is given as [83]

$$\left|\frac{v_b}{c_s}\right| = (1+\tau_\mathrm{i})\,C\left(\frac{\delta_\parallel}{L_\mathrm{c}}\right)^2\left(\frac{L_\perp}{R}\right)\left(\frac{\rho_s}{\delta_b}\right)^2\tilde{P}_\mathrm{e}, \tag{2.11}$$

with the mean profile scale length $L_\perp$ and the collisionality parameter $C = \Lambda \cdot \left(\frac{L_\perp}{L_\mathrm{c}}\right)^{-1}$. Λ is given as $\frac{\nu_\mathrm{ei} L_\mathrm{c}}{\omega_\mathrm{ce}\rho_\mathrm{s}}$, with the electron-ion collision frequency ν_ei and the electron cyclotron frequency ω_ce.

Depending on the properties of the plasma, different filament regimes dominate. These cases are discriminated according to the collisionality Λ and the scale size δ_b [83]:

- for small sizes, filaments are in the inertial regime.
- for large filament sizes and small collisionality, filaments are in the sheath dissipation regime.
- for large filament sizes and large collisionality, filaments are in the collisional regime.

In experimental measurements, the Λ dependency of the transition between these regimes was confirmed [85, 86, 87].

As mentioned above, the model was developed to relate the size and velocity of the filaments. For the experimental measurement of both quantities, different

criteria are set to the diagnostic. Due to the high velocities, a high acquisition rate is required. In addition, the small size in the poloidal plane requires a high spatial resolution. Among these diagnostics fulfilling the criteria are gas-puff imaging (GPI) [88], Langmuir probes [89], Lithium beam diagnostic [90], and passive D_α emission [91]. At AUG and Reversed Field eXperiment-mod (RFX-mod), the thermal helium beam diagnostic measures filaments in addition to the previously mentioned diagnostics [40].

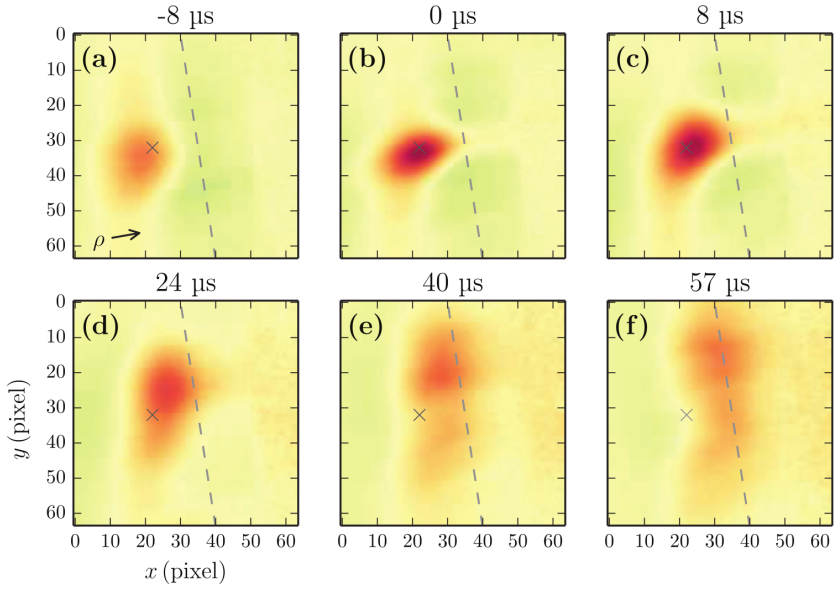

Figure 2.4.: Normalized intensity perturbation of an conditionally averaged blob. Conditional averaging is further explained in Section 6.1.4. This GPI measurement was performed 2014 at AUG, with the triggering channel marked by a cross. It shows the blob propagating into the limiter shadow, indicated by the dashed line. Image from [70].

For two dimensional measurements, a dense grid of measurement points is required. This is often done by GPI, but also Langmuir probes are capable of 2D measurements [92]. By these two-dimensional measurements, filaments can be traced in the SOL. This can be seen in the GPI measurement in figure 2.4. Analogue to GPI, the AUG thermal helium beam diagnostic has a 2D grid of measurement points. In comparison to GPI, they are less dense, but measure in contrast four helium transitions, allowing the reconstruction of electron temperature (T_e) and electron density (n_e). The diagnostic is explained in more detail in section 3.1.

2.5. Phenomena influenced by filaments

The influence of filamentary transport is manifested in the observation of different phenomena. At the midplane, a so-called density shoulder can be observed [93, 94]. It arises by an increased fuelling of the plasma, leading to an increase of the time-averaged SOL density decay length λ_{n_e}. This effect is so strong that the boundary between the near- and far-SOL disappears, as both regions are now dominated by filamentary transport. The increased filamentary transport manifests in increased filament sizes and radial velocities [85, 95]. The fuelling increase, leading to the formation of the density shoulder, also increases the divertor collisionality Λ [96], which is the decisive parameter for the separation of the different filament propagation regimes, described in section 2.4.

The influence of the filaments extends further from the midplane to the target. The small gradients of the time-averaged midplane profiles lead to a broadening of the target heat flux. This broadening manifests for the quasi-continuous exhaust regime (QCE) regime in an increase of λ_q [97]. Besides widening the divertor heat flux profiles, high filamentary transport also increases the heat fluxes on other PFC like the main chamber wall [98].

This heat flux behavior shows that filaments play an essential role in solving the heat exhaust challenge for future fusion devices. Filaments deposit through their radial propagation heat on other PFC besides the divertor target. This reduces the power in the divertor and prevents melting and too high erosion. While type-I ELMs are too massive for future machines and are a threat themselves, smaller filaments increase the heat flux wetted area without damaging the machine. Although a larger area is now exposed to higher heat fluxes, the responsible direct filamentary transport, does not significantly increase the erosion on the PFC over the background values [99].

To make precise predictions regarding these filamentary heat fluxes, their temperatures, densities, sizes, and velocities need to be measured.

2.6. Filament temperature and density measurements

To calculate the convective heat flux of the filaments, analog to equation 2.4, the filament size, temperature, density, and velocity must be known. Multiple diagnostics, including GPI [70], Lithium beam diagnostic (LIB) [99], thermal helium beam diagnostic[40], and Langmuir probes [100], can measure the size and perpendicular velocity, while only a few can measure temperature and density.

First experimental observations of filaments were done at non-tokamak plasmas [101, 102]. These experiments could measure filament temperatures and densities

using Langmuir probes [103, 104]. For a fixed position, the probe measurements allow to determine the temporal evolution of the filament passing by, having the disadvantage that the probe measurement has reduced 2D capabilities and potentially perturbs the plasma [105, 106].

These Langmuir probe measurements use the ion saturation current, having the dependencies $I_{\mathrm{sat}} \propto n_{\mathrm{e}}\sqrt{T_{\mathrm{i}} + T_{\mathrm{e}}}$ [107]. Measurements at the TEXT tokamak showed a relatively small temperature fluctuation in the range of 10 %, while the density fluctuation was up to 50 % [108, 109]. Therefore, the assumption that the ion saturation current perturbation is proportional to the n_{e} perturbation was made for many early Langmuir probe measurements, whereby the dependence on the root of the temperature was neglected [110, 111, 112].

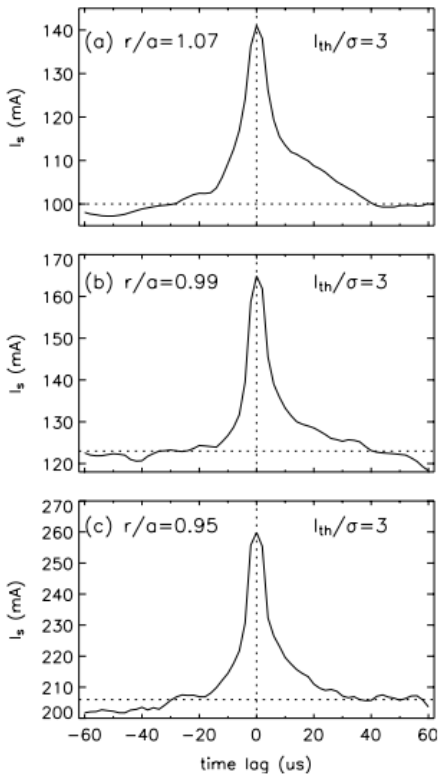

Figure 2.5.: In the three panels, conditionally averaged time traces of the ion saturation current for filaments measured at TEXTOR in 2005 are displayed. The Langmuir probe in a) is positioned in the SOL, while the measurements in b) and c) are located at the edge of the confined region. Image from [107].

The time trace of an ion saturation current measurement from Tokamak Experiment for Technology Oriented Research (TEXTOR) is displayed in Figure 2.5. It shows conditionally averaged measurements on three radial positions. Conditional averaging is an averaging technique where multiple events are placed on top of each other, defined by a filter criterion [113]. As this tool is also used in this thesis, it is explained in more detail in Section 6.1.4.

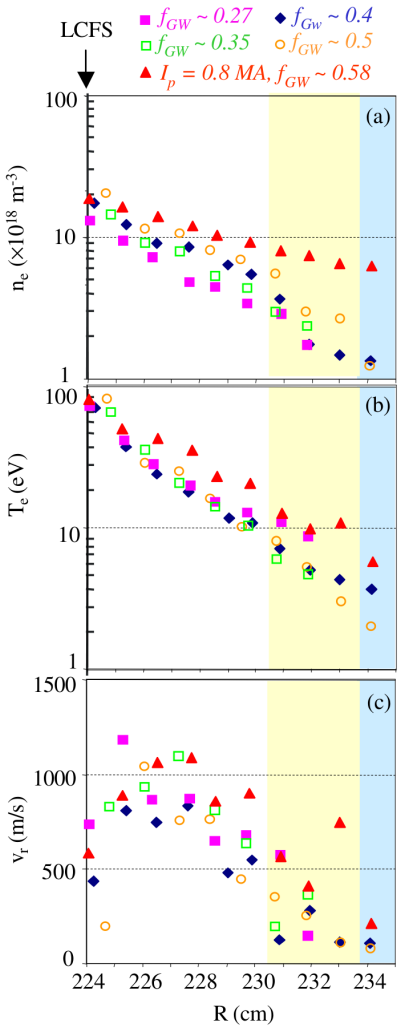

Figure 2.6.: Radial profiles of the blob temperature, density, and radial velocity, measured 2005 with a Langmuir probe in DIII-D. The color coding of the symbols represents different plasma densities during the L-mode, while the yellow and blue background colors represent regions shadowed by different limiters. Image from [100].

Later, Langmuir probe measurements focused again on measuring T_e and n_e simultaneously [114], showing that the relative temperature fluctuation is up to a factor of four smaller than the density one [115]. For the blobs, the density perturbation is in the order of up to 100 % [58]. Tracking filaments over different positions, radial profiles can be generated. This was done at Doublet III-D (DIII-D) using a reciprocating probe, whose results are displayed in Figure 2.6. These radial measurements show a monotonic decrease for the filament temperature and density, while the blobs propagate radially outwards [100]. A scan of the plasma density, normalized to the Greenwald density [116], was performed, showing a correlation with the blob density [100]. Other measurements at DIII-D showed that the relative contribution of filaments to the radial particle transport differs between L-mode and H-mode. In both scenarios, the filaments slow down with increasing radius and lose particles [117].

For measurements performed at the stellarator Wendelstein 7-X (W7-X), temperature fluctuations of filaments were found around to be 10 % of the background amplitude, measured for different heating powers [89]. The typical density fluctuation amplitude is 30 %. As the filaments in W7-X have a weak radial propagation, they barely move during their lifetime [89].

First measurements of the filament T_e and n_e using the thermal helium beam diagnostic, which is used in this thesis and explained in more detail in chapter 3, were performed at RFX-mod [118]. For a fixed radial position, the temporal evolution of filament temperature and density was calculated [119]. It shows a positively peaked structure in n_e, while T_e shows a double structure with a positive and negative perturbation. This double peak is not observed in other measurements and a possible explanation is discussed in section 5.3.

As shown in this section, filament temperatures and densities have been mainly measured by Langmuir probes. For this thesis, the thermal helium beam diagnostic is used. Besides determining the electron temperature and density, the diagnostic has in addition the capability to trace the filaments in 2D. The diagnostic is described in more detail in the next chapter.

3. Diagnostics

This chapter explains the main diagnostic utilized in this thesis, the thermal helium beam diagnostic. It provides radial background profiles for the electron temperature and density and can be used to reconstruct filament properties in the 2D plane. Besides this, the reconstruction relies on integrated data analysis and the magnetic equilibrium reconstruction, which are discussed at the end of the chapter.

3.1. Thermal helium beam diagnostic

3.1.1. Beam emission spectroscopy

Beam emission spectroscopy is an active diagnostic technique used to measure plasma parameters. It relies on the local injection of particles into the plasma, which are excited due to the interaction with the plasma. As a result of the interaction, light is emitted, which can be diagnosed in multiple ways, e.g., in terms of radiances, spectral shifts, and spectral widths [120, 121, 122].

In the first step, neutral particles are injected into the plasma. This is either done by a thermal injection via a valve or by a dedicated diagnostic injector system, which involves the acceleration of ions to high energies and subsequently neutralizing the energetic ions. Besides this, beams from the NBI heating systems are also used [123]. After the neutrals are injected into the plasma, they collide mainly with the plasma electrons. This leads to excitation and eventually to the ionization of the atom. As a result of the ionization, the neutral density drops with distance, limiting the measurable region for the diagnostic.

The excited neutrals further interact with the plasma and are subject to the following secondary effects: On the one side, further collisions can change the excited state or even lead to ionization. In contrast, the spontaneous emission can de-excite the neutral, leading to photon emission. Depending on the neutral species and injection velocity, other populating processes like charge exchange reactions, recombination, and photon absorption are more or less frequent.

There are three models to describe the intensity of the emission for different atomic transitions in the plasma. Although there are no sharp boundaries, the models can be defined based on the plasma collisionality, which can be seen in Figure 3.1 [122]. For very few collisions, the corona model is applied. Here the

assumption is that every excitation via a collision is de-excited purely by the photon emission. For an increased collisionality, a collisional radiative model (CRM) is used. In the CRM, the depopulation of the states occurs via photon emission and other collisions, which excite other states or ionize the atom. By further increasing the collisionality, one reaches the Boltzmann equilibrium. The states are then populated according to a Boltzmann distribution of the energy levels, with a single effective ionization rate describing the neutral atom. In the Boltzmann equilibrium, the de-excitation via the photon emission is negligibly small.

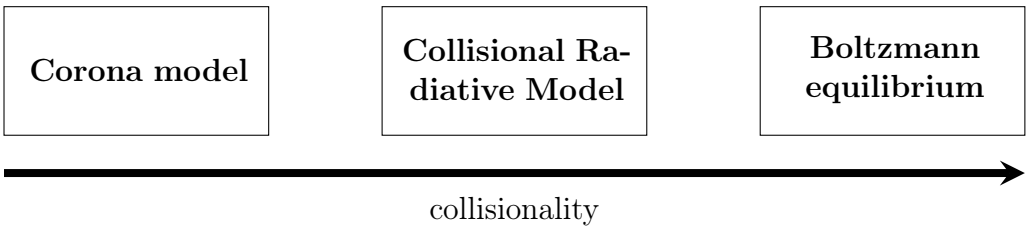

Figure 3.1.: For the plasma-neutral interaction, different regimes for the validity of state population models can be defined. For low collisionalities, the corona model is applied, while high collisionalities can be treated with a Boltzmann equilibrium. The computational more expensive collisional radiative model (CRM) is applied between both regimes.

For AUG, as for other fusion experiments, the collisionality in the plasma requires the usage of a CRM to describe the plasma-neutral interaction for helium.

3.1.2. Setup of the ASDEX Upgrade thermal helium beam

At AUG, the thermal helium beam diagnostic (THB) consists of a fast piezo valve and an optical head in the vessel. These in-vessel components are displayed in Figure 3.2. Outside the vessel, the setup consists of a polychromator connected via 50 m long optical fibers to the vessel and a data acquisition system.

The in-vessel valve is located below the outer midplane in the limiter shadow [124]. A capillary injects helium into the SOL. The cloud has a half opening angle of 20° [124], injecting helium at an estimated velocity of $1760\,\mathrm{m\,s^{-1}}$ [125].

The emission from the helium cloud is measured via an optical head that observes the cloud from the side [126]. This has the benefit: each line of sight (LOS) is almost perfectly tangential to a single magnetic flux surface at its intersection point with the helium cloud. As a result, the plasma along each LOS has only a single temperature and density since the pressure on a flux surface is constant, simplifying the evaluation. The LOS are distributed in a 5×5 grid, with additional radial and poloidal channels along and perpendicular to the injection axis. For each

LOS, the helium emission is then collected via one of two lenses and coupled into optical fibers.

These fibers are guided to a polychromator [126], simultaneously measuring 32 LOS. Inside the polychromator, the emission of every single LOS is divided into four spectral components via dichroic mirrors. Four photomultipliers independently measure these four spectral components. In front of each photomultiplier, an interference filter narrows the spectral radiance into a single wavelength. These are the 587 nm, 667 nm, 706 nm and 728 nm transitions of helium. The photomultiplier signal is sampled with 900 kHz [126].

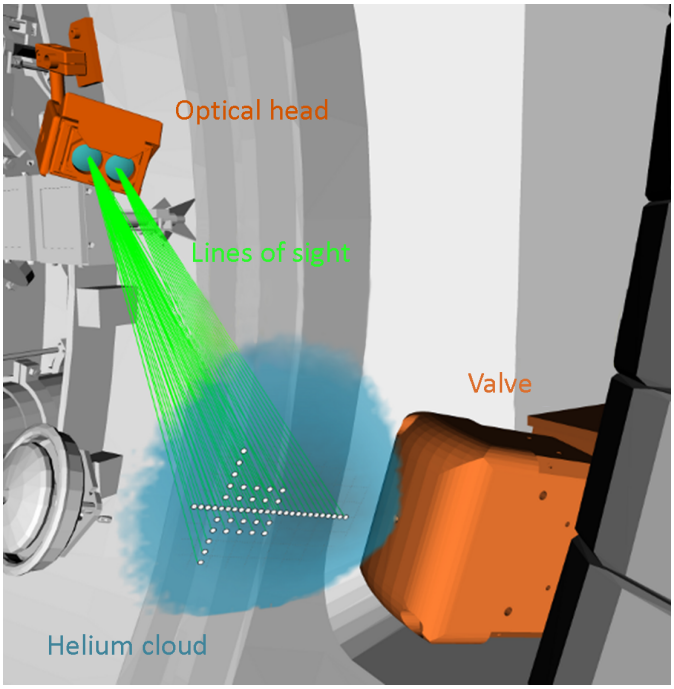

Figure 3.2.: Setup of the in-vessel parts of the ASDEX Upgrade thermal helium beam diagnostic. It consists of a valve (bright orange) that injects helium into the vessel. Via two lenses (blue) in the optical head (dark orange), the radiance of the cloud is collected. Image adapted from [126].

To determine the passive emission, the helium puffing is modulated with a step function with usually 10 Hz, allowing to measure the background in the beam-off phases. The duty cycle usually consists of a 50 ms beam-on phase followed by an equally long beam-off phase. The measured spectral lines, as well as the relevant helium energy levels, are displayed in the Grotrian diagram in figure 3.3.

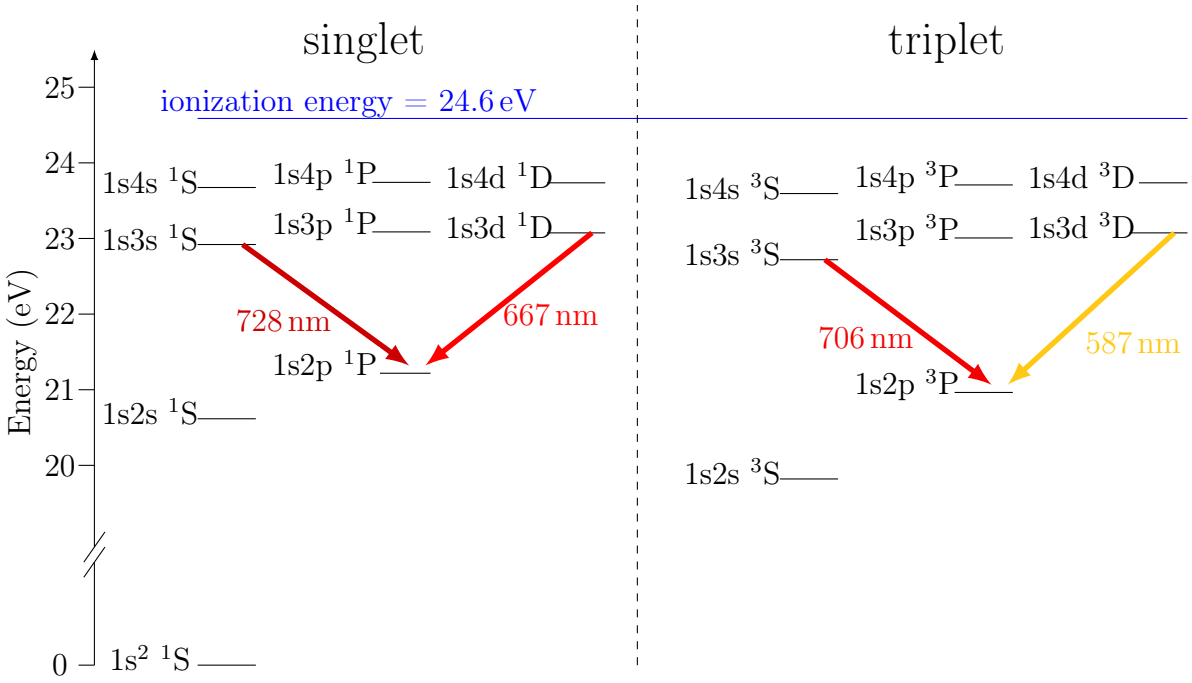

Figure 3.3.: The figure shows selected energy levels of the helium atom. The transitions measured by the polychromator system are indicated by the colored arrows lines. Data from [127].

Only the $1s^2\ ^1S$ ground state is occupied without external excitation. All higher energetic states are excited from the ground state by electron collisions, where the transitions between the two spin systems are particularly slow. Therefore, a metastable population is formed in the triplet state 1s2s ^3S, which dominantly populates the triplet states [128]. The singlet states have a dominant population from the ground state ($1s^2\ ^1S$). Since the metastable state 1s2s ^3S is energetically higher than the ground state, the triplet system has a higher ionization rate because the difference to the ionization energy is smaller. Consequently, the triplet states have a relative population maximum at 25 eV. In contrast, the relative population maximum in the singlet system is 200 eV. [129].

3.1.3. Collisional radiative models used at AUG

Two different CRMs are currently used to calculate the electron temperature (T_e) and the electron density (n_e) at the plasma edge of AUG.

The first model is called the "static model" and is based on the assumption of a collisional radiative equilibrium (CRE), where the equilibrium populations are determined by population and depopulation rates [130]. The CRE, a special

case of the CRM, differs from the Boltzmann equilibrium, where the equilibrium populations are determined according to their energies. In the CRE, given for a fixed T_e and n_e, the relative populations of the excited states are constant, and the ionization only causes an equal population decrease for all excited states. As the CRE depends on the local background T_e and n_e, the relative populations of helium change if it propagates over varying background profiles. Therefore, high transition rates are required to ensure that the assumption of an CRE is fulfilled at every position [131]. Especially for spin-changing transitions, the transition rate coefficients are slow, requiring high background densities to fulfill the assumption of a CRE.

The model is based on theoretically calculated photon emissivity coefficients (PECs) to determine the line emission L_λ. This reads as

$$L_\lambda = n_{\mathrm{He}} \cdot n_e \cdot PEC_\lambda \left(T_e, n_e\right), \tag{3.1}$$

with the neutral helium density n_{He}, the electron density n_e and the photon emissivity coefficient PEC_λ for the considered transition with the wave length λ [132]. Ratios of given PEC for two different spectral lines can be compared to ratios of measured intensities of the two corresponding lines, referred to as line ratios [133]. This way, the neutral helium density cancels due to the evaluation of ratios instead of single intensities.

A dominant density-sensitive line ratio (R_{ne}) can be determined as $\frac{I_{667\,\mathrm{nm}}}{I_{728\,\mathrm{nm}}}$. By dividing the 728 nm line through the 706 nm line, a dominant temperature-sensitive line ratio (R_{Te}) $\frac{I_{728\,\mathrm{nm}}}{I_{706\,\mathrm{nm}}}$ is created. The static model uses these two line ratios, determined from three intensities, to reconstruct the electron temperature and densities. By determining the intersection point of the measured line ratios in the corresponding pre-calculated PEC ratios in the T_e-n_e plane, the experimental temperature and density values are obtained. The result is the electron temperature and density at the considered line of sight position. A line ratio plot is displayed in Figure 17 of Ref. [134].

Since the assumption of a CRE at the plasma edge is not always valid, an unphysical temperature rise in the profiles in the far SOL was observed in certain conditions [125]. This can be seen for the static profile in figure 3.4.

In order to avoid this artificial and unphysical temperature rise in the SOL, a second CRM, called "dynamic model" was recently developed [125]. In contrast to the static model, which calculates the temperatures and densities at each line of sight position, the dynamic model is a forward model. This means input profiles are iteratively updated until the calculated and measured radiances for each LOS converge. As an input, the model takes the T_e and n_e profiles over ρ_{pol}. Considering the ionization, the radiance from all four measured transitions in the helium cloud is calculated from these input profiles. The radiance of the cloud is integrated

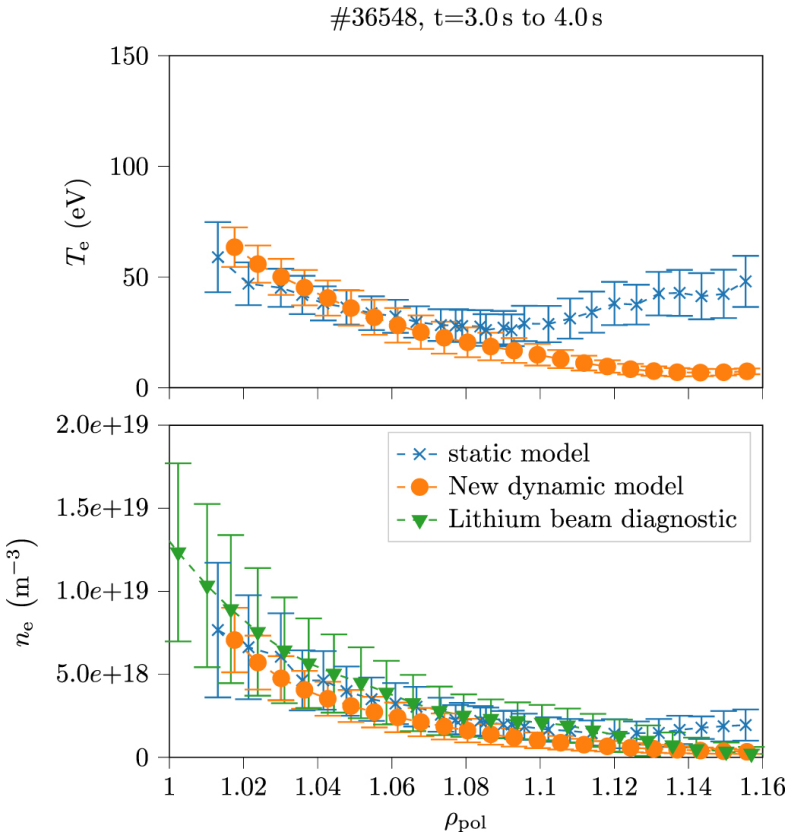

Figure 3.4.: Comparison between THB edge profiles, evaluated with the static and dynamic CRM. At the outer positions, the artificial temperature rise from the static model is corrected by the dynamic CRM. The density is similar for both models, agreeing with the measurement from the Lithium beam diagnostic. Image from [125].

along each LOS. As a cost function for the optimization, the difference between measured and forward-modeled data is calculated for each LOS using one intensity shape (587 nm) and three line ratios ($\frac{I_{728\,nm}}{I_{587\,nm}}$, $\frac{I_{667\,nm}}{I_{728\,nm}}$ and $\frac{I_{728\,nm}}{I_{706\,nm}}$). Iterative updating of the input profiles over ρ_{pol} is repeated till the overall difference is minimized [125]. This profile reconstruction is done within the integrated data analysis framework (see Section 3.2).

The dynamic model differs in multiple points for calculating the cloud emission from the static model. Instead of assuming a CRE, the model calculates the dynamic population of three projection states (1 s^2 ^{1}S, 1s2s ^{3}S, 1s2p ^{3}P). Each projection state combines the population mechanisms of that underlying physical state and, via a projection matrix, other physical states [125]. The transition rates of the projection states use the transition rates of the underlying physical states and

treat the transitions via other states as first-order corrections. The population of the emitting states arises from multiplying the projection states with the projection matrices and the emission by multiplying this with the corresponding Einstein A coefficient. Besides the dynamic state mixing, the forward model treats another effect, the re-absorption. Self-emitted radiation, especially for three ultra violet (UV) transitions, is significantly absorbed and modifies the state population. This re-absorption is included via precalculated absorption files that assume exponential decaying electron temperatures and densities. As the helium injection rates and the magnetic field strength are not identical for all evaluated discharges, multiple datasets are calculated to handle this variation. By selecting the corresponding dataset and profiles, the re-absorption coefficients are determined, and the rates are included in the model.

Comparing the two models, it was found that the dynamic state population significantly impacts the reconstructed T_e in the far SOL. This was the major improvement of the dynamic model over the static model, leading to monotonic decaying temperature profiles in the far SOL. The comparison is displayed in Figure 3.4. Adding the re-absorption to the CRM slightly improved the fit quality but didn't change the temperature and density profiles significantly. For the re-absorption, it could be shown that the effect scales with the helium injection rate. Only when leaving the usual range of injection rates the re-absorption influence becomes so large that it measurably affects the profiles [125].

3.1.4. Extended CRM

The dynamic CRM described in subsection 3.1.3 and in more detail in reference [125] reconstructs one-dimensional radial edge profiles for the electron temperature and density over the normalized poloidal magnetic flux coordinate (ρ_{pol}). To modify this model for filament analysis and to allow the usage of the 5×5 grid of the THB, a 3D Cartesian calculation grid is chosen for the extended CRM. This is needed to resolve the 2D properties of filaments in the poloidal cross-section, where a filament simultaneously passes multiple LOS with identical ρ_{pol} values. Besides this, the 3D grid allows us to take the shape of the filament along the magnetic field into account.

The introduced coordinate system is referred to as beam coordinate system (bco) and originates in the injection point of the valve. In figure 3.5, the relation of the bco to the poloidal cross-section of AUG is displayed. From the helium injection point, the z_{bco} vector points in the direction of the injection, which is approximately antiparallel to the radial direction in torus coordinates. The x_{bco} axis is parallel to the central line of sight of the 5×5 grid. The third Cartesian axis y_{bco} is orientated binormal to the two other axes, which is approximately the poloidal direction.

Input temperatures and densities are given as 2D maps in the z_{bco}-y_{bco} plane, with the projection in the third dimension (x_{bco}) being performed along the magnetic field line. This corresponds to the experimental behavior of the filament.

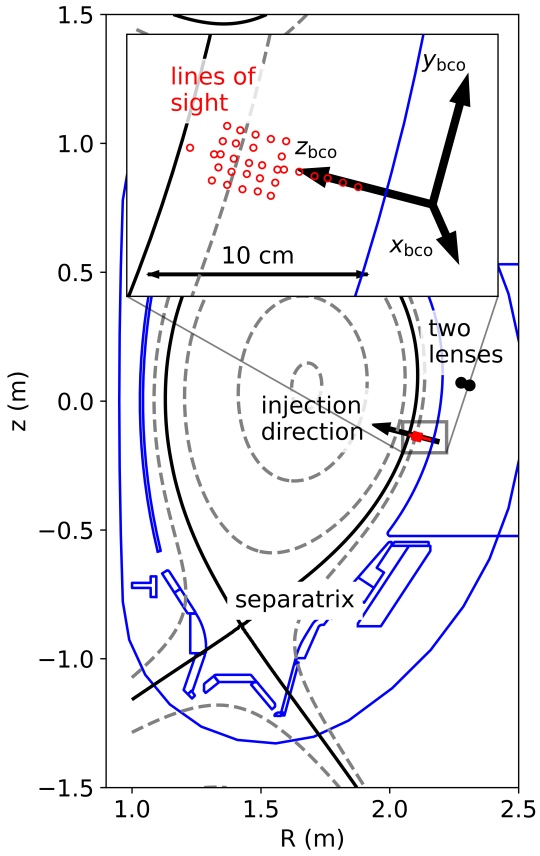

Figure 3.5.: Cross section of ASDEX Upgrade including the helium beam geometry. The lenses of the optical head are located at a toroidal angle of 17° with respect to the valve and the indicated measurement positions. The beam coordinate system is displayed in the enlarged window. z_{bco} points in the direction of the helium injection, x_{bco} goes along the central line of sight and y_{bco} is binormal to the other two vectors. The magnetic equilibrium with its poloidal flux surfaces is shown in gray, the separatrix in black, for #40425, $t = 4.78\,\mathrm{s}$.

Although the spatial extent of the helium cloud is small compared to the torus, the curvature of the magnetic field results in a measurable difference for the three-dimensional temperature and density mapping. The curved shape of a filament, corresponding to one magnetic field line, in the bco can be seen in Figure 3.6.

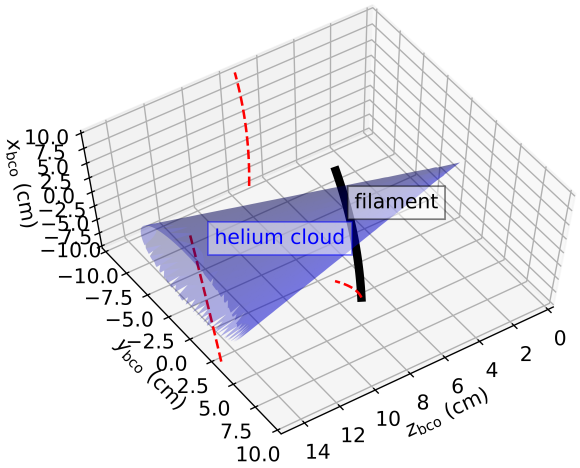

Figure 3.6.: Visualization of a field aligned filament with respect to the helium cloud. The same field aligned mapping is used to generate 3D density and temperature fields from the 2D input values. The red lines are the projections of the filament on the planes.

The grid used for calculating the atomic emission is a cone, which has a half-opening angle of 40°, twice the experimentally determined half-opening angle of the helium cloud [124]. The radiances per atom are calculated along propagation axes starting from the injection point within this cone. The propagation axes consist of 150 points spaced by 1 mm, with 10 axes each covering the opening angle of 40° and the 360 degree angle around the injection axis. For the calculation of each propagation axis, T_e and n_e are mapped on the axis, allowing to calculate the relative populations of the three projection states, resulting from the interplay of state-mixing and ionization. The radiance per LOS is then inferred by using the intersection points between the LOS and the calculation grid. The neutral density needs to be multiplied to get the absolute helium radiation and population from the relative populations calculated on the propagation axes. Since the helium cloud has a Gaussian cross section [124], a Gaussian-Hermite integration [135] is used within the LOS integration to simultaneously integrate the radiation and take the neutral helium density into account. The line-of-sight integration is important because the LOS, which are radially further out from the focal point of the lenses, collect emissions from several points in the z_{bco}-y_{bco} plane. This effect can be seen in Figure 3.7.

For the two-dimensional profiles, no re-absorption files can be precalculated, due to the increased complexity coming along with a larger amount of free variables.

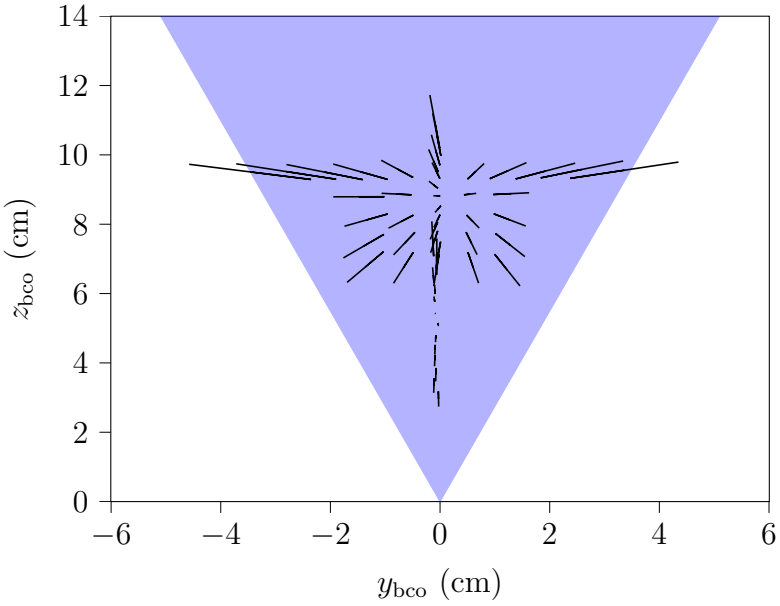

Figure 3.7.: The z_{bco}-y_{bco} plane, as viewed from the optical head. The lines of sight, originating from two lenses, lead to a projection on the plane which fans out from two positions. The blue cone represents the cloud size in the plane.

This discarding of the re-absorption is justified by the low injection rates for the used discharges (below $5 \cdot 10^{19}\,\mathrm{s}^{-1}$ for all measurements), and the evaluation at the 2D grid LOS, which is distant from the injection point [125].

3.2. Integrated data analysis

To infer T_e and n_e profiles from the measurement data of multiple diagnostics, the integrated data analysis (IDA) framework was developed [136]. It uses a Bayesian approach to combine the measurement data of various plasma diagnostics, including electron cyclotron emission (ECE)[137, 138, 139], Lithium beam diagnostic (LIB) [140, 141, 142] and interferometry [143].

The Bayesian inference is based on Bayes' theorem, which is given as [144, 145]

$$P(f|d) = \frac{P(d|f)}{P(d)} P(f). \tag{3.2}$$

The theorem is used to calculate the probability $P(f|d)$ of an assumed profile f for the given measurement data d. $P(d)$ is the evidence of the data and constant for the following optimization. $P(f)$ is the prior probability, which gives the likelihood of the profile f. $P(d|f)$ is the likelihood describing the probability that the measurement data matches the profile, assuming the hypothetical profile f is true. This is done by forward modeling the diagnostic response for the profiles f, comparing them to the measured diagnostic data. For multiple diagnostics, the likelihood is the product of the likelihood from the individual diagnostics. Optimizing the profile f to increase the probability $P(f|d)$ achieves the final profiles.

The profiles for n_e and T_e are given as exponential cubic spline functions. By definition, both quantities are always positive, and an analytical derivative is given for the gradient [145]. All profiles are calculated along the ρ_pol axis, combining results from diagnostics located at different positions.

Using the prior $P(f)$, the likelihood of a profile is quantified, which is used to set profile constraints [146]. The typical constraints are set for the monotonicity and the curvature of the profiles, as well as for smoothness [145]. More advanced priors are based on heat flux profiles [147].
For the profiles evaluated in this thesis, the following settings were applied:

- edge profiles solely determined by the THB,
- weak monotonicity and curvature prior, in order to allow for non-monotonic profiles as they are typical when filaments are present in the SOL

3.3. Magnetic equilibrium and field line tracing

The magnetic equilibria of AUG plasma are reconstructed using the code CLISTE [148, 149]. It iteratively solves the Grad-Shafranov equation using the information about the radial and poloidal components of the magnetic fields, which are measured outside the plasma.

By considering the plasma pressure, a kinetic equilibrium can be created [150, 151]. The otherwise unknown current distribution can be approximated through the pressure constraints, reducing the dependency on equilibrium constraints and improving the equilibrium quality.

The field lines can be traced in the SOL based on the magnetic equilibrium. This allows to determine the connection length L_c (see eq. 2.1), usually measured from the low field side midplane to the outer divertor plates.
The routines used for the field line tracing are based on the GOURDON code [152]. It interpolates the magnetic flux matrix with cubic splines and uses a 5th-order Runge-Kutta method to calculate the field line and its length.

4. Thermal helium beam signal response to synthetic filaments

Optical diagnostics, like GPI or THB, are often used to measure filaments. As these diagnostics do not measure the direct physical properties of the filament but instead the intensity change of the diagnosed emission line, the interaction of the filament with the light-emitting neutrals needs to be precisely understood. For the THB, the dependency of light emission changes of neutral helium on filaments is described in this chapter using synthetic filament data.

Parts of the findings have been published in *D. Wendler, et al.; Two-dimensional reconstruction of filament temperatures and densities with the thermal helium beam at ASDEX Upgrade. Phys. Plasmas 1 September 2023; 30 (9): 092509.* [134]

4.1. Parametrization of filaments and background profiles

In order to model the diagnostic response of the THB on filaments, input data of T_e and n_e as typical for filaments in the SOL is needed. However, this data is not known from experiments, and has to be postulated. The filament is assumed to be a positive perturbation of T_e and n_e added to the background profile. For the temperature, analog for the density, the total temperature T_e is given as $T_\mathrm{e,bg}+T_\mathrm{e,fil}$. The background profile is further described later in this section. The amplitude of the perturbation, also called filament amplitude $T_\mathrm{e,fil}$, is calculated from a Gaussian distribution, given as

$$T_\mathrm{e,fil}\left(\vec{x}\right) = T_\mathrm{e,fil,0} \cdot \exp\left(\frac{|\vec{x}-\vec{\mu}|^2}{2\sigma_\mathrm{fil}^2}\right). \tag{4.1}$$

The identical parametrisation is given for the density amplitude $n_\mathrm{e,fil,0}$. Here, the filament position $\vec{\mu}$ is identical for the temperature and density, as the filament width σ_fil. Both distributions have an amplitude factor $T_\mathrm{e,fil,0}$, which sets the perturbation amplitude at the center of the filament. Due to this axissymmetric filament width, the filament has a circular shape.

The distribution parametrizes the filament in the z_{bco}-y_{bco} plane of the beam coordinate system (bco), used in the extended CRM (see Section 3.1.4). In the third dimension x_{bco}, the filament is mapped according to the magnetic field, assuming constant T_{e} and n_{e} along the magnetic field line.

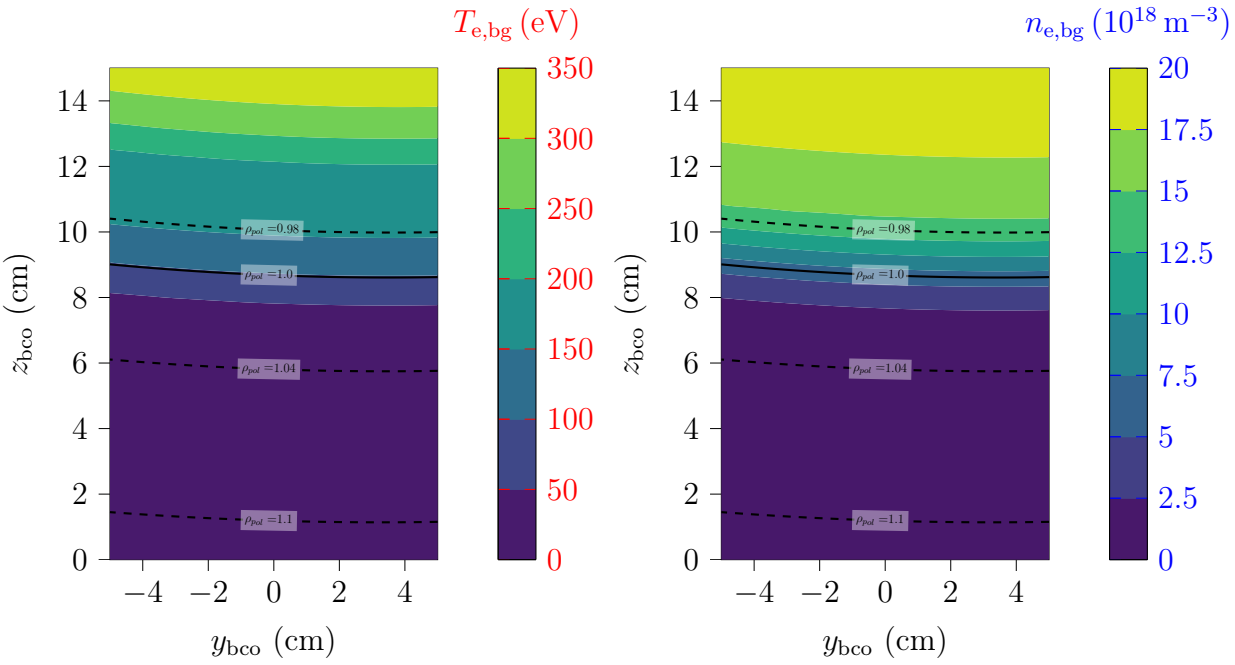

Figure 4.1.: The figure shows the two-dimensional background profiles from discharge #37021, in the interval from 2.2 s to 3.9 s. T_{e} and n_{e} are displayed in the bco. It can be seen that the curvature of the magnetic flux surfaces, given by constant ρ_{pol} values, is weak in the y_{bco} direction.

The two-dimensional background profiles are created from the forward model (see Chapter 3.1.3), calculated for all time points without filaments. This is done by discarding every time point, for which the signal any of the radial LOS is above the 2.5σ threshold, used to distinguish filaments from the background (see Section 6.1.3). For the discharge presented here, the background profiles including the filaments, i.e. including the time points above the 2.5σ differ only marginally from the profiles, for which the filament time points are excluded [134]. These profiles available as a function of ρ_{pol}, are mapped onto the z_{bco}-y_{bco} plane using the corresponding magnetic equilibrium. The synthetic filament analysis, which is presented in this chapter, is performed with the profiles from the L-mode discharge #37021 in the interval from 2.2 s to 3.9 s. Two-dimensional background profiles

resulting from this interval are displayed in Figure 4.1.

It shows that the shape of the magnetic field causes a slight curvature for the projection along y_{bco}. As stated for the filament amplitude, the mapping in the x_{bco} direction is performed along magnetic field lines.

4.2. Relation between filament and intensity perturbation

For simplicity, some basic features of the relation between the filament and the intensity response are discussed for a 1D profile. The profile is obtained from the cut along z_{bco} for $y_{\mathrm{bco}} = 0$. The filament is placed at $z_{\mathrm{bco}} = 8\,\mathrm{cm}$, $y_{\mathrm{bco}} = 0\,\mathrm{cm}$, with a Full Width at Half Maximum (FWHM) of 1.2 cm, an amplitude of $T_{\mathrm{e,fil}} = 40\,\mathrm{eV}$ and $n_{\mathrm{e,fil}} = 6 \cdot 10^{18}\,\mathrm{m}^{-3}$. The background values are $T_{\mathrm{e,bg}} = 55.9\,\mathrm{eV}$ and $n_{\mathrm{e,bg}} = 3.6 \cdot 10^{18}\,\mathrm{m}^{-3}$, resulting in relative filament amplitudes of $\frac{T_{\mathrm{e,fil,0}}}{T_{\mathrm{e,bg}}} = 72\,\%$ and $\frac{n_{\mathrm{e,fil,0}}}{n_{\mathrm{e,bg}}} = 170\,\%$. The comparison between the 667 nm intensity and the electron density with and without filament is shown in Figure 4.2.

The helium is injected at $z_{\mathrm{bco}} = 0$, propagating along the injection axis z_{bco}, corresponding to a radial inwards propagation in the torus geometry. The background intensity, shown as the solid black line, increases for inward propagation. This is caused by the increasing background temperature and density leading to higher excitation. Parallel to the excitation, the ionization of the helium increases, which, together with the opening of the helium cloud, causes a decrease in the neutral helium density. The interplay between excitation and ionization determines the position of the maxima, from which the drop in neutral helium density dominates over the excitation and causes a monotonically decaying intensity profile.

For the case with a filament, a positive intensity perturbation arises ahead of the filament position due to the increased excitation. Together with the modified ionization by the filament, the position of the maximum intensity shifts, leading radially inwards of the filament to a drop of intensity below the background profile. This can be clearly seen in Figure 4.2b, where the relative perturbations $\frac{I_{667\,\mathrm{nm,fil+bg}} - I_{667\,\mathrm{nm,bg}}}{I_{667\,\mathrm{nm,bg}}}$ and $\frac{\left(n_{\mathrm{e,fil}} + n_{\mathrm{e,bg}}\right) - n_{\mathrm{e,bg}}}{n_{\mathrm{e,bg}}} = \frac{n_{\mathrm{e,fil}}}{n_{\mathrm{e,bg}}}$ are compared. Inside $z_{\mathrm{bco}} = 8.5\,\mathrm{cm}$, the intensity perturbation gets negative, caused by the increased ionization of the neutral helium at the filament position due to the increased T_{e} and n_{e}.

The relation between the perturbations is further analyzed by fitting a Gaussian (parametrized equal to eq. 4.1) on the relative intensity and density perturbation. The results are given in Table 4.1.

The table clearly shows that the relative perturbations between both quantities are not equal. For the given case, the position of the intensity perturbation is

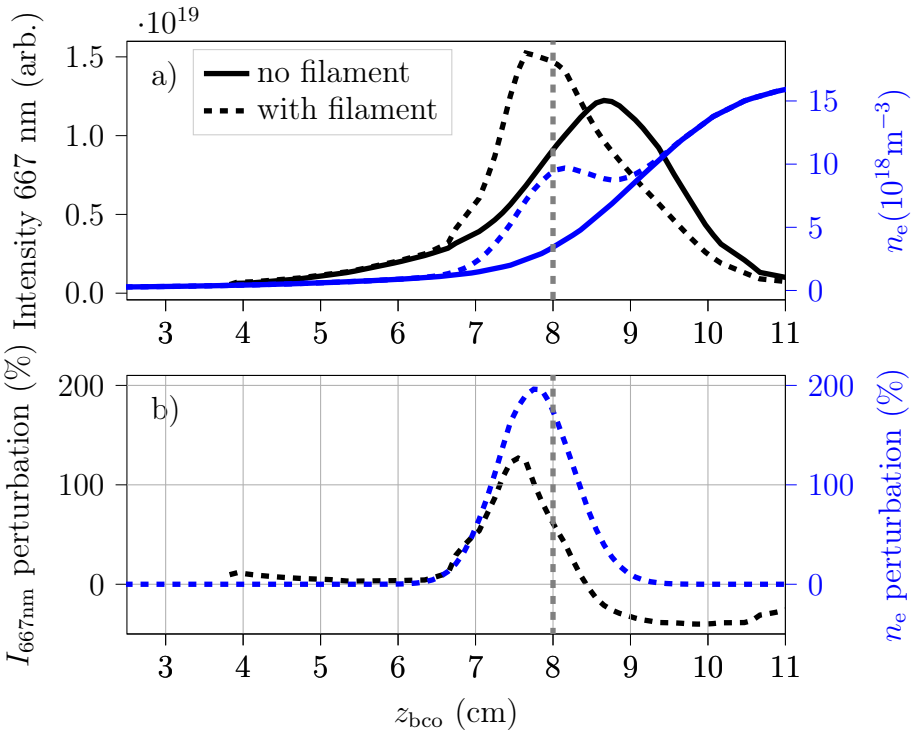

Figure 4.2.: One-dimensional cut for an artificial filament. In blue, the density background is displayed with a solid line, and the profile with filament (its position is indicated by a vertical dashed line) is displayed by a dashed line. In subplot a), the absolute density and 667 nm emission are displayed, while subplot b) shows for both quantities the relative perturbation caused by the filament.

radially further outside (smaller z_{bco}), having a smaller relative amplitude. Besides this, the size of the filament in the intensity picture is smaller.

General trends for the filament response can be formulated, based on the characteristics seen in Figure 4.2. The position of the intensity perturbation from the THB is radially further outside compared to the position of the density and temperature perturbation of the filament. This distance between the relative perturbation maxima increases for filaments close to the separatrix, while the maxima positions in the far-SOL are nearly identical. For a maximum displacement between the intensity perturbation and the filament of 1 cm, which decreases to zero during a 200 µs long radial outwards propagation, the velocity calculated by the intensity perturbation would be 50 m s^{-1} lower compared to the true filament velocity. So, only in these extreme cases, the radial velocity measurement is seriously influenced by the displacement between the intensity perturbation and the filament position.

Table 4.1.: Comparison between the relative intensity and density perturbation of a synthetic filament, by fitting a Gaussian to the relative perturbations from Figure 4.2b. The density-sensitive line ratio comparison in the right column is analyzed and described in Section 4.4

	n_e perturbation	$I_{667\,\mathrm{nm}}$ perturbation	$\frac{I_{667\,\mathrm{nm}}}{I_{728\,\mathrm{nm}}}$ perturbation
amplitude (%)	197	122	48
position μ_z (cm)	7.8	7.5	7.7
FWHM (cm)	1.2	0.9	1.2

This displacement between the filament and the intensity perturbation is a common feature also observed in other studies like D_α simulations [153] and other edge experiments [154]. In contrast to these measurements, the LIB, which has a higher injection velocity than GPI or THB, observes the maxima of the intensity perturbation radially inside the filament position [142]. The shift in the maximum perturbation position results from the high injection velocity of the lithium, while the atom moves a significant distance before the excited lithium state emits the photon and, therefore, influences the intensity profile.

An important feature is that the circular filament creates an elliptical intensity perturbation in all observed cases. The ellipticity varies with the position on the background, as well as the filament parameters. A half-moon shape of the intensity perturbation can be observed in extreme cases [134].

The following sections display selected dependencies for the intensity and line ratio amplitude, the intensity and line ratio perturbation size, and the sensitivity to background values. The background comes as in section 4.1 from L-mode discharge #37021, t =2.2 s to 3.9 s. Unless the filament parameter (parametrization from eq. 4.1) is explicitly stated, the filament is described with the values of Table 4.2.

Table 4.2.: Parameters of the synthetic filament if not explicitly stated.

$T_{e,\mathrm{fil},0} =$	$40\,\mathrm{eV}$
$n_{e,\mathrm{fil},0} =$	$6 \cdot 10^{18}\,\mathrm{m}^{-3}$
$\vec{\mu} = (z_{\mathrm{bco,fil}}, y_{\mathrm{bco,fil}}) =$	$(8\,\mathrm{cm}, 0\,\mathrm{cm})$
$\sigma_{\mathrm{fil}}/\mathrm{FWHM}_{\mathrm{fil}} =$	$0.5\,\mathrm{cm}/1.2\,\mathrm{cm}$

4.3. Temperature and density dependency of the intensity perturbation

The dependency of the intensity amplitude on different filament temperatures and densities is presented in this section, using the same background profiles and filament position and size as in section 4.2. As the position of the maximum intensity perturbation is not equal to the position of the density perturbation, the maximum density perturbation is compared to the maximum density perturbation. In Figure 4.3, the dependency of the intensity perturbation on $T_{\mathrm{e,fil}}$ is displayed for all four helium lines measured by the polychromator system (see figure 3.3 for the Grotrian diagram of helium).

The spin of the emitting state characterizes the behavior of each line. The 587 nm line (Figure 4.3a) and the 706 nm line (Figure 4.3c) from the triplet system show a negative correlation with the temperature. This is caused by a background temperature of 55.9 eV, which is higher than the temperature of the relative population maxima of the triplet states of 25 eV. As a result, the intensity drops for the entire range of added filament temperatures. By comparing the temperature response for different filament densities, it can be seen that the intensity change by different filament densities is higher than the intensity change within each temperature scan. Accordingly, the filament density sets an offset for the respective temperature curve.

The singlet lines of 667 nm and 728 nm are shown in the Figure 4.3b and 4.3d. Here, the temperature amplitude is positively correlated with the intensity change. This is due to the relative population maximum of the singlet states around 200 eV, which is not exceeded in the scanned range. As with the triplet states, the underlying density vertically separates the temperature curves. The slope of the line indicates the sensitivity of the transition. A flat slope corresponds to a small change in intensity for a change in temperature, indicating a weak sensitivity.

Although the characteristics of the lines within each spin system are the same, the lines differ in their relative amplitudes. This allows the creation of a temperature dependency by forming line ratios, which is discussed in Section 4.4. The line ratios are more sensitive because the singlet intensity perturbation increases with temperature while the triplet intensity perturbation decreases at higher temperatures.

As observed in the temperature scan, the filament density is the dominant parameter influencing the intensity perturbation. The corresponding scan is displayed in Figure 4.4. It shows that the intensity perturbation is dominantly correlated with $n_{\mathrm{e,fil}}$. The curves have a steep rise for low filament densities, followed by a flat linear rise for high density amplitudes. As with the temperature scan, the lines have different relative amplitudes despite the identical trend. The relative

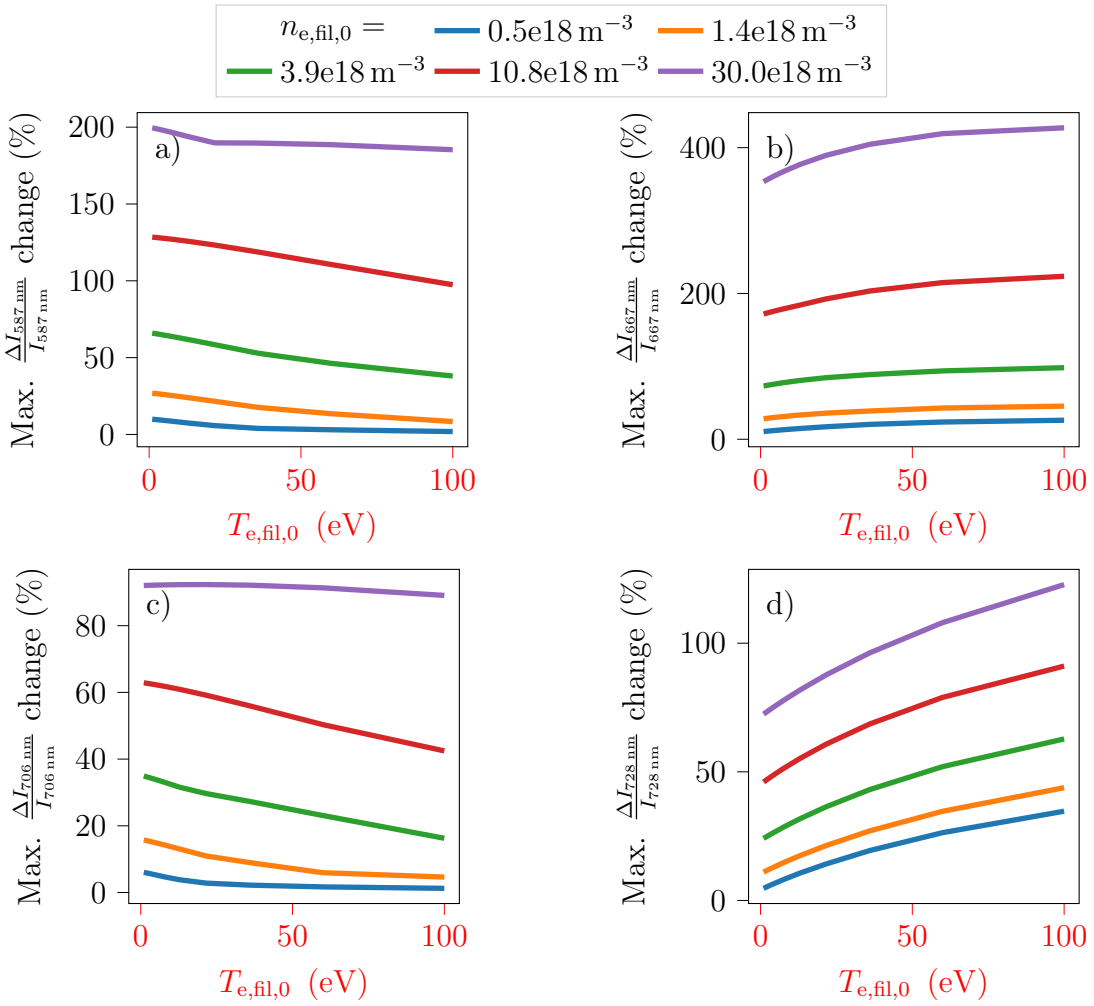

Figure 4.3.: The relative intensity perturbation of four helium transitions scanned for the filament temperature amplitude, using multiple fixed filament densities. As the position of the maximum intensity perturbation is not identical to the filament position, the maximum intensity perturbation is considered. The background values are $T_{e,bg} = 55.9\,\text{eV}$ and $n_{e,bg} = 3.6 \cdot 10^{18}\,\text{m}^{-3}$.

change is highest for the 667 nm line, reaching over 400 % for the cases with the highest filament density ($\frac{n_{e,fil}}{n_{e,bg}} = 830\,\%$). This is a factor of four higher than the intensity perturbation of the 728 nm line.

From the two spin systems, only the singlet lines are positively correlated with T_e and n_e. This is later important to identify the filaments in the experiment. In the experiment, the 2.5σ criterion, described in section 6.1.3, is applied to the

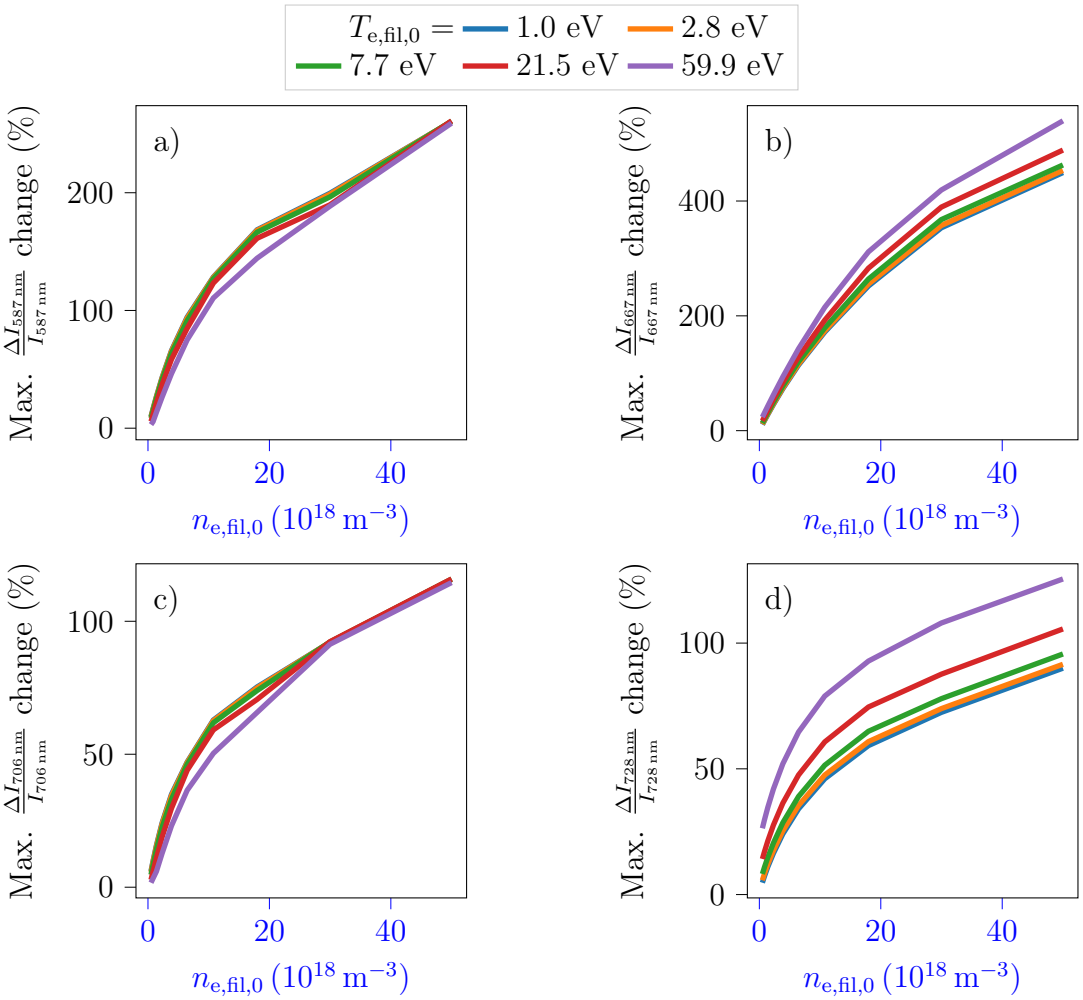

Figure 4.4.: The relative intensity perturbation of four helium transitions scanned for the filament density amplitude. Within each scan, different filament temperatures are compared. For the intensity perturbation, the relative maximum is used. The background values are $T_{e,bg} = 55.9\,\text{eV}$ and $n_{e,bg} = 3.6 \cdot 10^{18}\,\text{m}^{-3}$.

raw intensity. The 667 nm line is chosen to identify the filaments with a positive temperature and density perturbation. In comparison to the other singlet line, the 728 nm transition, the relative intensity changes induced by a filament are higher. In addition, the experimental setup has a higher signal-to-noise ratio (SNR ratio) for the 667 nm line.

4.4. Perturbation of line ratios by filaments

As shown in the previous sections, the absolute intensity of a helium line is not a good proxy for the density or temperature perturbation. Motivated by the "static CRM" (see section 3.1.3), one could use line ratios to investigate their relation to the filament parameters. For the density-sensitive line ratio (R_{ne}), given as $\frac{I_{667\,\mathrm{nm}}}{I_{728\,\mathrm{nm}}}$, the 1D cut analogue to Figure 4.2, is displayed in Figure 4.5. The performed Gaussian fit results in a perturbation position $z_{\mathrm{bco}} = 7.7\,\mathrm{cm}$ (7.8 cm for the n_{e} perturbation), and the FWHM = 1.2 cm, which is equal to the density perturbation. This shows, that the R_{ne} is capable of determining size and position of the density perturbation. Nevertheless, the relative perturbation amplitude is different, see Table 4.1.

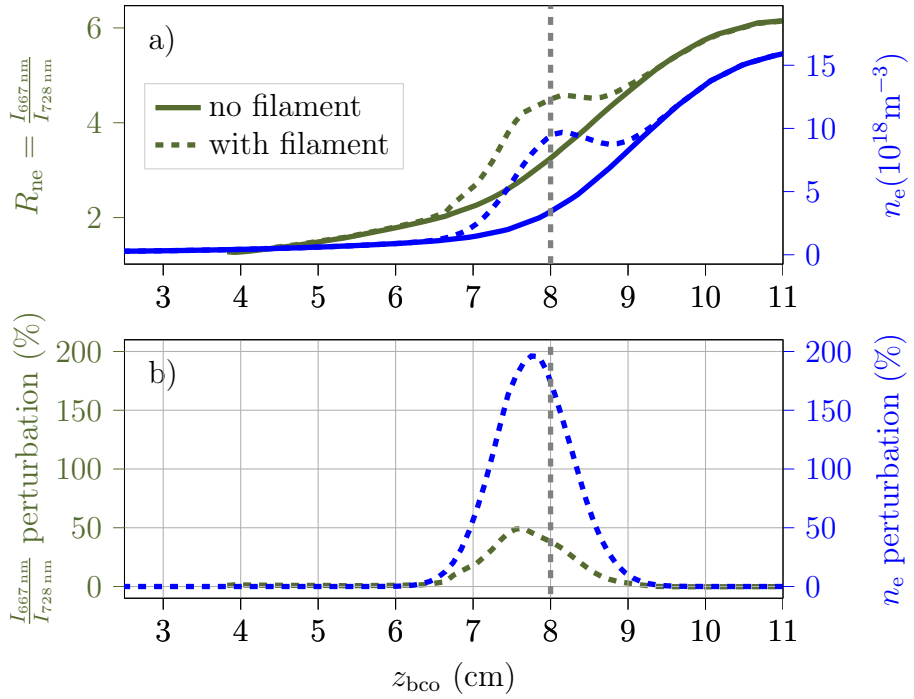

Figure 4.5.: a) shows the absolute change of the density-sensitive line ratio (R_{ne}) by adding a filament to a background profile. This is compared against the density with (dashed) and without (solid) filament. The relative changes of the line ratio and density are compared in b).

To further check this dependence, the filament amplitude is scanned. The density is compared to R_{ne}, while the temperature is compared to the temperature-sensitive line ratio (R_{Te}). R_{Te} is formed as $\frac{I_{728\,\mathrm{nm}}}{I_{706\,\mathrm{nm}}}$. Both plots can be seen in Figure 4.6. As for the intensity comparison, the maximum of the line ratio perturbation

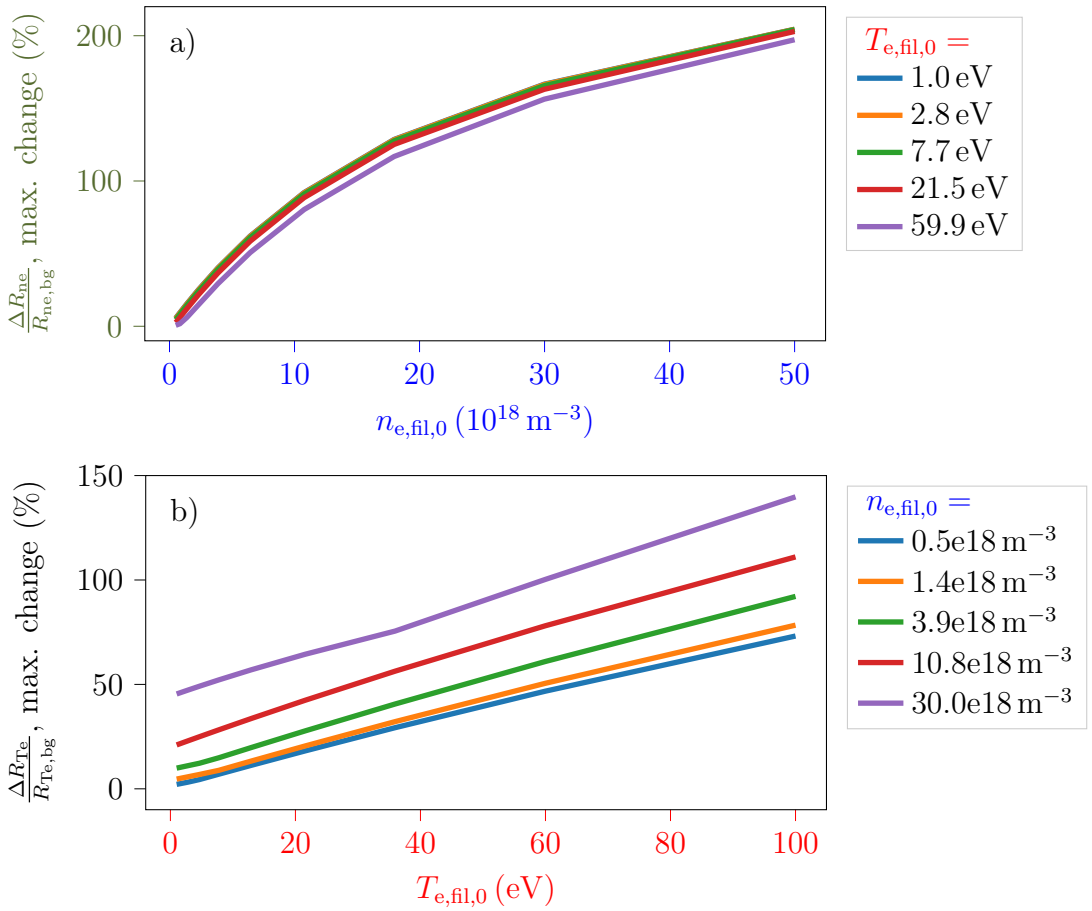

Figure 4.6.: Normalised line ratio difference versus filament amplitude for (a) density (R_{ne}) and (b) temperature (R_{Te}). In comparison to the intensities in figure 4.3, the R_{T_e} line ratio has a dominant temperature dependency. The background values are $T_{e,bg} = 55.9\,eV$ and $n_{e,bg} = 3.6 \cdot 10^{18}\,m^{-3}$.

is chosen, to be independent of the perturbation position. The relative line ratio perturbations are given as $\frac{R_{bg+fil}-R_{bg}}{R_{bg}} = \frac{\Delta R}{R_{bg}}$.

In Figure 4.6a, it can be seen that the perturbation of the density-sensitive line ratio has a limited growth with the $n_{e,fil}$, as seen for the intensity. The change of the density-sensitive line ratio is almost entirely independent of the filament temperature, similar to the line intensities. A significant difference can be seen for the temperature dependency, displayed in Figure 4.6b. The temperature-sensitive line ratio grows linearly with the temperature amplitude $T_{e,fil}$. The curves have a vertical offset for different $n_{e,fil}$.

This shows, that the evaluation of line ratios is superior to the evaluation of single line intensities, since line ratios exhibit a much clearer dependence on temperature and density. As displayed in table 4.1, the R_{ne} is capable of reproducing the 1D size and position of the filament, while the relative amplitudes of the density and the line ratio are different. In section 5.3, the temperature and density reconstruction with the static model, using these line ratios, is further described.

4.5. Size relation between the intensity perturbations and filaments

The relation between the filament size and the intensity size is further investigated in this section. This is done considering the two-dimensional size determined from the 2D intensity perturbation, which is linearly interpolated from the LOS. For a given circular filament with a size of $\sigma_{\mathrm{fil}} = 0.5\,\mathrm{cm}$, the resulting intensity perturbation of the 667 nm line is displayed in Figure 4.7.

Analogue to the 1D case, the position of the maximum intensity perturbation is shifted to lower z_{bco} values. Besides this, the circular filament causes an elliptical intensity perturbation. In Figures 4.7b and 4.7c, the 1D cross sections of the intensity perturbation through the center of the filament are displayed. By fitting a Gaussian, the width of the filament in the cross-section is displayed. Δz_{bco} is the FWHM determined for a cross section along z_{bco} which goes through the filament position. The analogue procedure is performed to get Δy_{bco}. For a constant filament position and amplitudes, the width scan of σ_{fil} is displayed in Figure 4.8.

The comparison shows no linear correlation between the filament and intensity perturbation size. For filament widths below 2 mm, the LOS setup prevents a meaningful evaluation (LOS spacing is 6 mm). For larger filament sizes, the ratio between Δz_{bco} and Δy_{bco} increases, showing an increasing ellipticity [1]. The increasing ellipticity in the intensity frame is caused by a strong increase of the poloidal width Δy_{bco}. Along the y_{bco} axis, the n_{e} perturbation of the filament has a Gaussian shape. As the relation between the density perturbation and the intensity perturbation is strongly non-linear (see Figure 4.4b), the low density amplitudes, that are radially outwards, translate into higher relative intensity amplitudes. As a result, the intensity perturbation slopes outward less than the density perturbation, resulting in a larger y_{bco} size.

For filaments with a given size of 1.4 cm, the FWHM of the resulting intensity perturbation along the y_{bco} axis is 2.4 cm, which corresponds to the size of the 5×5 grid, setting a hard limit for the maximum practical intensity size of the

[1] The ellipticity is defined as $\kappa_\epsilon = \frac{b}{a}(\text{with } b > a) = \frac{\Delta y_{\mathrm{bco}}}{\Delta z_{\mathrm{bco}}}$

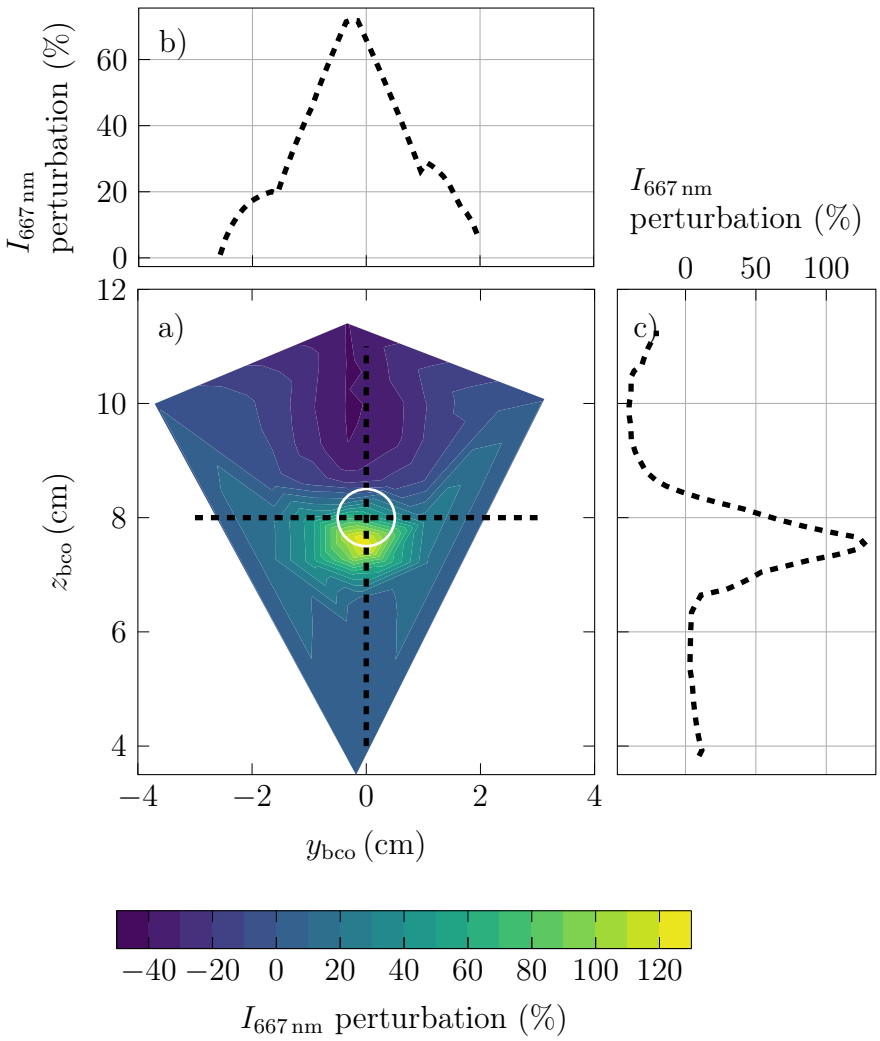

Figure 4.7.: a) Two-dimensional intensity perturbation caused by a filament. The filament is indicated as the white circle with a radius of σ_{fil}. b) and c) show the cross-sections through the filament position along y_{bco} and z_{bco}, indicated by the dashed lines. The steps in b) originate from the finites spacing of the LOS and the linar interpolation.

filament. Remarkably, the apparent radial width of the filament, estimated as z_{bco}, is smaller than the width of the density for the given inputs. By only measuring this value, the filaments appear smaller than they actually are. The reason is the increased ionization, which causes a drop in the neutral helium, and therefore also in the intensity. As a result, the filament has a smaller appearance in the intensity perturbation. This effect is the second reason causing an increased ellipticity of the

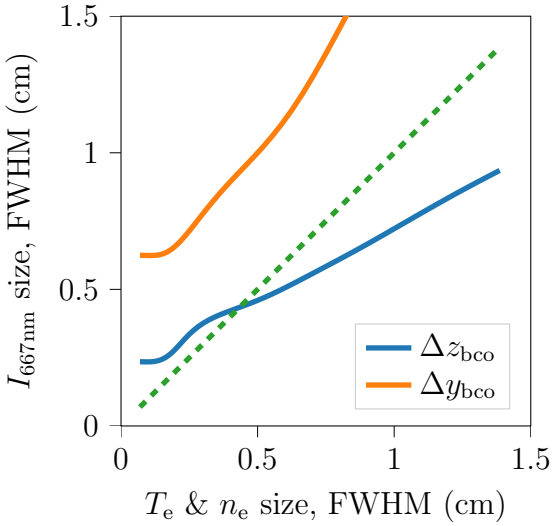

Figure 4.8.: Comparison of the intensity perturbation size versus the input filament size (FWHM). The relation is non-linear at small scales due to the limited number of LOS and at large scales due to increasing ellipticity caused by the stronger increase of Δy_bco. The background values are $T_\mathrm{e,bg} = 55.9\,\mathrm{eV}$ and $n_\mathrm{e,bg} = 3.6 \cdot 10^{18}\,\mathrm{m}^{-3}$.

intensity perturbation with an increased filament size. Even for the smallest sizes, the circular density and temperature perturbation causes an elliptical intensity perturbation.

The width scan is repeated for the density-sensitive line ratio (R_ne), shown in Figure 4.9. It shows, that Δz_bco, which corresponds to the radial width, agrees quite well with the input filament size. This is similar to the 1D case, shown in figure 4.5b. For the poloidal width Δy_bco, the size is overestimated for the whole range of filament widths, which is similar to the intensity picture. Here, too, the disturbance of the line ratio amplitude is particularly strong for small densities (see Figure 4.6a). As a result, the circular filament has an elliptical shape in the line ratio perturbation, similar to the intensity perturbation. In addition, the fanning out of the LOS, as seen in Figure 3.7, artificially increases the apparent size in Δy_bco direction.

To conclude, neither the intensity nor the density-sensitive line ratio can properly reconstruct the filament size in both dimensions, with the line ratio agreeing for the radial expansion. To relate the filament shape properly with the measured line ratios, a dynamic CRM is required. This case contradicts the general interpretation, sometimes made for GPI, that the sizes and fluctuation amplitudes between intensity and density are similar [88].

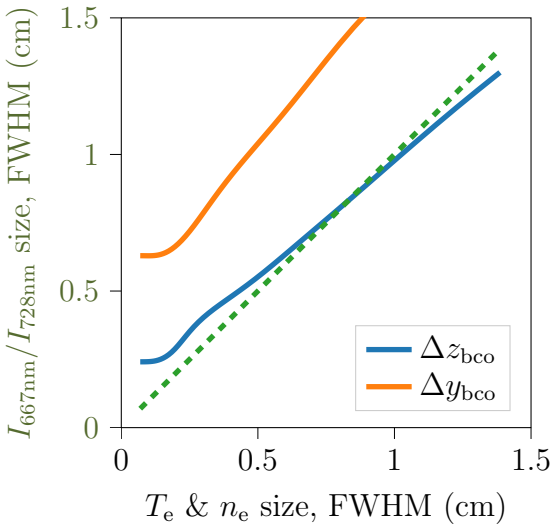

Figure 4.9.: The density-sensitive line ratio (R_ne) size is compared against the input filament size (FWHM). The relation is non-linear, at small scales due to the spacing of LOS, at large scales due to increasing ellipticity caused by the stronger increase of Δy_bco. The background values are $T_\mathrm{e,bg} = 55.9\,\mathrm{eV}$ and $n_\mathrm{e,bg} = 3.6 \cdot 10^{18}\,\mathrm{m}^{-3}$.

4.6. Sensitivity of the intensity response at different background values

The intensity response of the filament, as demonstrated in the previous sections, depends on the temperature and density amplitude of the filament. In this section, the influence of the background profiles is studied. This is done to determine the intensity response of a filament with a fixed amplitude, for a varying plasma background.

In the experimental context, this comparison allows to determine the intensity perturbation for a given background profile. By knowing this, the magnetic equilibrium can be shifted, which leads to a shift of the background profiles, to get a good SNR ratio at the position of the 5×5 grid. The profiles in this scan are shifted along the z_bco axis to analyze the dependency on the background profiles. This corresponds in the experiment to shifting the magnetic equilibrium with respect to the fixed LOS positions. In contrast to shifting the filament position, this method prevents the influence of other factors, as the distance between the valve and the filament is always constant, and the filament is always located at the identical position with respect to the LOS. The separatrix density is in all cases $n_\mathrm{e} = 6.5 \cdot 10^{18}\,\mathrm{m}^{-3}$, and shifts with the equilibrium.

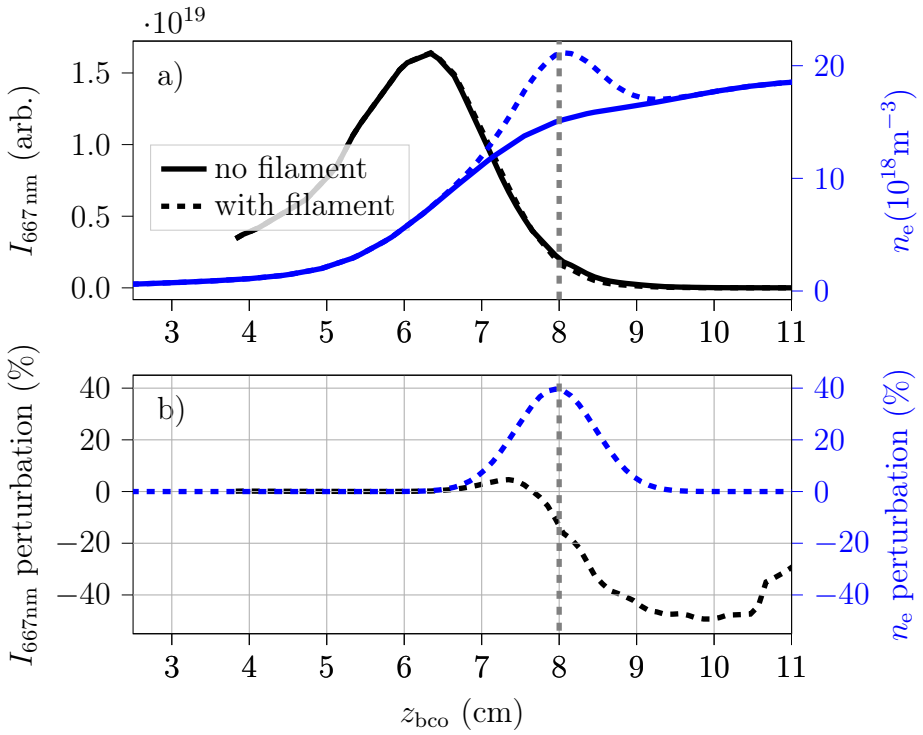

Figure 4.10.: Comparison of 1D profiles for a filament placed in the confined region. This was created by shifting the background profiles −2.5 cm w.r.t. the profiles shown in Fig 4.2. a) Comparison of the intensity and density profiles, with and without the filament. The relative perturbation of both quantities caused by the filament is displayed in b).

In figure 4.10, the original density profile from Figure 4.2 is shifted by −2.5 cm. This corresponds to placing the filament in the confined region. For the given and fixed filament amplitude of $T_{\mathrm{e,fil}} = 40\,\mathrm{eV}$ and $n_{\mathrm{e,fil}} = 6 \cdot 10^{18}\,\mathrm{m}^{-3}$, the relative filament amplitude decreases due to the higher background profiles, being only 40 % (see Figure 4.10b) for the density in comparison to 200 % as shown in Figure 4.2b for the original profile. The relative temperature amplitude is 25 %, which is lower than the temperature perturbation of the original profile (67 %). The resulting intensity perturbation is small, in maximum only 4.6 %. In addition, the position of the maximum intensity perturbation is located at $z_{\mathrm{bco}} = 7.2\,\mathrm{cm}$, which is 0.8 cm further radially outwards compared to the density perturbation. Beyond this narrow positive intensity perturbation, the relative intensity perturbation drops below zero for the remaining distance along the filament due to the increased ionization.

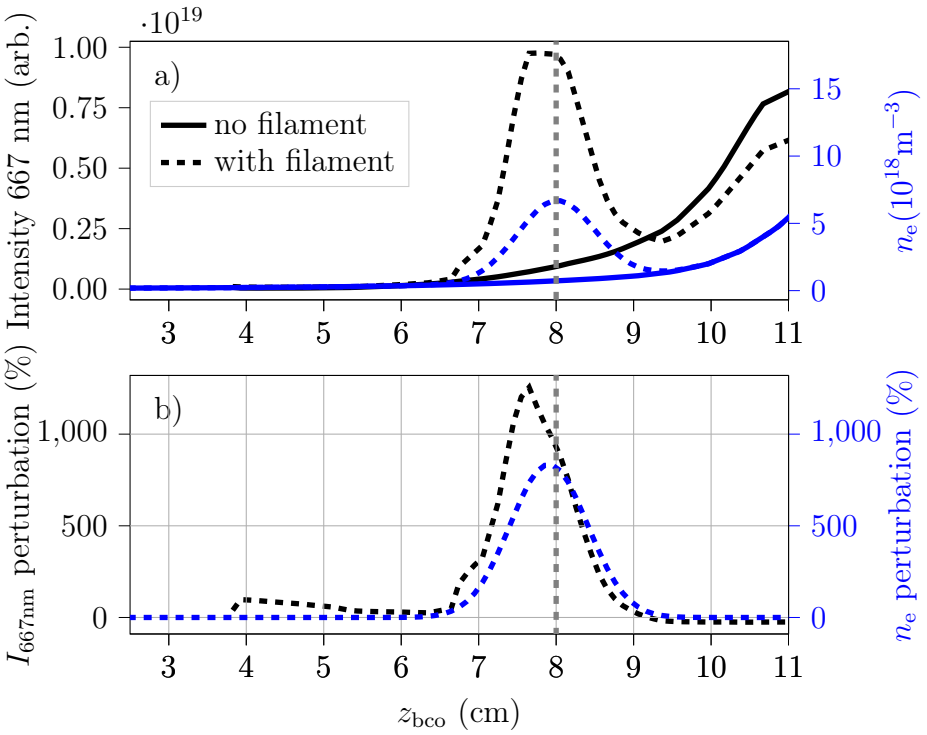

Figure 4.11.: Comparison of 1D profiles for a filament placed in the far-SOL. This was created by shifting the background profiles by +2.5 cm. a) Comparison of the intensity and density profiles, with and without the filament. The relative perturbation of both quantities caused by the filament is displayed in b).

A background profile shifted by +2.5 cm into z_{bco} direction is shown in Figure 4.11. Here the shift corresponds to placing the filament further outside into the SOL. It can be seen that this causes significant differences compared to the confined region case shown in Figure 4.10. Here, the position and size of the intensity perturbation are very similar to the density perturbation. All relative perturbation amplitudes are high, 830 % for the density, 270 % for the temperature, and 1250 % for the intensity perturbation. In this case the intensity response to a density perturbation is much larger than in the other considered cases indicating that the relative intensity of the THB signal in the far-SOL represents the density perturbation quite well. As shown in Figure 4.11a, the intensity profile exhibits two peaks: one caused by the filament and a second one caused by the rise of the background density profile. Besides this, the negative relative intensity due to ionization in this example is comparable weak and amounts to maximum −25 %.

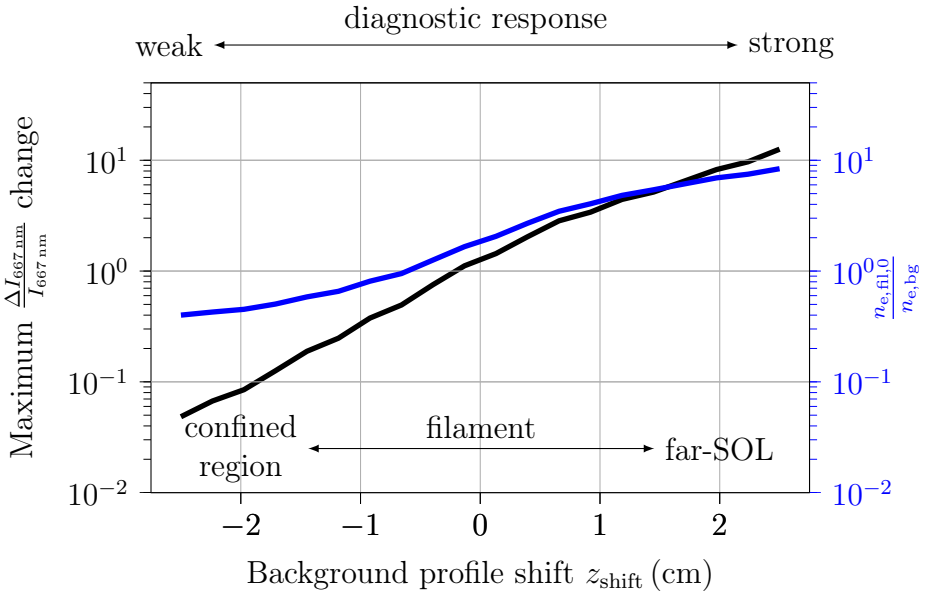

Figure 4.12.: Maximum relative intensity perturbation of the 667 nm line for a background shift along the z_{bco} axis. On the right axis, the ratio between the constant filament density amplitude and the varying background density is displayed. Positive z_{shift} values correspond to the displacement of the filament in the direction of the far-SOL, while negative values describe a displacement in the direction of the confined region. This shows the strong diagnostic response on filaments in the far-SOL

By consecutively shifting the background profile from −2.5 cm to +2.5 cm into z_{bco} direction, the relation between the relative intensity perturbation for a fixed density amplitude and varying background densities can be obtained as a function of the background profile shift z_{shift}. This is illustrated in Figure 4.12. In the logarithmic representation, it can be seen that the intensity perturbation changes by almost three orders of magnitude within the range of the investigated background shifts, while the density amplitude only changes by one order of magnitude. The almost linear curve of the relative intensity change in the logarithmic representation indicates, that a filament with fixed temperature and density gives rise to an exponential increase of the relative intensity perturbation with increasing distance to the confined region. In the density amplitude, the curve represents the inverse shape of the background profiles. In the far-SOL, as well as the confined region, the density gradient of the background profile is relatively flat, resulting in a flat profile for the relative density amplitude.

The tiny intensity and line ratio perturbation close to the separatrix limits the possibility of reliably identifying filaments in this region. This is further aggravated as the region around the separatrix is the presumed filament birth location, where the filaments have a total temperature and density marginally higher than the background. The combination of the low intensity response around the LCFS and the filament T_e and n_e amplitudes, which would in reality be lower at the separatrix than in the performed scan, makes an identification of filaments in the separatrix region or the confined region practically impossible.

In order to overcome this problem and to be able to measure the filaments, the discharges for this thesis have been designed in a way that the 5×5 grid of the THB measures in the far-SOL. This restriction of the measurement region, preferring filament measurements in the far-SOL, applies similarly to GPI [88, 70].

4.7. Experimental detection threshold of filaments

Using synthetic filaments, the relative intensity perturbation induced by a given filament is determined. This is possible because the cases with and without filament can be clearly distinguished. Unfortunately, this is not the case in the experiment, since the filament cannot be easily discriminated from the background profile due to noise and small-scale fluctuations. In experimental data, filaments are identified by the 2.5σ criterion, explained in more detail in Section 6.1.3. According to this criterion, a filament is identified in a raw signal if the actual value of the signal is larger than 2.5 standard deviations (σ) above the mean. In this section, the filament and background case for synthetic filaments are related to the mean and σ of experimentally measured profiles. The aim of relating these quantities is to identify the magnitude of filament amplitudes $T_\mathrm{e,fil,0}$ and $n_\mathrm{e,fil,0}$ that corresponds to a 2.5σ intensity perturbation in the experimentally measured signal.

The synthetic filament analysis allows to determine a relative intensity perturbation $\frac{\Delta I}{I} = \frac{I_\mathrm{fil+bg} - I_\mathrm{bg}}{I_\mathrm{bg}}$. In order to obtain a comparable quantity from experimental data, the standard deviation σ_exp of the experimentally measured time traces can be employed and normalized to a background value. This factor

$$\kappa_{int} = \frac{\sigma_\mathrm{exp}}{\overline{I_\mathrm{exp}}},$$

with the experimental mean intensity $\overline{I_\mathrm{exp}}$, represents the typical relative fluctuation level at the considered LOS. It allows to relate the relative intensity perturbation $\frac{\Delta I}{I}$ of the synthetic filaments to the standard deviation obtained from experimental data. The factor κ_{int} depends on the selected LOS, the specific

plasma discharge conditions and the background profiles, changing significantly with them.

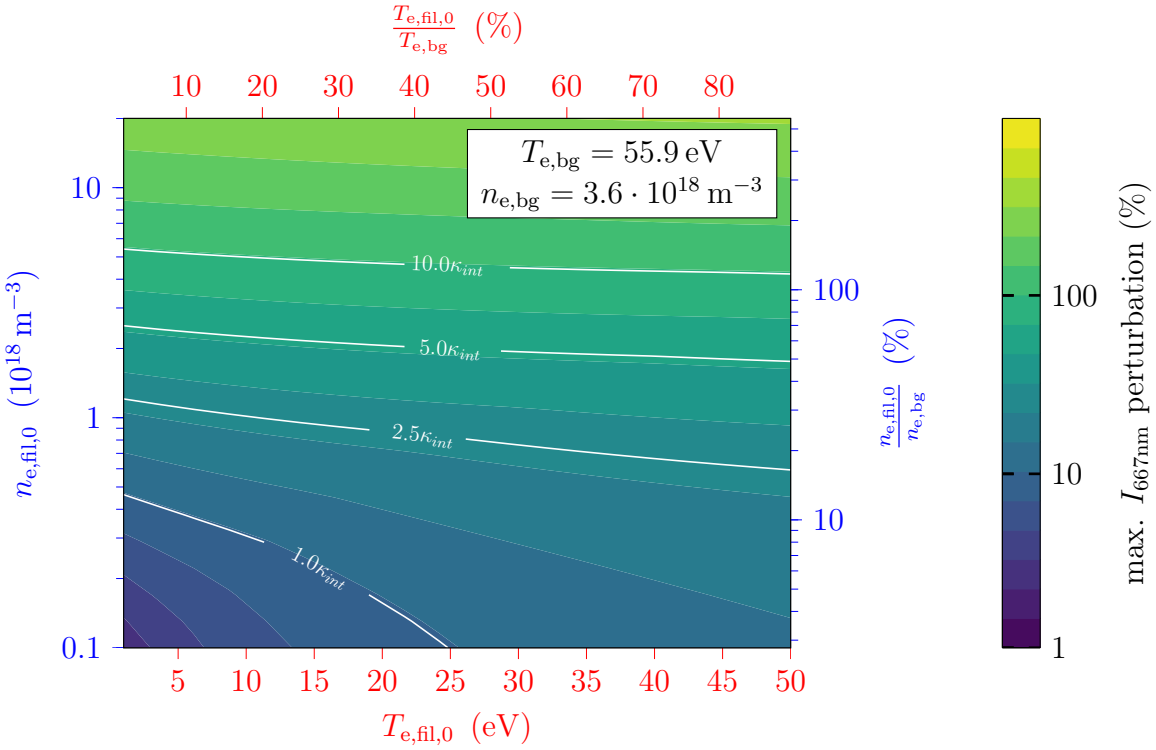

Figure 4.13.: The figure shows the 2D map for the relative intensity perturbation of the 667 nm line. Different values of κ_{int} are displayed in the plot. A filament with an intensity perturbation above $2.5\kappa_{int}$ would be identified as a filament in the experiment according to the 2.5σ criterion.

In Figure 4.13, the intensity perturbation of the 667 nm line by filaments with different temperature and density amplitudes is displayed. In addition, contour lines of different multiples of the relative fluctuation level κ_{int} are shown. These lines represent the minimum filament amplitude $T_{e,fil,0}$ and $n_{e,fil,0}$ required to generate an intensity response, which is sufficient to surpass the respective multiple of κ_{int}. For example, the 2.5σ criterion to select filaments in the experiment is represented by the $2.5\kappa_{int}$ line. Filaments with an amplitude that is located below this line in the 2D plane would give rise to an intensity perturbation below 2.5 standard deviations and, therefore, cannot be identified as filaments in the experimental measurement if the 2.5σ criterion is employed. In other words, only filaments with an density amplitude larger $n_{e,fil,0} > 1 \cdot 10^{18}\,m^{-3}$ would be identified

as filaments when the 2.5σ threshold is applied. For the filament temperature in this case, there is practically no minimum required. This is important, for example, in conditional averaging (explained in Section 6.1.4), where the average over multiple filament intensities is used. Due to this restriction, only a share of the possible filament $T_{\mathrm{e,fil,0}}$ and $n_{\mathrm{e,fil,0}}$ amplitudes is included in the averaging.

The κ_{int} factor gives a rough estimate for the measurement capabilities but has multiple problems. It is intended to relate the standard deviation in the experiment with the intensity of the background profiles. But as there is no definition of the background profiles in the experiment, the mean intensity $\overline{I_{\mathrm{exp}}}$ is used to normalize the standard deviation. Choosing the median or the mean intensity for the selected case does not make a significant difference.

The kind of analysis as shown in Figure 4.13 can be used to determine what range of experimental filament amplitudes can be detected for a selected plasma discharge.

5. Reconstruction of 2D synthetic filaments

Using the extended CRM (see Section 3.1.4), a reconstruction algorithm is developed in order to reconstruct filament properties. In the following, the reconstruction algorithm is explained and validated by means of synthetic filaments. Finally, the filament reconstruction with the static model is described.

Parts of the findings have been published in *D. Wendler, et al.; Two-dimensional reconstruction of filament temperatures and densities with the thermal helium beam at ASDEX Upgrade. Phys. Plasmas 1 September 2023; 30 (9): 092509.* [134]

5.1. Filament reconstruction algorithm

A reconstruction algorithm is used to obtain filament properties from input intensities, which originate either from synthetic or measured data. The algorithm assumes a circular filament, identically parametrized as the artificial filaments (see section 4.1). Besides the input intensity, the reconstruction needs a background profile. Analog to the artificial filaments in section 4.1, a 1D THB profile, calculated from time points without filaments, is mapped according to the magnetic equilibrium into the y_{bco}-z_{bco} plane. For the discharge evaluated in this chapter, discarding the filament time points for the background profiles doesn't make a difference, which is displayed in appendix A.2.

To improve and accelerate the reconstruction, the filament parameter space is restricted by the following boundaries shown in Table 5.1.

Table 5.1.: Boundaries for the filament reconstruction algorithm. For the filament position, the maximum perturbation of the density-sensitive line ratio is used to obtain an initial value.

$T_{\mathrm{e,fil,0}}$:	$[1\,\mathrm{eV}$ to $50\,\mathrm{eV}]$
$n_{\mathrm{e,fil,0}}$:	$[0.1 \cdot 10^{18}\,\mathrm{m}^{-3}$ to $20.0 \cdot 10^{18}\,\mathrm{m}^{-3}]$
σ_{fil} :	$[0.1\,\mathrm{cm}$ to $2.5\,\mathrm{cm}]$
z_{bco} :	pos. R_{ne} +- $0.75\,\mathrm{cm}$
y_{bco} :	pos. R_{ne} +- $0.75\,\mathrm{cm}$

For the position of the filament, the maximum of the relative fluctuation of the density-sensitive line ratio (R_{ne}) is used as an approximation in order to obtain a first guess of the filament coordinates. Based on these coordinates, the boundaries are set in the z_{bco}-y_{bco} plane.

Using the parametrized filament (given by $T_{\mathrm{e,fil,0}}$, $n_{\mathrm{e,fil,0}}$, σ_{fil}, z_{bco} and y_{bco}) and the background profiles, the extended CRM (see subsection 3.1.4) forward calculates the intensities for each LOS. These forwardly calculated intensities are together with the input intensities are used in the following.

As main element of the reconstruction algorithm, a difference function is defined, which serves as a cost function. It gives the agreement between the reconstructed intensities and the input intensity (in this case, the intensity from the synthetic filament). The difference function is constructed from the difference between the measured and forward-modeled data.

$$
\begin{aligned}
c = & \sum_{\mathrm{5x5grid}} \log\left(1 + \left(\frac{R_{\mathrm{Te,input,i}} - R_{\mathrm{Te,model,i}}}{\Delta R_{\mathrm{Te,input,i}}}\right)^2\right) \\
& + \sum_{\mathrm{5x5grid}} \log\left(1 + \left(\frac{R_{\mathrm{ne,input,i}} - R_{\mathrm{ne,model,i}}}{\Delta R_{\mathrm{ne,input,i}}}\right)^2\right) \\
& + \sum_{\mathrm{5x5grid}} \log\left(1 + \left(\frac{\left(\frac{I_{728\,\mathrm{nm}}}{I_{587\,\mathrm{nm}}}\right)_{\mathrm{input,i}} - \left(\frac{I_{728\,\mathrm{nm}}}{I_{587\,\mathrm{nm}}}\right)_{\mathrm{model,i}}}{\Delta\left(\frac{I_{728\,\mathrm{nm}}}{I_{587\,\mathrm{nm}}}\right)_{\mathrm{input,i}}}\right)^2\right) \\
& + \sum_{\mathrm{5x5grid}} \log\left(1 + \left(\frac{I_{587\mathrm{nm,input,i}} - I_{587\mathrm{nm,model,i}}}{\Delta I_{587\mathrm{nm,input,i}}}\right)^2\right)
\end{aligned}
$$

The cost function c is calculated for each LOS in the 5×5 grid, consisting of one intensity shape (587 nm) and three line ratios ($\frac{I_{728\,\mathrm{nm}}}{I_{587\,\mathrm{nm}}}$, $\frac{I_{667\,\mathrm{nm}}}{I_{728\,\mathrm{nm}}}$ (R_{ne}) and $\frac{I_{728\,\mathrm{nm}}}{I_{706\,\mathrm{nm}}}$ (R_{Te})), these are the identical line ratios as used for the 1D profile reconstruction (see subsection 3.1.3). Due to a broken optical fiber, one line of sight (LOS) in the upper right corner of the inner 3×3 grid is missing and, therefore, not used in the reconstruction algorithm. The missing LOS can be seen in figure 6.5. For each quantity, the difference between the measurement and the forward model is calculated, normalized by the standard deviation of the experimental quantity. In the last step of calculating the cost function, the difference for each LOS is summed up.

The reconstruction algorithm is initialized by an equidistant grid of four points in the direction of each of the five reconstructed parameters. The difference function is called for each grid point, which is computationally heavy. These points

are then used to set up a Gaussian process [155]. After the initialization,the Gaussian process uses the expected improvement to simultaneously minimize the absolute value of the difference function and reduce the uncertainties of the Gaussian Process. The predicted point from the expected improvement is inserted into the difference function and added to the Gaussian process. This step is repeated for 200 iterations. After the Gaussian Process Regression, the fine tuning is performed using a gradient-descent algorithm. The uncertainties are determined after the reconstruction by calculating the Hessian matrix for the resulting point.

5.2. Validation of the reconstruction algorithm

To test the performance and accuracy of the reconstruction algorithm, it is applied to synthetic data. This provides a test bed where a defined input can be compared to the reconstruction results.

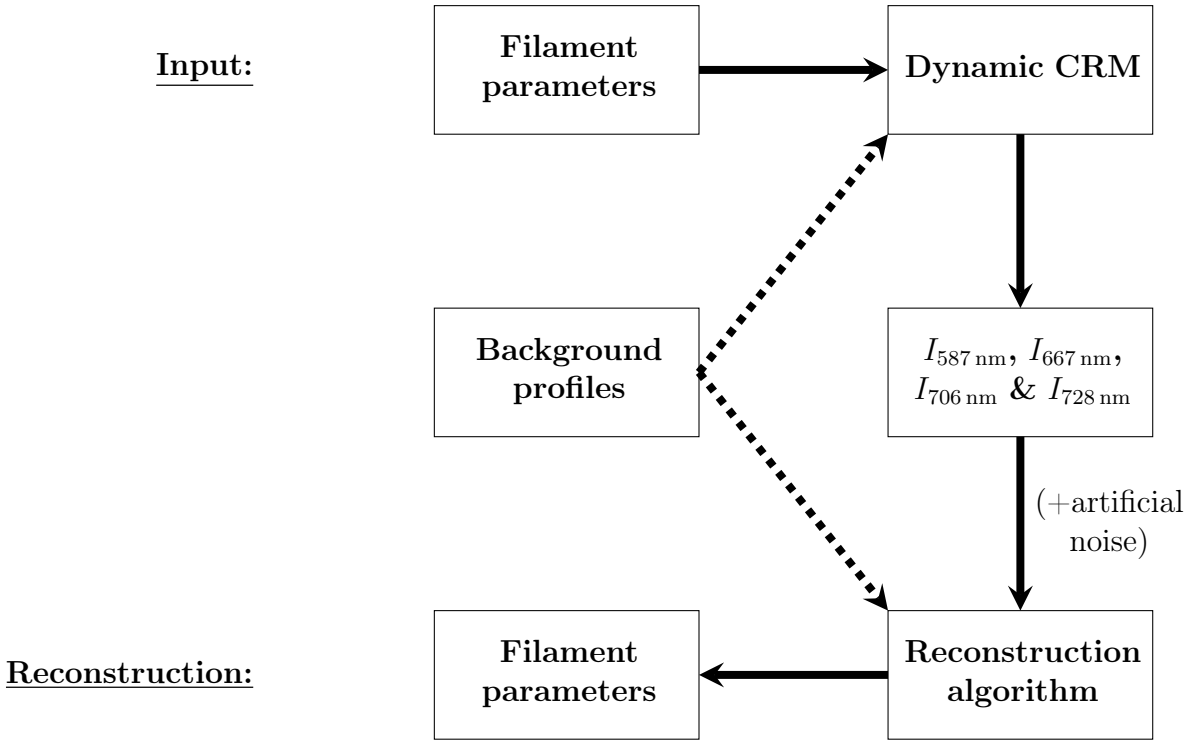

Figure 5.1.: Process scheme to compare the reconstructed filament amplitude with a given input for the dynamic CRM.

The process scheme for the comparison is displayed in Figure 5.1. A filament, with a given temperature and density amplitude is handed over to the dynamic CRM. Together with the constant background profiles, the model calculates the intensities for each LOS. These intensities are either passed on with noise or without any change. Together with the background profiles, the intensities are then handed to the reconstruction algorithm, which reconstructs the filament properties.

In table 5.2, a given filament is reconstructed for two cases, once with and without random noise. The background profiles are identical to the ones for the synthetic filaments, described in Section 4.1.

Table 5.2.: Results of the synthetic filament reconstruction.

	Input	Reconstruction (no noise)	Reconstruction (10% random noise)
$T_{\mathrm{e,fil}}$	$20.0\,\mathrm{eV}$	$19.69\,\mathrm{eV}$	$(10.6 \pm 3.3)\,\mathrm{eV}$
$n_{\mathrm{e,fil}}$	$2.0 \cdot 10^{18}\,\mathrm{m}^{-3}$	$1.94 \cdot 10^{18}\,\mathrm{m}^{-3}$	$(2.1 \pm 0.1) \cdot 10^{18}\,\mathrm{m}^{-3}$
σ_{fil}	$0.27\,\mathrm{cm}$	$0.36\,\mathrm{cm}$	$(0.35 \pm 0.02)\,\mathrm{cm}$
z_{bco}	$8.5\,\mathrm{cm}$	$8.50\,\mathrm{cm}$	$(8.57 \pm 0.03)\,\mathrm{cm}$
y_{bco}	$0.0\,\mathrm{cm}$	$-0.01\,\mathrm{cm}$	$(-0.10 \pm 0.03)\,\mathrm{cm}$

It can be seen that the reconstruction algorithm can reproduce the filament properties. The most significant deviation is observed for the filament size, whose resolution is limited by the LOS spacing of 3 mm. As the intensity of the filament changes drastically with the background (see Section 4.6), the filament position is recovered very well. Besides this, the density amplitude is recovered better than the temperature one, which is caused by the higher sensitivities of the helium transitions to the density. In the case of the random noise, the temperature amplitude is poorly reconstructed, which is not fully captured by the resulting uncertainty. This is an extreme outlier, that didn't appear in similar runs. Similar to the case without noise, the density amplitude, position, and size are recovered well.

These examples show that the dynamic model can reconstruct the filament quantities. Due to the weak response of the intensity and R_{Te} on the filament temperature, the highest relative uncertainties are on $T_{\mathrm{e,fil}}$. Due to the finite LOS spacing, the size σ_{fil} is reconstructed badly for these small filaments.

5.3. Reconstructing synthetic filament data with the static model

As stated in Section 3.1.3, the dynamic CRM was developed to compensate for an artificial temperature rise of the profiles in the far-SOL caused by too low transition rates between the spin system resulting from a low density. For high densities, this requirement might be fulfilled, so that the static CRM would be sufficient to be applied for the T_e and n_e calculation of filaments. To check this, 1D profiles with and without a filament are analyzed below by applying the static model to the synthetic data.

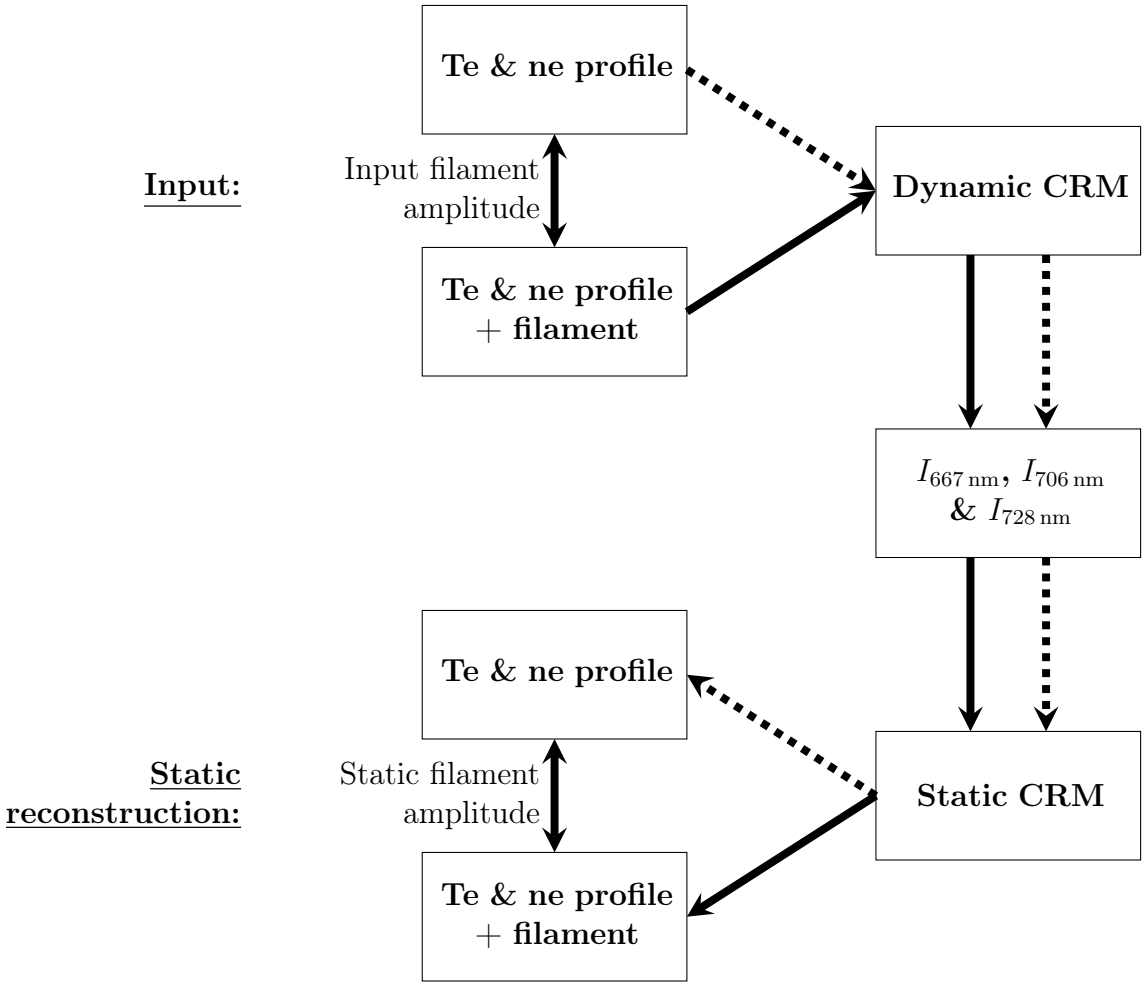

Figure 5.2.: Process scheme to compare the filament amplitude gained with the static model to the input data.

As input for the analysis, 1D T_e and n_e profiles with and without a filament are handed to the dynamic CRM. The resulting intensities are then used in the static model, which reconstructs T_e and n_e in the corresponding cases. As a final step, the static filament amplitude is determined by subtracting the static profile without filament from the static profile with filament. This allows to compare the input filament amplitude versus the statically reconstructed one for different background profiles and filament positions as well as filament amplitudes. This process scheme is displayed in Figure 5.2.

In Figure 5.3, the one-dimensional with and without filament as used in the sensitivity study presented in Section 4.1, is displayed. This corresponds to a filament in the near-SOL. The profiles are displayed along the injection axis z_{bco}. In Figures 5.3a and 5.3b the input T_e and n_e background profiles are shown and compared with the reconstructed profiles using the static CRM. The density profiles are very similar, while the reconstructed temperature profiles show the expected artificial temperature rise in the far SOL at $z_{\mathrm{bco}} \leq 7.5\,\mathrm{cm}$.

In Figure 5.3c and 5.3d, the profiles with filament are compared. As the relative filament amplitude is small, adding the filament to the background only slightly modifies the resulting profiles. For T_e and n_e, the profiles with filament are still similar for the input and the static reconstruction. By subtracting the background profiles from the reconstructed profiles with filaments, the filament amplitudes are determined as displayed in panels 5.3e and 5.3f. While the density amplitude is nearly a perfect match, the filament T_e amplitude from the static model is slightly higher, but still within the usual range of differences between the static and dynamic CRM

For a shifted background, corresponding to filaments in the far-SOL, the 1D profiles are displayed in Figure 5.4. The profiles originate from the discharge #40425 in the interval from 4.78 s to 5.78 s, which is the experimental interval that is further described in subsection 6.1.1 and analyzed in section 6.2. While the density profiles do still match well, there are major differences for the temperatures. In Figure 5.4a, one can see that the background temperatures differ for a wide radial range. The artificial temperature rise is observed at the entire range, with the static reconstructed profile converging to the input only for high z_{bco} values. For the position below $z_{\mathrm{bco}} = 8\,\mathrm{cm}$, the line ratios are outside the range of precalculated values for the static models, as the system is far away from CRE.

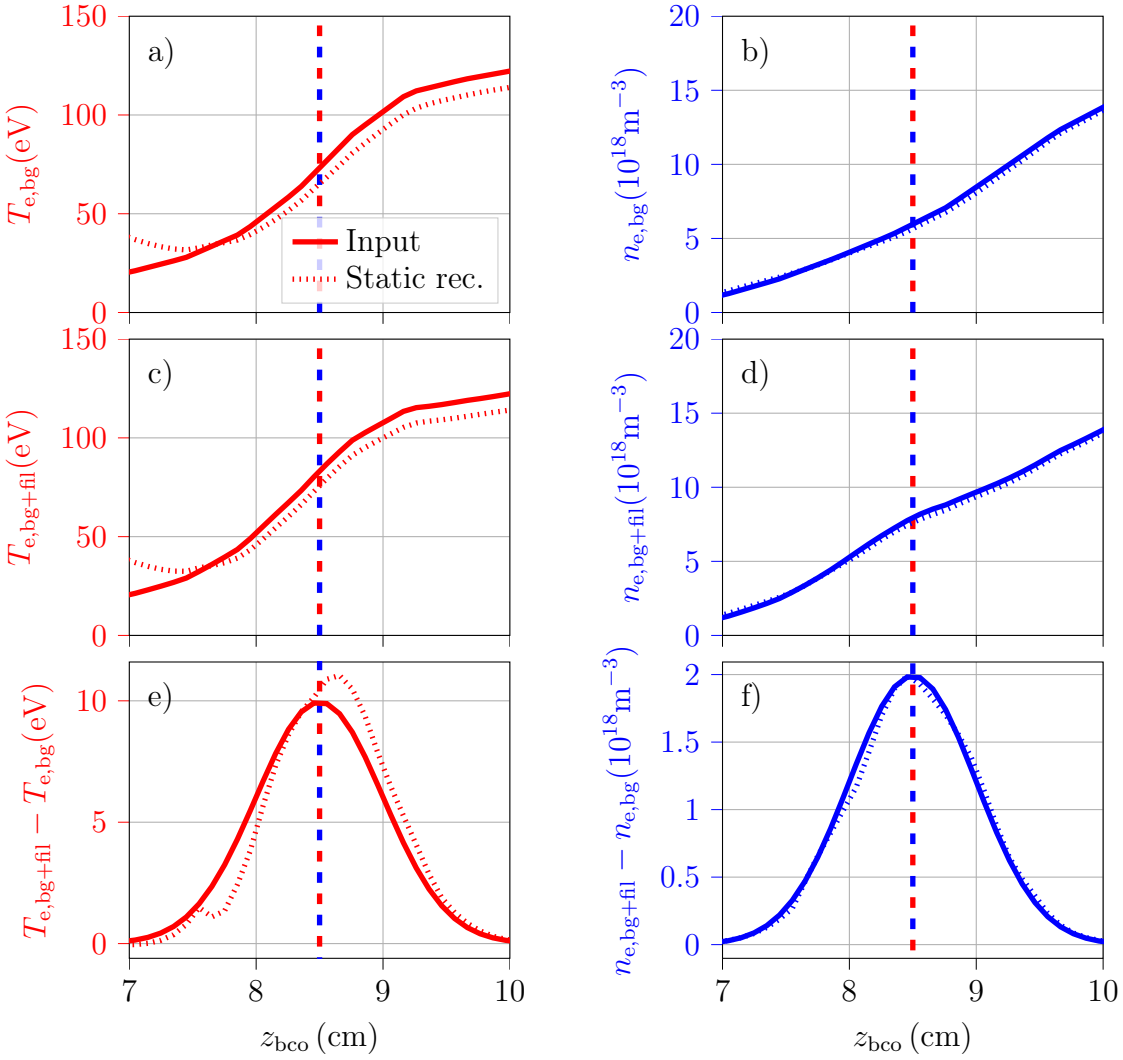

Figure 5.3.: Comparison between the input profiles and the static reconstruction, without filament (a,b) and with filament (c, d). The difference of pure background profiles and profiles including the filament results in the filament amplitude plotted in e and f. The background profiles are from #37021, t=2.2 s to 3.9 s.

The T_e profiles with filament are displayed in Figure 5.4c. It shows, that the static model exhibits the artificial temperature rise before the filament position. At the filament position, the static model converges to the input profiles. Behind the filament position, the static model shows a lowered T_e for a short distance, as explained below.

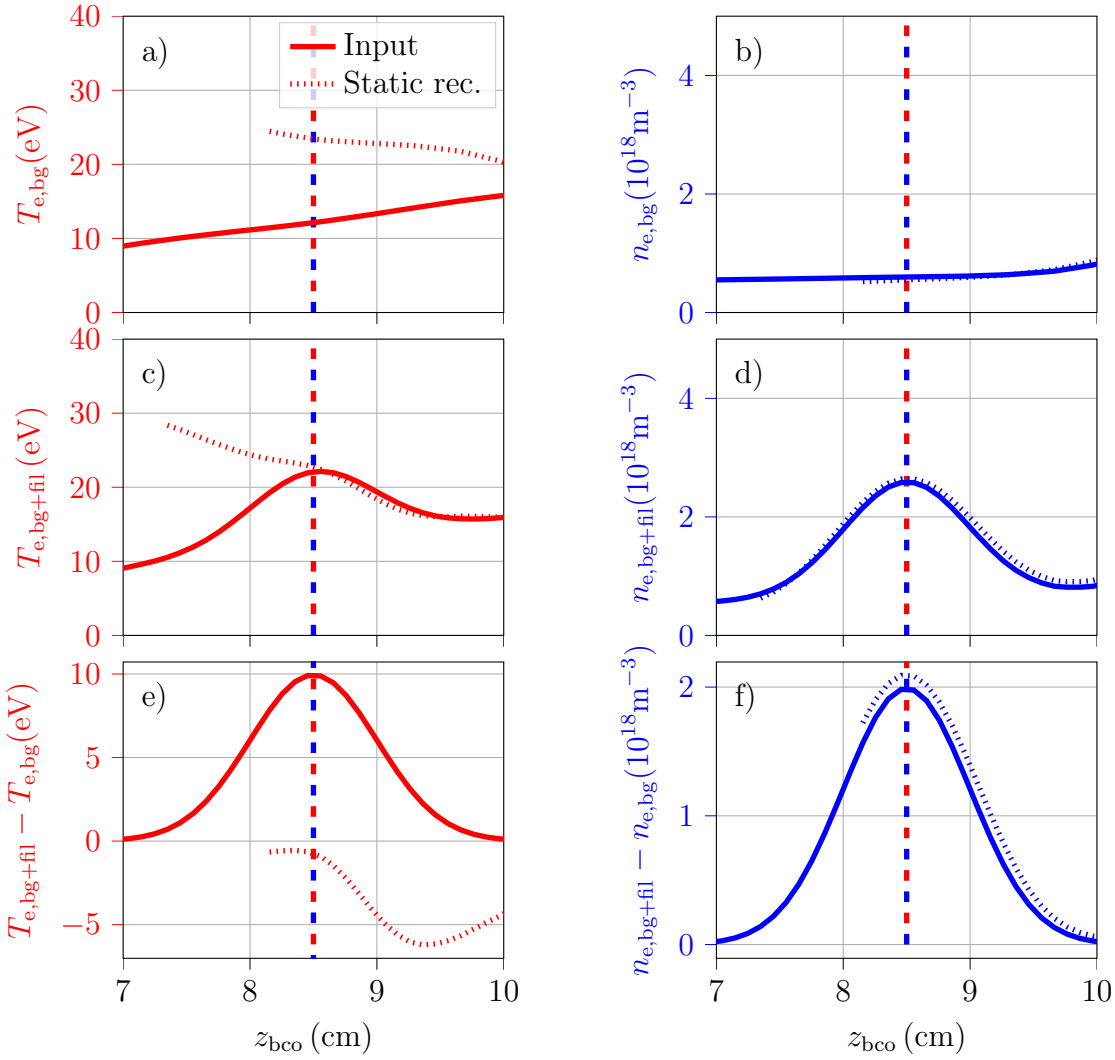

Figure 5.4.: Comparison between the input profiles and the static reconstruction. The forward model calculates intensities from the input profiles, that are then fed into the static CRM. For the given case, subtracting the background profiles from the one with filament leads to a negative temperature perturbation. The background profiles are from #40425, t=4.78 s to 5.78 s.

In the Figure 5.4e and 5.4f, the filament amplitude is calculated by subtracting the profiles with filament from the profiles without. As in the other case, the filament density agrees very well. But there are significant differences for the temperature amplitude, which can be seen in Figure 5.4e. The static reconstruction

produces a negative temperature amplitude of the filament. This behaviour, caused by the state mixing, can be explained by the following steps:

- For the positions radially outside the filament, both the case with and without filament overestimate the temperature because the condition of a CRE is not fulfilled due to the low density. That the condition for a CRE is not fulfilled, is cauesd by too low triplet populations, leading to the temperature overestimation by the static model.

- At the filament position, the density increase of the filament shifts the atomic system into a CRE. This can be seen in Figure 5.4c, where the static model exactly reconstructs the input profile. As the background density stays low, the background profile reconstructed with the static CRM reconstructs too high temperatures. By subtracting the profile with filament, with the correct temperature, from the background profile, with a too-high temperature, results in a slightly negative temperature perturbation.

- Radially inside the filament position, the total density decreases, caused by the decreasing filament amplitude $n_{\mathrm{e,fil}}$. The atomic states are for the filament case no longer in a CRE as the temperature decreases as well. The triplet populations are now too high compared to the CRE due to the reduced temperature and the reduced collisions. By subtracting the static profiles with filament, having a too low temperature, from the background static profiles, having a too high temperature, a negative temperature perturbation arises radially inside the filament position. This can be seen in figure 5.4c.

- With increasing background densities, the condition of a CRE for the inner positions is fulfilled again, leading to an accurate temperature reconstruction with the static model. This happens radially inside the displayed positions.

This case shows, that the static model can lead to wrong and even negative temperature perturbations for filament analysis. The reason for this is, that the increased density by the filament can shift an unequilibrated atomic system into a CRE. Therefore, a dynamic CRM is required to reconstruct filament T_{e} and n_{e} at low background densities. To further investigate the temperature deviation, another case is compared in Figure 5.5. The filament position is moved by 1 cm radially outwards in comparison to the case in Figure 5.3. This shift in the filament position leads to lower background temperatures and densities. In contrast to the background values, the filament T_{e} and n_{e} amplitude is increased.

As in the two other cases, the density is reconstructed well, but has a small deviation in the absolute amplitude. However, the filament temperature is underestimated by almost 25 %.

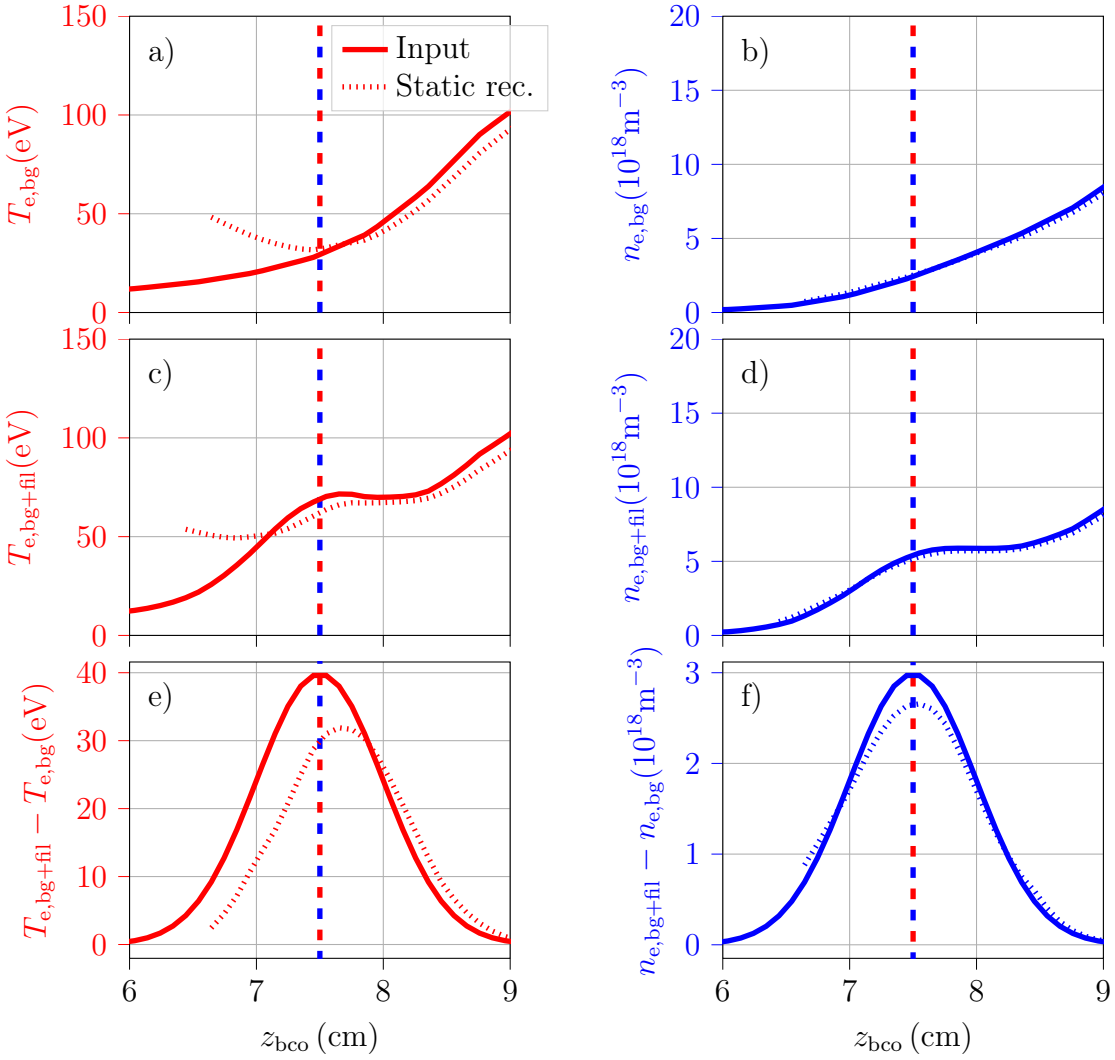

Figure 5.5.: Comparison between the input profiles and the static reconstruction. The forward model calculates intensities from the input profiles, that are then fed into the static CRM. By subtracting the cases with and without filament, it can be seen that the static model reconstructs lower values for the T_e and n_e perturbation. The background profiles are from #37021, t=2.2 s to 3.9 s.

The details of the three cases, at the filament position, are summarzed in table 5.3. It shows that the density is reconstructed in all cases very well. For the temperature, the values agree only well in the near-SOL case for the background and the filament amplitude.

Table 5.3.: Comparison between the three reconstruction cases for the static CRM. For the temperature and density, the values at the filament position are compared.

		$T_{\mathrm{e,fil}}$ (eV)	$T_{\mathrm{e,bg}}$ (eV)	$\frac{T_{\mathrm{e,fil}}}{T_{\mathrm{e,bg}}}$ (%)	$n_{\mathrm{e,fil}}$ ($10^{18}\,\mathrm{m}^{-3}$)	$n_{\mathrm{e,bg}}$ ($10^{18}\,\mathrm{m}^{-3}$)	$\frac{n_{\mathrm{e,fil}}}{n_{\mathrm{e,bg}}}$ (%)
near-SOL	input	11	77	14	2.0	5.8	34
	static rec.	10	69	15	2.0	5.5	36
far-SOL	input	10	12	83	2.0	0.6	333
	static rec.	-1	23	-4	2.1	0.6	350
intermediate case	input	40	31	129	3.0	2.6	83
	static rec.	31	33	94	2.8	2.7	103

To summarize, the comparison between the dynamic CRM and the static CRM leads to the following points:

- n_{e} is reconstructed by the static model in all cases very well. This is caused by the fact, that the density-sensitive line ratio (R_{ne}) is formed from two singlet helium states, and therefore not influenced by the state-mixing.
- The temperature is successfully reconstructed for cases with high background densities, including the background profile and the filament amplitude.
- For low background densities, the background profiles create an artificial temperature rise. If the condition of a CRE is then fulfilled by the filaments density perturbation, the static model leads to a negative temperature perturbation.
- For cases with densities in-between, the static model causes a temperature underestimation. Therefore, for medium densities, it is necessary to use a dynamic CRM. Otherwise the temperature estimation fails.
- Besides the absolute values of the background, the possibility of reconstructing filaments with the static model also depends on the filament amplitudes and the gradients of the background profiles. Steep gradients at low n_{e} require a dynamic model. Only if the background profiles of the static and dynamic CRM are equal, the static model can be used for the filaments without restrictions.

This behavior could explain negative temperature perturbations, as observed in Ref. [119] and discussed in section 2.6.

In the near-SOL the static CRM is applicable due to the high density of the background. As mentioned in Section 4.6, filaments are difficult to detect in the near-SOL, so typical filament measurements are performed in the far-SOL. A dynamic CRM is needed for this radial region or regions with similar densities.

In the next chapter the reconstruction algorithm with the dynamic CRM is applied to experimental filaments.

6. Filament reconstruction from experimental data

In this chapter, the reconstruction of filament properties from experimental data is presented. In the first approach, this is done by conditional averaging. This approach allows to analyze a time trace, and the measured decay rates are compared to analytical models for the filament temperature and density. In a second approach, individual filaments are analyzed and compared to the result from conditional averaging.
Parts of the findings have been published in: *D. Wendler, et al.; Two-dimensional reconstruction of filament temperatures and densities with the thermal helium beam at ASDEX Upgrade. Phys. Plasmas 1 September 2023; 30 (9): 092509.* [134].

6.1. Selected discharge and data processing

In this section, the plasma discharge is presented, for which the THB data is analyzed. The data analysis methods used to extract the filament properties are introduced, especially CA and the 2.5σ criterion.

6.1.1. I-phase discharge #40425

For the experimental evaluation, the I-phase discharge #40425 is chosen. Because of the regular I-phase burst, there are many filaments in the interval. For the discharge, the subinterval from 4.78 s to 5.78 s is selected for the evaluation. In the interval, the plasma is heated with 840 kW of ECRH power, having a toroidal field strength on the magnetic axis of -2.5 T and a plasma current of 800 kA. The edge safety factor is $q_{95} = 4.8$, and the separatrix at the outboard midplane is positioned at $R_{\mathrm{maj}} = 2.09$ m. The main ions species of the plasma is deuterium, having a line averaged density of $\overline{n_{\mathrm{e,core}}} = 5.6 \cdot 10^{19}\,\mathrm{m}^{-3}$. The plasma stored energy is $W_{\mathrm{mhd}} = 0.2$ MJ. All parameters were kept constant during the interval. The time-averaged background profiles of the interval are displayed in figure 6.1.

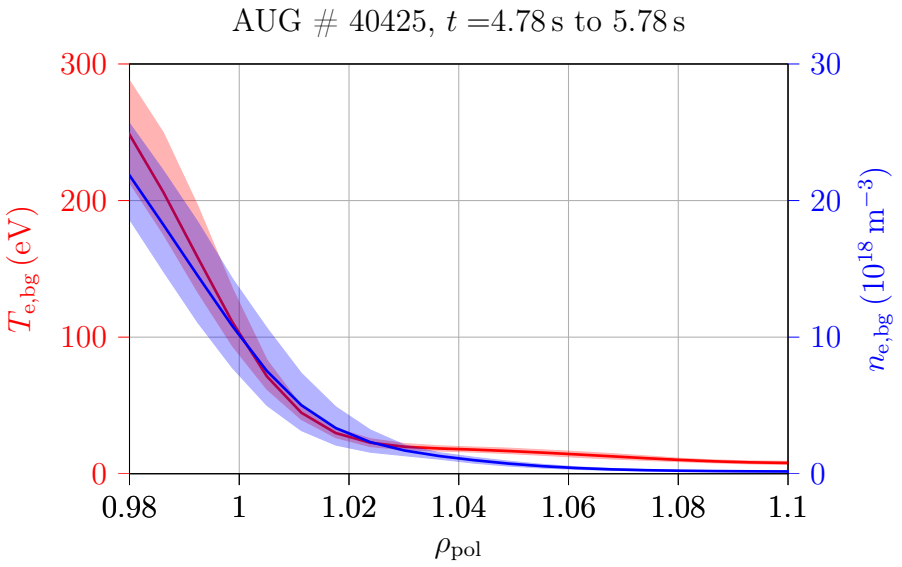

Figure 6.1.: Background profiles of temperature and density over the coordinate ρ_{pol}. The shaded area corresponds to the standard deviation of the profiles, that are evaluated each 1 ms within the given time-span. Here the helium injection is from the right to the left.

6.1.2. Raw data processing

The four measured wavelengths for each LOS are processed over multiple steps to evaluate the THB measurement data. The first steps of the processing are similar between the filament analysis and the background profiles. It includes:

1. signal calibration as described in Refs. [126, 156],

2. binning 5-time points together to improve the SNR ratio,

3. subtracting the background intensity, determined in the beam-off phases.

In the following steps, only the intensities from the beam-on phases (the duty cycle in this discharge was chosen to be 60 ms beam-on, 40 ms beam-off) are further processed. For the filament analysis, the resulting intensities of each LOS are smoothed using a Gaussian filter with a length of seven time points (corresponding to 35 µs) and a width of one time point (5 µs). All these steps are performed to improve the SNR ratio of the raw signal. The resulting intensity is then used to apply the 2.5σ criterion, which is described in the next subsection

6.1.3. 2.5σ criterion

As described in section 2.6, initial filament measurements were typically performed with Langmuir probes. As these measurements had a fixed position with no spatial components, a criterion was required to distinguish filament time points from random noise in a measured time trace.

Random noise leads to a Gaussian distribution of the measurement signal. For a Gaussian distribution, the higher order moments of the distribution, skewness and kurtosis, are zero. Experimental data typically deviates from the Gaussian distribution due to the intermittent appearance of filaments. Accordingly, both moments are non-zero and have been used to describe the intermittency of the transport [157, 158, 159].

The Gaussian distribution is parametrized by the standard deviation (σ). For this Gaussian distribution, 99 % of the measurement points are in the interval from -2.5σ to 2.5σ. So by random noise solely, only 1 % of measurement points would be out of this interval. For an experimental signal distribution consisting of random noise and filamentary transport, the ratio of points out of this 2.5σ interval is higher due to the finite skewness and kurtosis. Even though the background noise in the experiment differs from random noise, the 2.5σ criterion is used to discriminate large events, which are considered as filaments. Therefore, it is more likely that a measurement point above 2.5σ is from a filament than from the background noise. The corresponding figures of the intensity distribution and the fitted Gaussian are displayed in appendix A.4. In the experiment, the 2.5σ criterion is used to define filaments. More specifically, if a measured signal is above 2.5 σ of the mean value, the signal time point is defined as a filament time point. The choice of 2.5 σ is arbitrary but has proven to be useful in filament studies at AUG. Studies at other tokamaks have partially applied larger or smaller detection thresholds [160, 107, 161, 162]. The filament detection by means of the 2.5σ criterion depends on the underlying distribution function present in the considered measurement signal. Since this distribution varies for different local plasma conditions, the diagnostic used and the pre-processing of the data, the selected filaments might vary as well, depending on the given circumstances, despite the same 2.5σ criterion was applied. Therefore, this is a somewhat arbitrary, albeit statistically well founded, criterion, and comparisons between different diagnostics or different plasma conditions should be used with care. The range of detectable filament amplitudes above the 2.5 σ threshold is theoretically approached for synthetic filaments in Section 4.7, and the concept is validated with the experiment in Section 6.4.1.

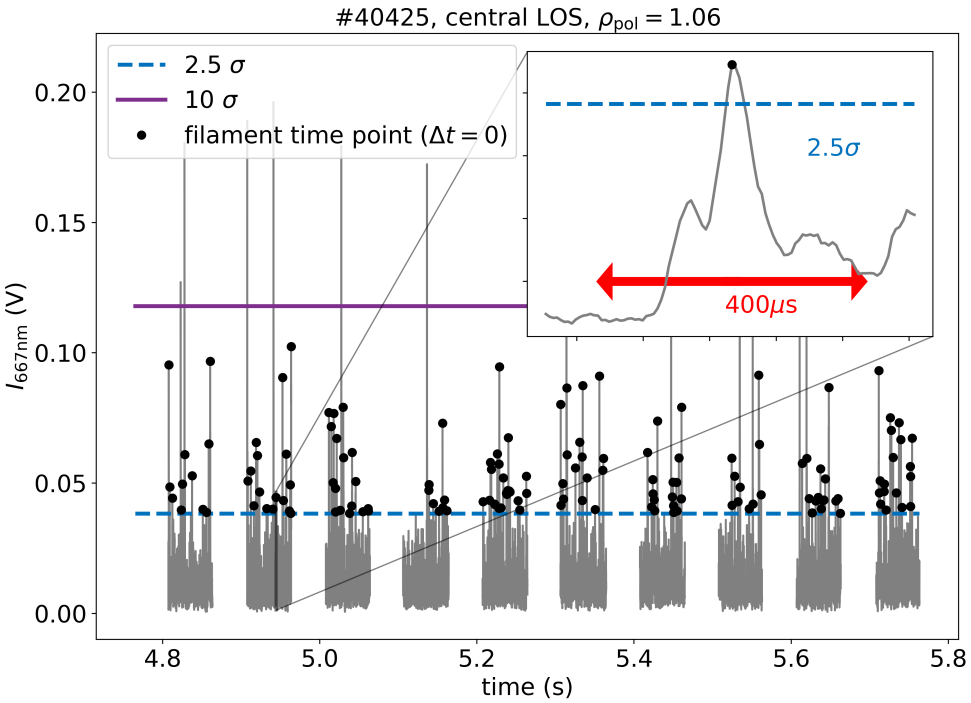

Figure 6.2.: The figure shows the 667 nm intensity time trace (grey) from the central LOS in the evaluated time interval. In the inset box, it can be seen that the filament time point (black dot) is the point of maximum intensity in an interval above the 2.5σ criterion. Filaments with intensities above 10σ are discarded to reduce the influence of extreme outliers. The helium puffing is modulated with a frequency of 10 Hz, and the beam-off time points are discarded.

In the filament evaluation, the 2.5σ criterion is applied to the THB time trace in the first steps from Section 6.1.2. The central LOS of the 5×5 grid is used for this evaluation and serves as a reference LOS. Due to a positive correlation with T_e and n_e, the 667 nm line is chosen (see Section 4.3). As there are intervals with multiple time points above the threshold, a single time point uniquely assigned to the filament needs to be selected. In this work, the time point of the maximum amplitude is selected as the filament time point. This selection is displayed in Figure 6.2. The dashed lines indicate the 2.5σ criterion. The inset shows a time window of a single filament and the maximum (black dot) determining the filament time point ($\Delta t = 0$).

In total, the 2.5σ criterion identifies 185 filaments in the interval. A filter discards 11 filaments with intensities above 10σ. This marginally affects the intensity averaging described in the next section, and the final reconstruction result, but is routinely used in order to exlude very large events, which might impact the final physics results (see also Section 6.3.2). The 174 filaments detected in the interval and evaluated in the next steps correspond to a filament frequency of $f_{\mathrm{fil}} = 290\,\mathrm{Hz}$.

6.1.4. Conditional averaging

To improve the signal quality of the filaments, conditional averaging (CA) is performed [113, 163]. For this purpose, subintervals from $\Delta t = -200\,\mu\mathrm{s}$ to $\Delta t = 200\,\mu\mathrm{s}$ around the filaments are selected. By coherently averaging each time point Δt separately, a single conditionally averaged time trace centered around $\Delta t = 0$ is obtained. This method intrinsically assumes that all filaments are sufficiently similar, i.e. obey the same size and dynamics aside from small statistical deviations. The conditional averaged intensities of the 174 filaments detected in the selected time interval are displayed in Figure 6.3.

In the intensity time traces, different characteristics can be seen. Most filaments are in a narrow band for all four helium transitions, with only relatively few outliers. In black, the mean intensities are displayed. For these mean curves, one can see that the rise and fall of the peak have different exponential decay times. This is similar to GPI measurements, showing that the rise and fall times are anti-correlated with the number of filaments in the discharge [164].

Comparing the curves of the four different helium intensities, one can see that they have different relative perturbations caused by the filament. Because of these different relative perturbations, the line ratios are likewise perturbed by the filament, as seen in section 4.4 for synthetic filaments. For the processing of the line ratios, two process orders are possible. This are

- first calculating the line ratios from raw intensities and then perform the CA, or
- first CA of the raw intensities and then calculating the line ratios.

Both processes are displayed in Figure 6.4, along with the line ratios of the individual filaments.

These two procedures lead to very similar results. Only for very large timesteps, both process orders cause a measurable difference. To reduce the influence of the weak 728 nm line, the line ratios in the evaluation are formed by first averaging the intensity and then forming the ratio. By reconstructing the filament properties described in the next section, the results at the trigger time point $\Delta t = 0$ are very similar but differ in their temporal evolution between both process orders.

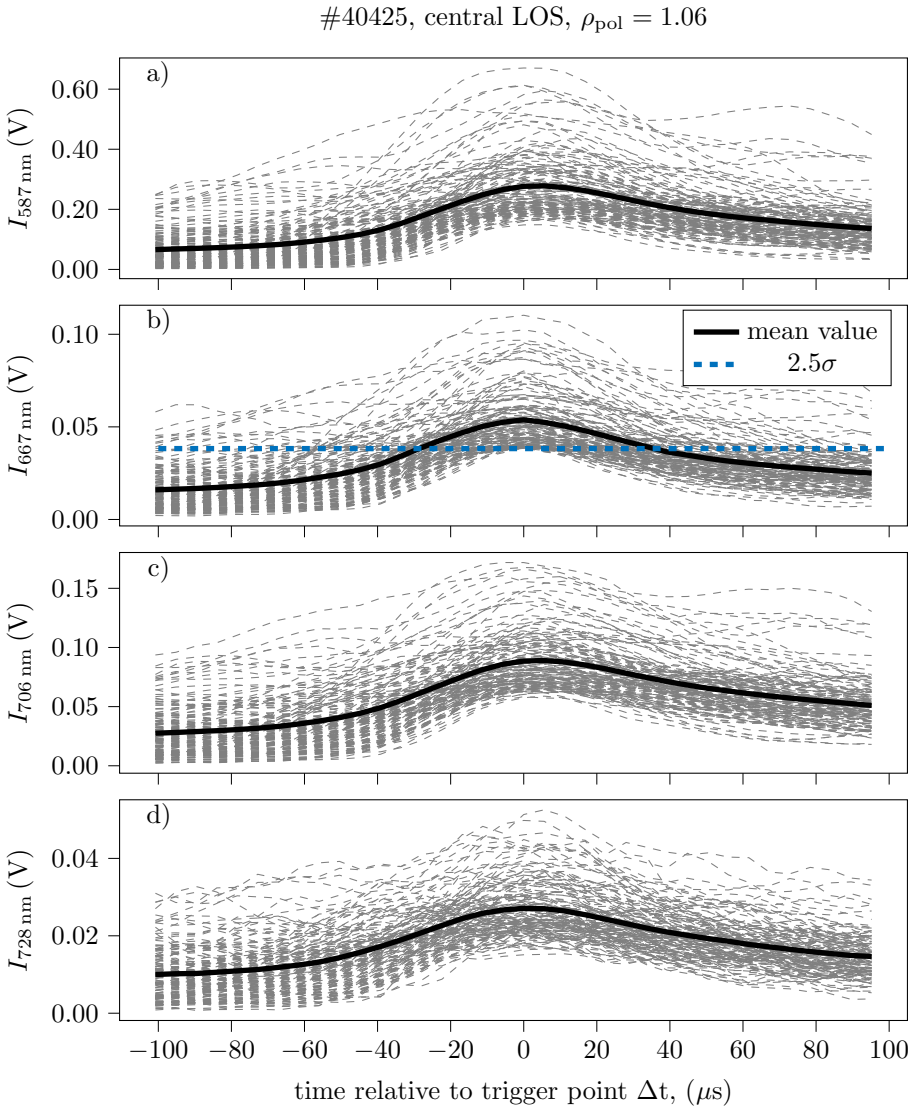

Figure 6.3.: Intensity time traces of the individual filaments (grey) at the central LOS, in the interval from 4.78 s to 5.78 s of #40425. For the 667 nm line, used for triggering and displayed in b), the 2.5σ criterion is displayed. Resulting from averaging of the individual filaments, the mean intensity of the four transitions is displayed in black.

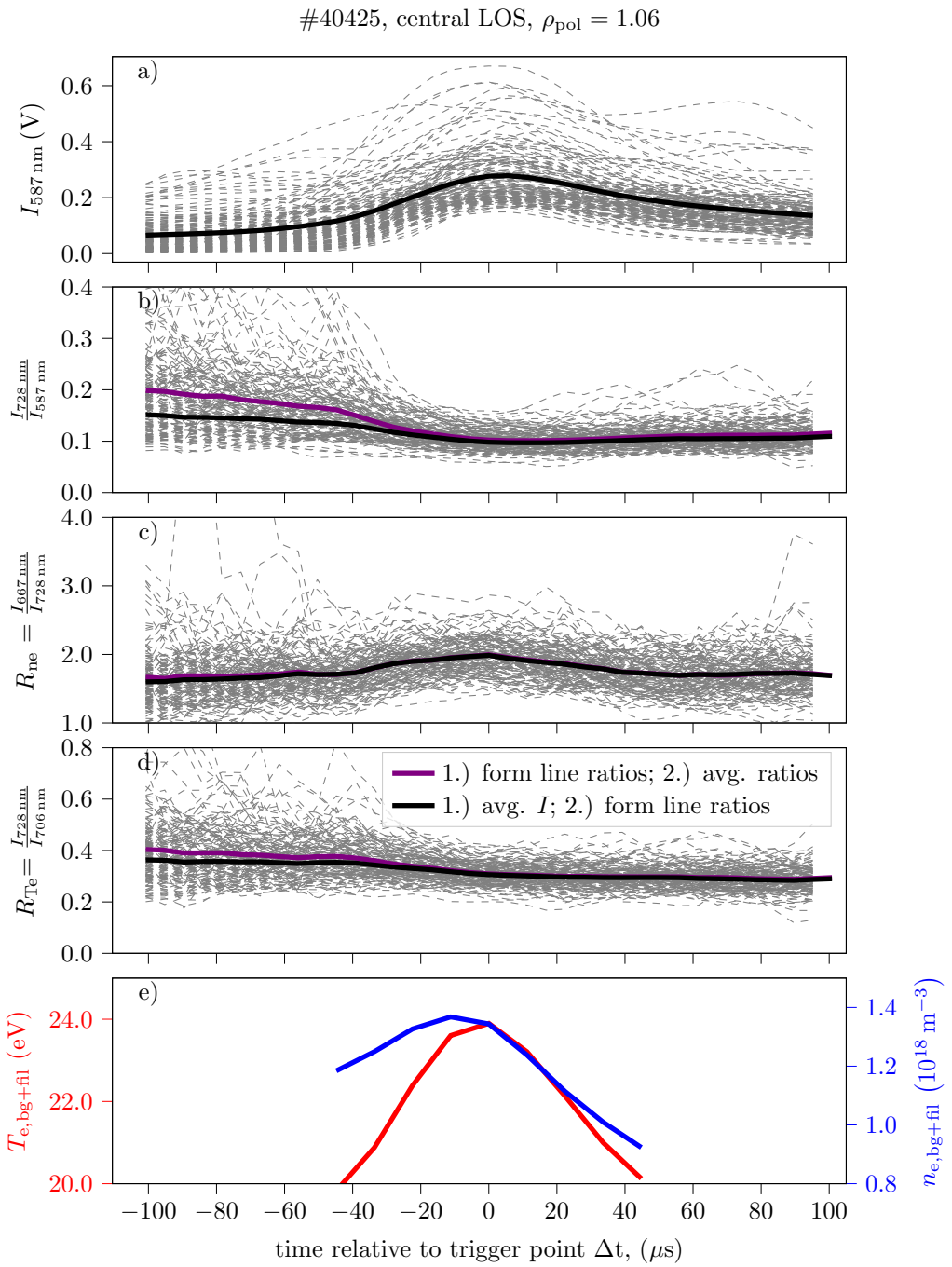

Figure 6.4.: The figure shows the four quantities used in the filament reconstruction, including the 587 nm line and three line ratios. For the line ratios, the order of averaging and forming the ratio can be swapped, what is compared with the two solid lines in the three lower panels. In the bottom panel, the temperature and density time trace at the fixed LOS position, calculated from the black CA line, are displayed.

6.2. Filament reconstruction from conditionally averaged experimental data

After processing the measured intensities by the previously described steps, the CA line ratios and the 587 nm intensity are fed into the reconstruction algorithm (see Section 5.1). The reconstruction is performed at $\Delta t = 0\,\mu s$. The corresponding 2D intensity perturbation for the 667 nm line is displayed in figure 6.5, created by linear interpolating the LOS intensities. In the intensity map, the filament has an elliptical shape. As shown in section 4.5, this does not automatically mean that the T_e and n_e distribution is elliptical since a round filament can also cause an elliptical intensity perturbation.

Using the conditionally averaged intensity and line ratios, the reconstruction is performed. The obtained results fromm the reconstruction are shown in Table 6.1.

Table 6.1.: Results of the filament reconstruction applied to CA data, evaluated at $\Delta t = 0\,\mu s$. The background values are $T_{e,bg} = 14.9\,eV$ and $n_{e,bg} = 1.5 \cdot 10^{18}\,m^{-3}$.

$T_{e,fil,0}$	=	$(13 \pm 7)\,eV$
$n_{e,fil,0}$	=	$(1.1 \pm 0.3) \cdot 10^{18}\,m^{-3}$
σ_{fil}	=	$(0.9 \pm 0.1)\,cm$
$z_{bco,fil}$	=	$(9.1 \pm 0.2)\,cm$
$y_{bco,fil}$	=	$(0.07 \pm 0.24)\,cm$
$width_{fil,FWHM}$	=	$2.37\,cm$
R_{fil}	=	$2.10\,m$
z_{fil}	=	$-0.135\,m$

The relative temperature and density amplitudes are $\frac{T_{e,fil}}{T_{e,bg}} = 84\,\%$ and $\frac{n_{e,fil}}{n_{e,bg}} = 73\,\%$. Both relative perturbations are in the same range, which is different to results from Langmuir probe measurements at other experiments and other conditions. For the Langmuir probe measurements, the relative temperature perturbation was up to a factor of four smaller than the density one (see section 2.6).

The filament has a FWHM size of 2.37 cm, which is roughly the size of the 5×5 grid. This can be seen in Figure 6.5, where the black circle shows the FWHM of the filament density. Besides this, the density perturbations radial center is shifted compared to the maxomum of the intensity perturbation. An analog observation was made for the synthetic filaments in section 4.2. The intensity perturbation is radially further outside, which on the LFS corresponds to a larger radius R.

Optimizing the cost function leads to a stable minimum, showing that the five

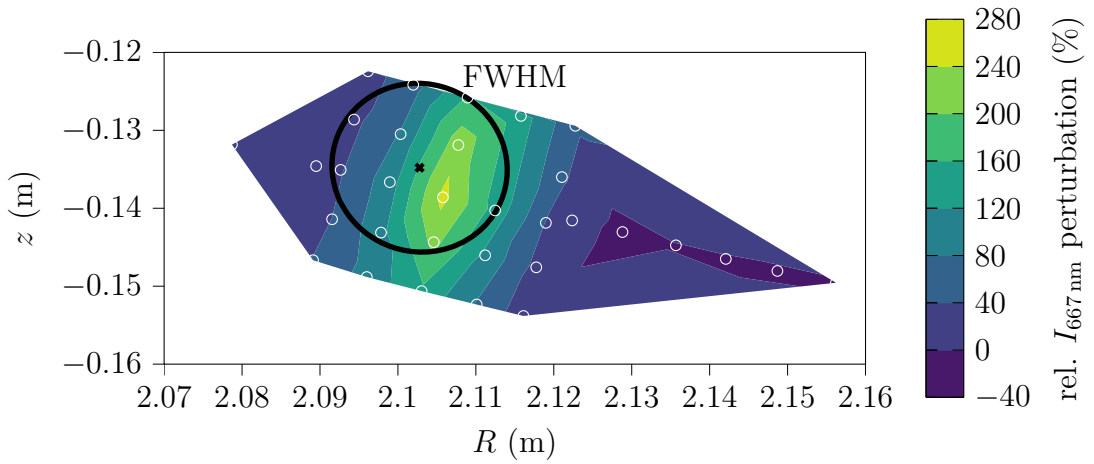

Figure 6.5.: The figure shows the relative $I_{667\,\mathrm{nm}}$ perturbation of the conditionally averaged filament at $\Delta t = 0\,\mu\mathrm{s}$. The white circles correspond to the LOS positions. The black circle shows the FWHM of the reconstructed density perturbation, with the cross indicating the center.

filament parameters (see Eq. 4.1) are enough to reconstruct the properties of an experimental filament.

In the same way, the reconstruction at $\Delta t = 0$ was performed, other CA time points $\Delta t \neq 0$ can be analyzed. This provides time traces of various filament properties. The analysis is done using the identical conditional averaged signal and moving forward and backward in the trigger time Δt. In total, a series of five time points from $-22.4\,\mu\mathrm{s}$ to $22.4\,\mu\mathrm{s}$ is analyzed. The corresponding intensity perturbations are displayed in figure 6.6. The 667 nm perturbation shows a filament moving radially outwards, with a very weak poloidal component.

The reconstructed filament properties are displayed in Figure 6.7. For the filament properties it is important to mention that they are displayed in the co-moving frame of the filament. This means, that the values at each time point are taken from the center of the filament. This is different to visualizations of probe measurements, as in Figure 2.5, that show the filament values at a fixed probe position. For comparison reasons, the time trace at a fixed LOS position is displayed for the temperature and density in Figure 6.4.

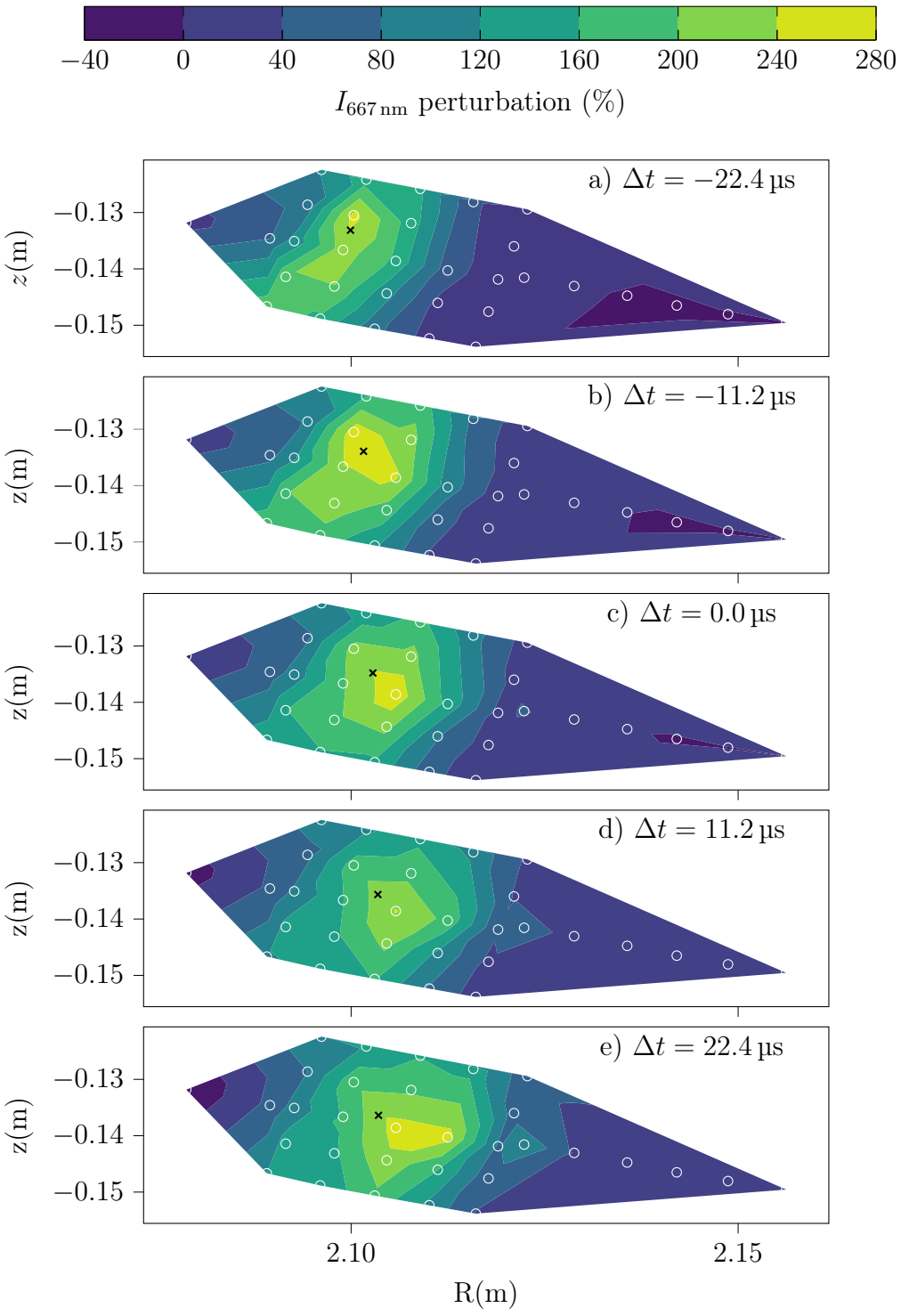

Figure 6.6.: Time trace of the 667 nm intensity perturbation from the conditionally averaged signal ($2.5\sigma - 10\sigma$). The white circles indicate the LOS positions, the black cross indicates the reconstructed position (R_{fil}, z_{fil}).

A cross in Figure 6.7 indicates the reconstructed filament position at the respective time point, while the color shows the intensity perturbation. As for the reconstructed time point and the synthetic filaments, the reconstructed filament position is on most time points radially inside the maximum of the intensity perturbation. In Figure 6.7a, the total temperature and density, consisting of filament amplitude and background, are displayed. Both quantities decay over time. The decay consists of two parts. On the one side, the radial outwards propagation of the filaments lowers the background values. On the other side, the filament amplitude decreases, which can be seen in Figure 6.7b. For the total temperature and density decay, a linear regression is performed. It leads to decay rates of $\frac{dT_e}{dt} = 0.10\,\mathrm{eV\,\mu s^{-1}}$ and $\frac{dn_e}{dt} = 1.3 \cdot 10^{16}\,\mathrm{m^{-3}\,\mu s^{-1}}$. In Section 6.3, these temperature and density decay rates are compared against different theoretical models.

In Figure 6.7c, the evolution of the reconstructed FWHM is displayed. The conditional averaging, used to process the data, is expected to influence the size evolution. Individual filaments, used for the averaging have a broad velocity distribution (as showed by Ref. [40] in figure 6 for different scenarios and positions, and in Figure 6.15 in this work). At the trigger points, all filaments are roughly at the same position. Due to the velocity distribution, faster filaments are expected to travel further than slower ones, so the filament distribution loses spatial coherence with increasing temporal distance to the trigger point. As a result, a parabolic curve is expected from the reconstruction of the conditional averaged signal, overlaying with the underlying physical behavior of the individual filaments. This parabolic curve can be seen in Figure 6.7c, with a minimum at $-11.2\,\mu s$ and not at $\Delta t = 0$, but the deviation is still within the errorbars. Since the individual filaments used for CA disperse over a longer time interval, it is expected that the CA influence will affect the temperature and density reconstruction in addition to the size. To prevent this, the time interval is not extended further to limit the size change in the interval to 16 %.

Another quantity influenced by this effect is the reconstructed position. In Figure 6.7d, it can be seen that the radial propagation velocity decreases over time. This goes along with a simultaneous increase in the reconstructed filament size.

After reconstructing the experimental time trace, the decay rates are compared in the next section to theoretical models.

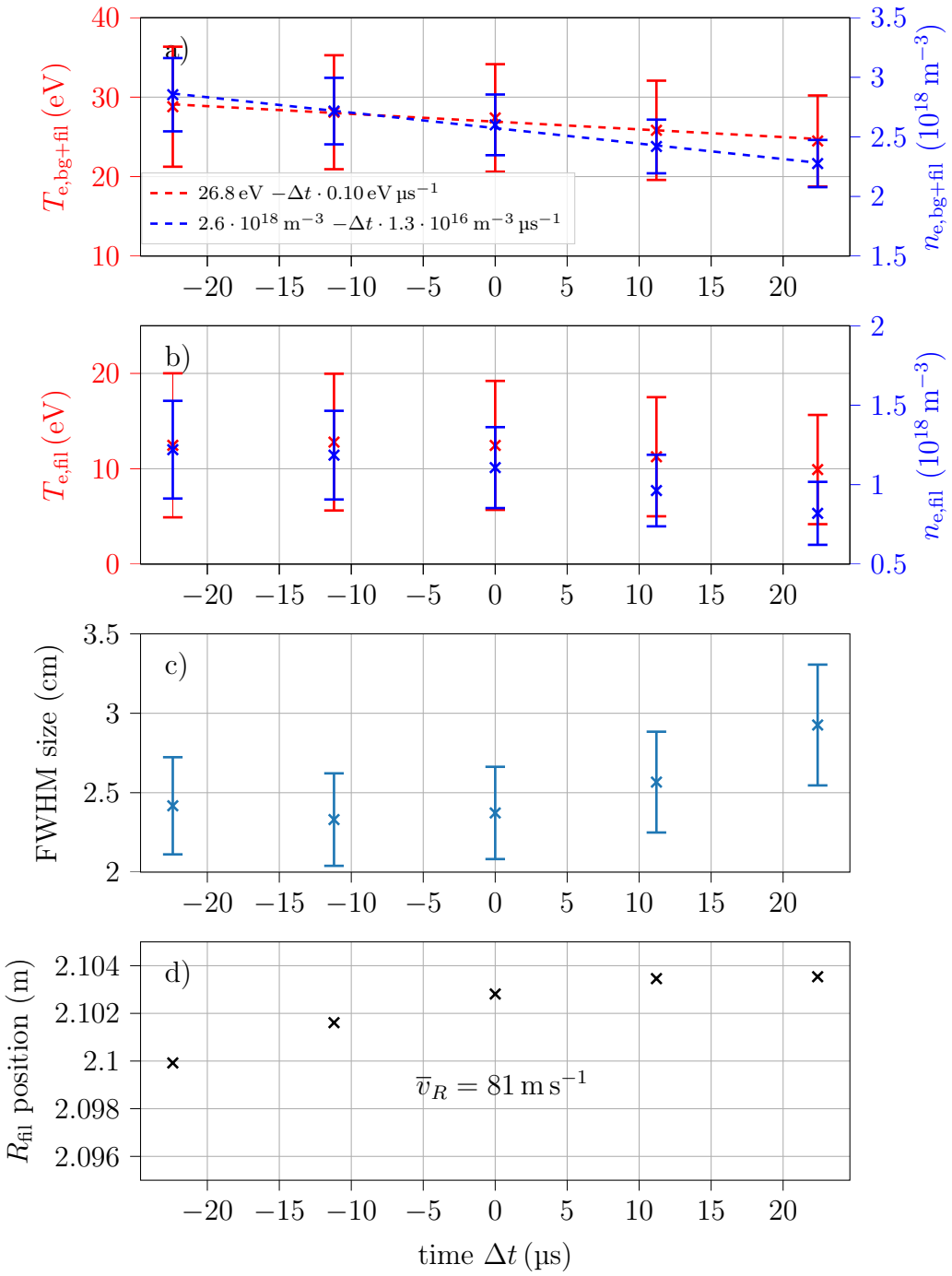

Figure 6.7.: The figure shows the reconstructed filament properties (of filaments between 2.5σ and 10σ) in panels b)-d). All properties are in the co-moving frame, showing the properties at the center of the filament. In panel a), the background and filament amplitude sum are displayed for temperature and density. A linear regression is applied to the total temperature and density data (dashed line).

6.3. Comparison of decay rates with analytical transport models

6.3.1. Analytical decay rate models

In decay rate models, the filament is assumed as a tube, with a cross-section A and the length equalling the connection length L_c. So, the volume of the filament is given as

$$V_\mathrm{fil} = L_\mathrm{c} \cdot A.$$

The density is assumed to decay due to parallel convective particle flux

$$\Gamma = n_\mathrm{e} \cdot c_\mathrm{s},$$

which leads to the following decay rate:

$$\frac{dn_\mathrm{e}}{dt} = \frac{-\Gamma \cdot A}{A \cdot L_c \cdot} = \frac{-n_\mathrm{e} \cdot c_\mathrm{s}}{L_c}. \tag{6.1}$$

The decay rate only depends on the connection length and the ion sound speed $c_\mathrm{s} = \sqrt{\frac{T_\mathrm{e}+\gamma T_\mathrm{i}}{m_\mathrm{i}}}$, with an adiabatic coefficient $\gamma = 3$ for the 1D case parallel to the magnetic field.

For the temperature, the decay is assumed to be due to parallel heat flux. The model starts with the filament energy

$$W_\mathrm{fil} = A \cdot L_c \cdot n_\mathrm{e} \cdot T_\mathrm{e}.$$

The only temporal varying parameters are n_e and T_e. To calculate the temperature decay, transport without sources and sinks, including $\frac{dn_\mathrm{e}}{dt} = 0$, is assumed. This leads to

$$\frac{dT_\mathrm{e}}{dt} = \frac{\frac{dW_\mathrm{fil}}{dt}}{A \cdot L_c \cdot n_\mathrm{e}} = \frac{-Q}{A \cdot L_c \cdot n_\mathrm{e}} = \frac{-q_\parallel}{L_c \cdot n_\mathrm{e}}. \tag{6.2}$$

For the parallel heat flux $q_\parallel$, the conductive heat flux $q_\parallel^\mathrm{cond.}$ (see eq. 2.2) or the convective heat flux $q_\parallel^\mathrm{conv.}$ (see eq. 2.4) is used.

A possible mechanism influencing the temperature decay is the electron-ion heat exchange [42]. In the SOL, the ion temperature is usually up to a factor of three higher than the electron temperature [165, 166]. Accordingly, ions, whose temperature can not be measured by the THB, can heat the electrons over collisions. Including this into the temperature decay gives the following equation:

$$\frac{dT_\mathrm{e}}{dt} = \frac{-q_\parallel}{L_c \cdot n_\mathrm{e}} + \frac{T_\mathrm{i} - T_\mathrm{e}}{\tau_\mathrm{ei}}. \tag{6.3}$$

Here T_i is the ion temperature and τ_ei is the energy relaxation time [42].

6.3.2. Comparison of measured and modeled decay rates

The evaluation performed in Section 6.2 is divided into multiple intensity sub-intervals, to compare them with the analytical decay rates. This is done to preserve the good SNR ratio while investigating decay rates for filaments with different amplitudes and, therefore, filaments with different strong perturbations of the 667 nm intensity. The entire intensity range from 2.5σ to 10σ is split into three intensity amplitude ranges with different values for the filament threshold and with comparable filament numbers. The sub-intervals are defined as

- $2.5 - 3\sigma$ (54 filaments),
- $3 - 4.5\sigma$ (74 filaments),
- $4.5 - 10\sigma$ (51 filaments) and
- $> 10\sigma$ (11 filaments).

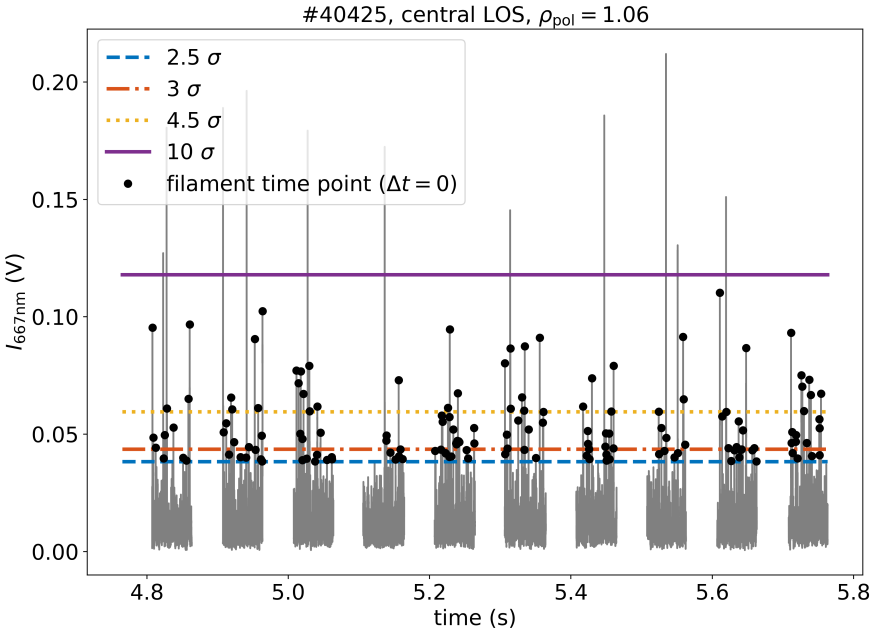

Figure 6.8.: The figure shows the 667 nm intensity time trace from the central LOS and the evaluated time interval. Depending on the intensity, filaments are grouped into different amplitude ranges, given as multiples the standard deviation (σ). The helium puffing is modulated with a frequency of 10 Hz, and the beam-off time points are discarded.

The corresponding intensity intervals are displayed in Figure 6.8. The reconstruction is performed for five consecutive time points in these intensity intervals. This leads to the temperature and density curves in Figure 6.9 and 6.10. A linear regression is performed for each temperature and density trace, the respective values are written in Table 6.2 and 6.3.

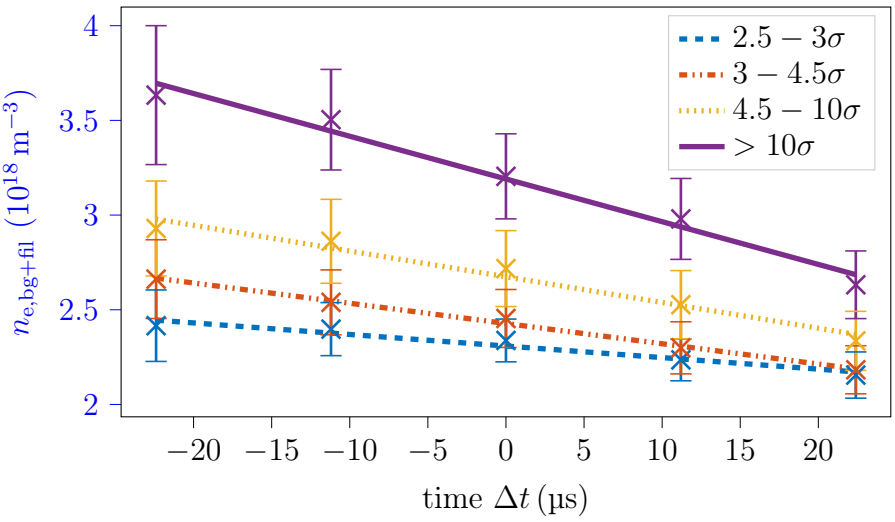

Figure 6.9.: Filament density in the co-moving frame for multiple intensity resolved amplitude ranges of the 667 nm line. Through each time trace, linear regression is performed; its values can be found in table 6.2.

First, the decay rates of the three amplitude ranges are compared against the combined decay rate of the entire $2.5 - 10\sigma$ interval. For the temperature, the decay rate ($-0.10\,\mathrm{eV\,\mu s^{-1}}$) and total filament electron temperature (26.8 eV) of the entire interval agree surprisingly well with the mean decay rates ($-0.10\,\mathrm{eV\,\mu s^{-1}}$) and mean total temperature (26.7 eV) of the three amplitude ranges ($2.5 - 3\sigma$, $3 - 4.5\sigma$, $4.5 - 10\sigma$). For the density, the offset of the three amplitude ranges, the result of $2.5 \cdot 10^{18}\,\mathrm{m^{-3}}$ is marginally lower than the offset from the entire range ($2.6 \cdot 10^{18}\,\mathrm{m^{-3}}$). The mean decay rate of the 3 amplitude ranges of $-1.3 \cdot 10^{16}\,\mathrm{m^{-3}\,\mu s^{-1}}$ is within the error bars equal to the decay rate of the intensity perturbation range from 2.5σ to 10σ. Besides this, the decay rates are compared to the decay rate models from subsection 6.3.1.

Density decay

The density decay is given by eq. 6.1, depending on the connection length, the ion sound speed, and the density offset $n_{e,bg+fil}^{\Delta t=0}$. The connection length L_c is half the distance between the inner and outer target, being 32 m. A Figure showing L_c is

Table 6.2.: This table compares the slopes of the linear regressions of n_e decay in the co-moving frame of the filament, from Figure 6.9, with the decay rates predicted by different models.

$I_{667\,\mathrm{nm}}$ amplitude	measurement		convection model
	$n_e(\Delta t = 0)$ $\left(10^{18}\,\frac{1}{\mathrm{m}^3}\right)$	$\frac{dn_e}{dt}$ $\left(10^{16}\,\frac{1}{\mathrm{m}^3\,\mu\mathrm{s}}\right)$	$\frac{dn_e}{dt}$ $\left(10^{16}\,\frac{1}{\mathrm{m}^3\,\mu\mathrm{s}}\right)$
$2.5\sigma - 3\sigma$	2.31 ± 0.01	-0.66 ± 0.08	-1.2
$3\sigma - 4.5\sigma$	2.43 ± 0.01	-1.1 ± 0.1	-1.2
$4.5\sigma - 10\sigma$	2.68 ± 0.02	-1.4 ± 0.1	-1.4
$> 10\sigma$	3.20 ± 0.03	-2.4 ± 0.2	-2.0

displayed in appendix A.3. For the ion sound velocity, the ion/electron temperature ratio is assumed to be $\tau_i = \frac{T_i}{T_{e,\mathrm{bg+fil}}} = 3$, which is supported by results from AUG [166] and other tokamaks [165]. The comparison between the experimental decay rate and the model is displayed in Table 6.2. Convective transport captures the density decay and agrees within error with the measured decay rates of the $3 - 4.5\sigma$ and $4.5 - 10\sigma$ amplitude ranges, with a slightly too large decay for the smallest filaments and a too weak decay for the largest filaments.

Temperature decay

Table 6.3.: This table compares the slopes of the linear regressions of T_e decay in the co-moving frame of the filament, from Figure 6.10, with the decay rates predicted by different models.

$I_{667\,\mathrm{nm}}$ amplitude	measurement		conduction model	sheath limited model
	$T_e(\Delta t = 0)$ (eV)	$\frac{dT_e}{dt}$ $\left(\frac{\mathrm{eV}}{\mu\mathrm{s}}\right)$	$\frac{dT_e}{dt}$ $\left(\frac{\mathrm{eV}}{\mu\mathrm{s}}\right)$	$\frac{dT_e}{dt}$ $\left(\frac{\mathrm{eV}}{\mu\mathrm{s}}\right)$
$2.5\sigma - 3\sigma$	25.9 ± 0.6	-0.05 ± 0.04	-0.09	-0.23
$3\sigma - 4.5\sigma$	25.8 ± 0.2	-0.09 ± 0.01	-0.09	-0.23
$4.5\sigma - 10\sigma$	28.5 ± 0.4	-0.09 ± 0.03	-0.11	-0.27
$> 10\sigma$	38.5 ± 0.5	-0.18 ± 0.03	-0.26	-0.41

For the temperature decay, given by eq. 6.2, two different heat fluxes can cause the cooldown. These is either the conductive heat flux (see eq. 2.2) or the convective heat flux (see eq. 2.4). The parallel conduction model best captures the

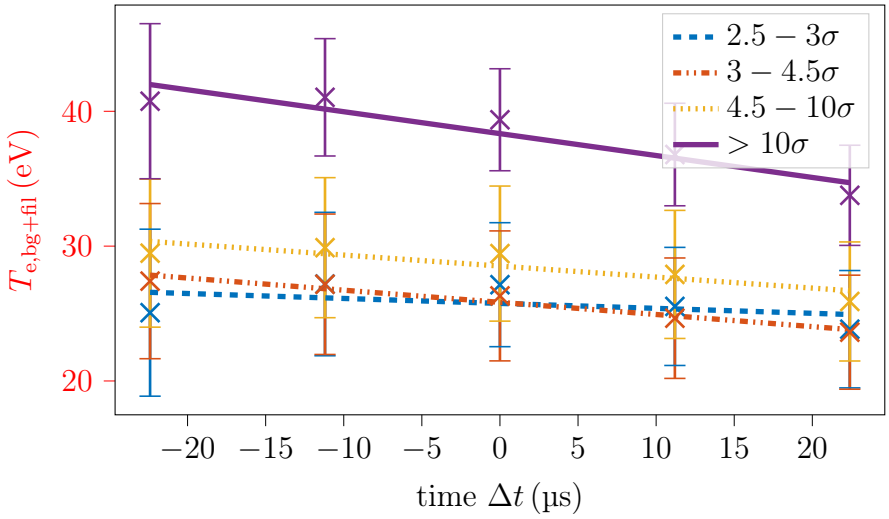

Figure 6.10.: Filament temperature in the co-moving frame for multiple intensity resolved amplitude ranges of the 667 nm line. Through each time trace, linear regression is performed; its values can be found in table 6.3.

experimental temperature decay. The model agrees within the error bars with the decay rates of the three lowest sigma intervals. For filaments $> 10\sigma$, the difference between the measured decay rate and conduction model is larger than the error bars. A possible mechanism for this difference could be the electron-ion heat exchange, incorporated in equation 6.3. Assuming $\tau_i = 3$ in the $> 10\sigma$ case, the conduction model with ion heating leads to a decay rate of $\frac{dT_e}{dt} = -0.23\,\mathrm{eV\,\mu s^{-1}}$. In comparison to the model without ion heating, the cooling rate of the electrons increases only by $+0.03\,\mathrm{eV\,\mu s^{-1}}$. Since ion heating makes a difference equal to the measurement uncertainties, no clear statement can be made about the influence of electron-ion heat exchange.

Although the difference for the temperature decrease by warm ions is not as significant and, therefore, not unique, the density decay supports the assumption that $\tau_i = 3$. For the density decay, τ_i affects the sound speed, which would be too small if cold ions would be assumed. Another indication that warm ions need to be considered, is the relative temperature and density decay. For models assuming cold ions, the density decays relatively slower than the temperature [167]. In the measured intensity intervals, the relative temperature decay rates are between $\frac{1}{T_e}\frac{dT_e}{dt}$ $=0.2\,\%\,\mathrm{\mu s^{-1}}$ and $0.5\,\%\,\mathrm{\mu s^{-1}}$, while the relative density decay rates are between $\frac{1}{n_e}\frac{dn_e}{dt}$ $=0.2\,\%\,\mathrm{\mu s^{-1}}$ and $0.75\,\%\,\mathrm{\mu s^{-1}}$. Accordingly, the relative temperature and density decay are of the same order of magnitude. The contradiction with the cold ion model, which predicts a higher relative temperature than density decay,

also indicates that warm ions must be taken into account.

In summary, comparing the measured and modeled decay rates, the temperature decay is best described by conductive transport for the given discharge. In contrast, the density decay can be approximately described by convective transport. Both models have assumed $\tau_\mathrm{i} = 3$, which supports that warm ion models best explain filament properties and dynamics [83, 99].

6.3.3. Heat fluxes due to filaments

Based on the measured quantities and the decay rate model comparison in the previous sections, the filamentary heat fluxes can be estimated. As there are no direct measurements of the ion properties, this comparison only includes the heat flux carried by the electrons. For the evaluation, the time point $\Delta t = 0$ is chosen. It is important to mention, that most of the parameters used in this calculation change over time, and therefore also the heat flow. For the heat flow parallel to the magnetic field, the conductive heat flux, as described by Equation 2.2 is used. Perpendicular to the magnetic field, the convective heat flux reads as

$$q_\perp^\mathrm{fil} = \frac{5}{2} T_\mathrm{e,bg+fil} \cdot n_\mathrm{e,bg+fil} \cdot v_\mathrm{\perp,fil}, \tag{6.4}$$

analog to Equation 2.4. By using the values from Tables 6.2 and 6.3, the corresponding heat fluxes are calculated in Table 6.4. As the reconstructed velocity is influenced by the effects of CA (see Section 6.2), the mean of the intensity velocity from the corresponding filaments is used.

Table 6.4.: Electron heat fluxes of filaments parallel and perpendicular to the magnetic field. The heat fluxes are calculated for $\Delta t = 0$ and decay over time. The velocities are averaged from the intensity velocities of the individual filaments.

$I_{667\,\mathrm{nm}}$ amplitude	$T_\mathrm{e,bg+fil}$ (eV)	$n_\mathrm{e,bg+fil}$ ($10^{18}\,\mathrm{m}^{-3}$)	$v_\mathrm{\perp,fil}$ ($\mathrm{m\,s}^{-1}$)	$q_\parallel^\mathrm{fil}$ ($\mathrm{MW\,m}^{-2}$)	$q_\perp^\mathrm{fil}$ ($\mathrm{MW\,m}^{-2}$)
$2.5\sigma - 3\sigma$	25.9	2.31	209	1.6	0.005
$3\sigma - 4.5\sigma$	25.8	2.43	171	1.6	0.005
$4.5\sigma - 10\sigma$	28.5	2.68	170	2.2	0.006
$> 10\sigma$	38.5	3.20	455	6.3	0.024

It can be seen that the dominant heat flux of the filaments in this scenario is parallel to the magnetic field, with a three order smaller perpendicular component. To obtain the time-averaged heat load from filaments, the heat flux at

the filament time point must be multiplied by the packing fraction, which is the fraction of time points where filaments are present [168]. For the given case, the packing fraction, resulting from the product of the filament frequency $f_{\mathrm{fil}} = 290\,\mathrm{Hz}$ and the temporal filament width $\tau_{\mathrm{AC}} = 51\,\mu\mathrm{s}$, is 1.5 %. During the time points without filaments, heat is transported by the steady background fluxes. For the background temperature of $T_{\mathrm{e,bg}} = 14.9\,\mathrm{eV}$, the parallel conductive heat flux is $q_{\parallel} = 0.2\,\mathrm{MW\,m^{-2}}$.

The heat fluxes of the filament in the direction parallel and perpendicular to the magnetic field cannot be directly compared. In the divertor, a narrow angle between the magnetic field line and the target increases the deposition are, geometrically reducing the heat flux on the PFC by a factor in the order of $\frac{1}{\sin(2°)} \approx 29$. By this, the effective parallel heat flux on the target is only by a factor of 10 smaller than the perpendicular heat flux.

Besides calculating the heat flux of the filaments at a given time point, the temperature can be extrapolated from the given time interval. By linearly extrapolating the temperature decay, the temperature at the PFC can be estimated. The corresponding values are displayed in Table 6.5.

Table 6.5.: Temperature decay from the filament position towards the wall. The values are linearly extrapolated from the temperature decay rates, assuming a constant velocity. The velocity is calculated from the intensities of the corresponding filaments.

$I_{667\,\mathrm{nm}}$ amplitude	measured values at $\Delta t = 0$			extrapolated values at PFC	
	$T_{\mathrm{e,bg+fil}}$ (eV)	$\frac{dT_{\mathrm{e,bg+fil}}}{dt}$ ($\mathrm{eV\,\mu s^{-1}}$)	$v_{\perp,\mathrm{fil}}$ ($\mathrm{m\,s^{-1}}$)	Δt (µs)	$T_{\mathrm{e,bg+fil}}$ (eV)
$2.5\sigma - 3\sigma$	25.9	-0.05	209	431	4.4
$3\sigma - 4.5\sigma$	25.8	-0.09	171	526	(0)
$4.5\sigma - 10\sigma$	28.5	-0.09	170	529	(0)
$> 10\sigma$	38.5	-0.18	455	197	2.9

For the time difference, a propagation with constant velocity from the measurement location ($z_{\mathrm{bco}} = 9\,\mathrm{cm}$) to the PFC ($z_{\mathrm{bco}} = 0\,\mathrm{cm}$) is assumed. The comparison of the predicted filament temperatures at the wall shows that only the largest filaments would reach the wall with a finite temperature. The filament temperature of the 2.5σ-3σ filaments at the wall is mainly influenced by the low decay rate. This decay rate is below the value of the conduction model and has relatively high uncertainties, as seen in Table 6.3, so this outlier, with a finite wall temperature, of the 2.5σ-3σ amplitude range shouldn't be overrated. As mentioned above, all of the quantities used in this calculation ($T_{\mathrm{e,bg+fil}}$, L_{c}, $\frac{dT}{dt}$) are time-dependent. There-

fore, the decay rates, which are for the electron temperature and density inverse proportional to the connection length, would decrease with radial propagation. As a result, the real filament temperatures at the PFC would be higher than in this linear extrapolation.

6.4. Reconstruction of individual filaments

As discussed in Section 6.2, the conditoinal averaging can be used to determine filament parameters for a characteristic filament representing the ensemble of filaments used for the CA. However, the reconstruction algorithm also allows to estimate filament parameters of single filaments, albeit larger errorbars. This way, distributions of filament parameters are obtained. Due to the worse SNR ratio in comparison to CA, only 121 individual filaments from the measured intensity interval (2.5σ to 10σ) can be successfully reconstructed. The advantage of this approach is, that the individual filaments can be used to investigate correlations between different filament parameters and the influence of conditional averaging in the following.

6.4.1. Comparing individual filaments to the conditional averaged filament

The first comparison between the individual filament results and the previous conditional average measurement is performed.

The results for the temperature and density reconstruction of the individual filaments is displayed in Figure 6.11. As the filament is assumed as a perturbation on top of the background, the filament amplitude is added to the background in the graphs. For the temperature and density, histograms are added on the side of the corresponding axis. The mean temperature of the ensemble of individual filaments is $(28 \pm 5)\,\mathrm{eV}$, while the conditional averaging result is $(28 \pm 7)\,\mathrm{eV}$ (see Table 6.1). This surprising agreement also confirms the observation made for the different intensity intervals in Section 6.3, where the average of the different ranges of filament amplitudes in terms of σ intervals also matched the temperature result for the whole interval. A similar comparison is made for the density. Here, the mean of the individual filaments is $(1.9 \pm 0.6) \cdot 10^{18}\,\mathrm{m}^{-3}$, while the conditional average resulted in a higher density of $n_{\mathrm{e,bg+fil}} = (2.6 \pm 0.3) \cdot 10^{18}\,\mathrm{m}^{-3}$ (see Table 6.1). The difference is due to the background density, which changes greatly for small differences in position due to the steep gradients. This density background is steeper compared to the temperature background, which is displayed in Figure 6.1. The density perturbation in the individual fiament and CA case, which is added to the background density, is similar in both cases. For the individual filaments,

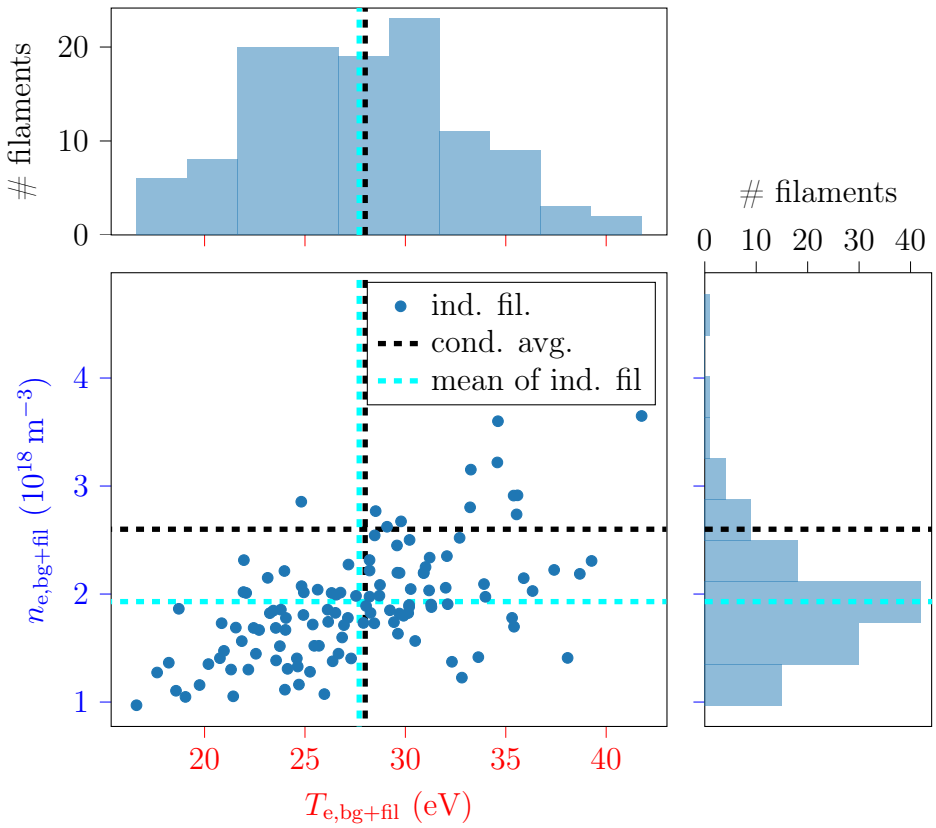

Figure 6.11.: Temperature and density of the individual filaments. For comparison, the result of the conditional averaging is displayed by the dashed horizontal and vertical lines. On the top/ side axis, the histograms for the individual filament parameters are displayed.

the mean density amplitude $n_{e,fil} = (1.5 \pm 0.5) \cdot 10^{18}\,\mathrm{m}^{-3}$ is in the same range as the amplitude of the conditional averaged filament of $(1.1 \pm 0.3) \cdot 10^{18}\,\mathrm{m}^{-3}$. The correlation between the total density and the position is further investigated in Section 6.4.2.

Further comparisons are made for the size of the individual filaments. Their comparison with the total density is shown in Figure 6.12. For the FWHM size, the mean of the single filaments is $(1.9 \pm 0.6)\,\mathrm{cm}$, which is lower than the conditional mean of $(2.4 \pm 0.2)\,\mathrm{cm}$, showing a difference in the range of the given errors (see table 6.1). As noted for the temporal evolution of filament size, conditional averaging combines filaments from different positions, whose intensity perturbation touches the trigger LOS. As these individual filaments can be located below or above the LOS, averaging over them results in a smeared mean. Therefore, the increased filament size for the conditional averaging is a data processing effect.

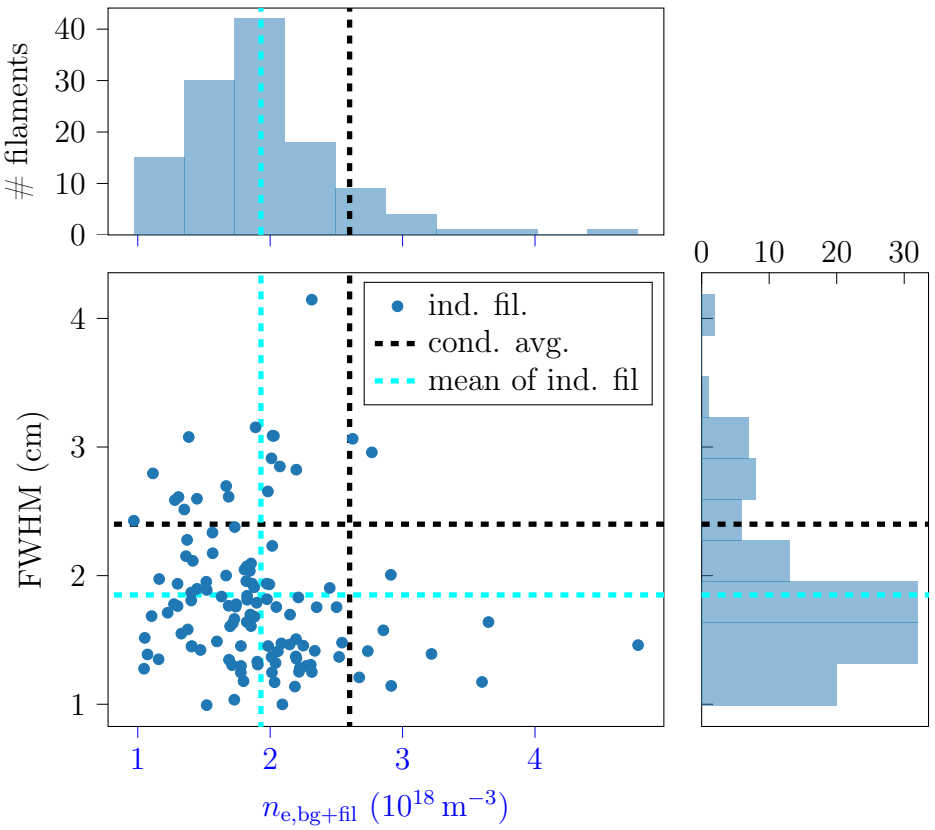

Figure 6.12.: Density and size of the individual filaments. For comparison, the result of the conditional averaging is displayed by the dashed horizontal and vertical lines. On the top/ side axis, the histograms for the individual filament parameters are displayed.

Filaments have a typical size of several ion gyro radii [85]. For the selected discharge and radial position, $\rho^* = 0.3\,\mathrm{cm}$. To compare this to the FWHM, corresponding to a diameter, the radius is doubled, resulting in $2\rho^* = 0.6\,\mathrm{cm}$. The experimentally measured FWHM would be two to five times ρ^*, confirming this rule of thumb. Furthermore, an analytical upper limit for the blob size is given as $10\rho^*$ [169], which is not exceeded by the measured filaments.

The comparison for the reconstructed filament positions is displayed in Figure 6.13. It shows, that $z_{\mathrm{bco,fil}}$, corresponding to the radial position, is reconstructed for most filaments in a narrow range. For the poloidal position $y_{\mathrm{bco,fil}}$, the reconstructed filament positions span the width from $-1\,\mathrm{cm}$ to $1\,\mathrm{cm}$, having an average value of $(-0.1 \pm 0.6)\,\mathrm{cm}$, which is within the uncertainties equal to the conditional averaged position of $(0.07 \pm 0.24)\,\mathrm{cm}$. The mean $z_{\mathrm{bco,fil}}$ position is for the individual filaments $(9.0 \pm 0.4)\,\mathrm{cm}$, compared to $(9.1 \pm 0.2)\,\mathrm{cm}$ for the conditional

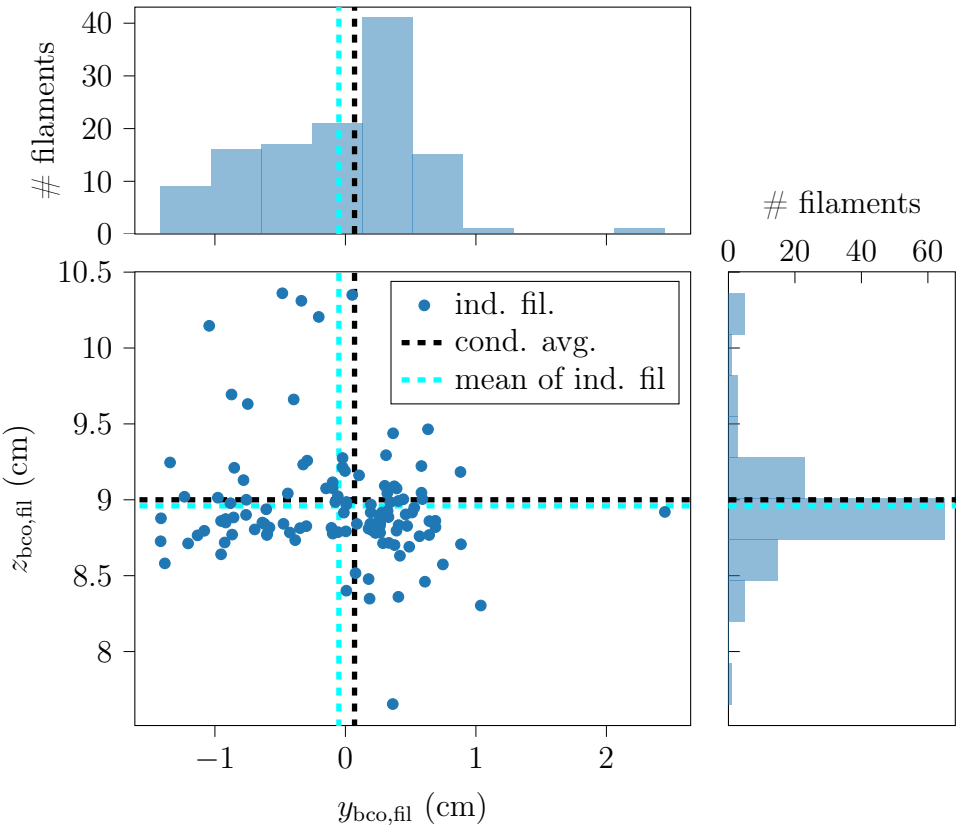

Figure 6.13.: Two-dimensional position of the individual filaments. For comparison, the result of the conditional averaging is displayed by the dashed horizontal and vertical lines. On the top/ side axis, the histograms for the individual filament parameters are displayed.

averaged filament. For both 2D coordinates, the mean of the individual filaments is within the uncertainties equal to the position of the conditional averaged filament.

Summarizing this comparison between the individual and conditional averaged filaments leads to the following points:

- The filament position is identical for the conditional averaged filament to the mean position of individual filaments.
- The CA size of the filaments is larger than that for individual filaments. This comes from averaging different filaments, sitting at different (poloidal) positions. Therefore the conditionally averaged filaments are larger than the individual filaments. As a consequence, the conditional averaged size shall not be overinterpreted, as the physical processes and the effect of the averaging can not be clearly separated.

- The conditional averaged temperature represents the individual filaments mean value. For the density, slight variations in the radial positions cause a difference in the background value, while the amplitude value is very close between the conditional averaged filaments and the mean value of the individual filaments.

6.4.2. Correlations between different filament parameters

In Figure 6.14, the five parameters of the reconstruction are displayed for the 121 individual filaments. As in the previous cases, the background values are added to the reconstructed amplitude for the temperature and density. The figure shows the histograms of the corresponding parameter on the diagonal axis and the different correlations in the graphs below. The Spearman correlation [170] is calculated for each plot. The Spearman correlation is a rank correlation, meaning it compares the position in the value-order distribution between two parameters. A correlation of 1 means that the order of values between two parameters is equal (100 % correlation), and -1 means that the order is inverted (100 % anti-correlation). A Spearman correlation of 0 means that the value orders are uncorrelated. The advantage of the Spearman correlation is that it is independent of the absolute amplitude value and, therefore, more outlier tolerant.

Most of the five filament parameters are uncorrelated. High correlation exist between the temperature and density of the filament. This indicates that the hot filaments are also denser, possibly pointing back to their origin at a radial position, where the pressure was higher than at the measurement position. Another high correlation is observed for the total density and the z_{bco} position. Filaments further radial inside, corresponding to a higher z_{bco} value, have a higher total density. This can be explained by the fact that the total density consists of a background and an amplitude. The background depends on the z_{bco} position, so the total density and the radial position are correlated. The relative perturbation amplitude is higher for the filament temperature, and the gradients for the temperature are flatter, which is the reason why no correlation between temperature and z_{bco} is observed (see Figure 6.1). The third strong correlation is observed between the z_{bco} position and the FWHM size of the filament. Filaments further radially inside are larger. This is caused by the point that all filaments are triggered at the identical LOS, and therefore, filaments further inside need to be larger to cause an intensity perturbation at the trigger LOS.

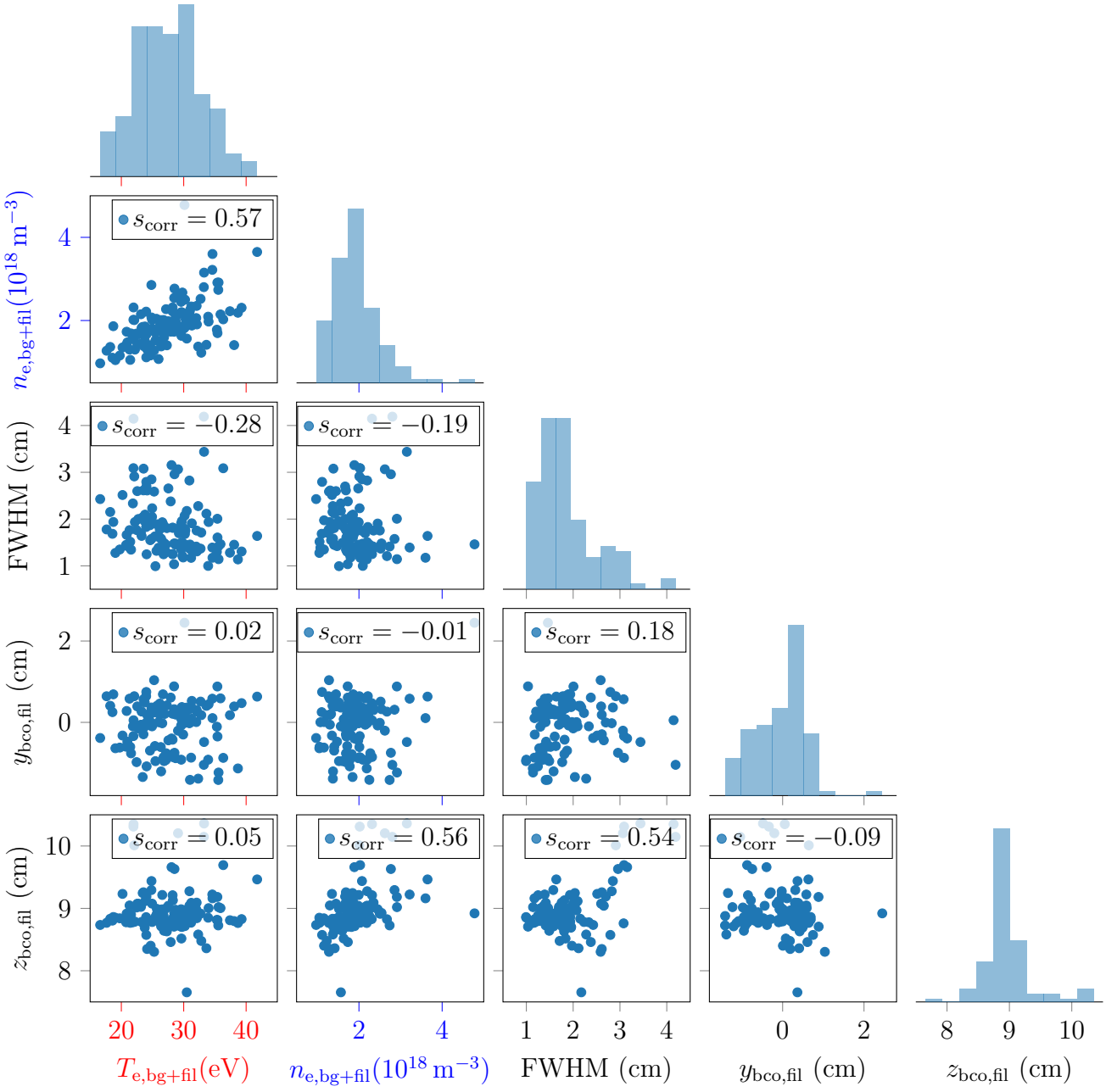

Figure 6.14.: Correlations between the five reconstructed quantities for the individual filaments. This are the total temperature and density, the FWHM size and the 2D position. The background value is added to the reconstructed amplitude for the temperature and density. The histograms for each quantity are displayed on the diagonal, and the Spearman correlation [170] is calculated for the correlation plots.

Besides correlating individual filament parameters among each other, they can be related to the measured intensity perturbation and the radial filament velocity, as calculated from the intensity. The corresponding pair plots are displayed in Figure 6.15. For comparison reasons, the intensity perturbation was normalized with the standard deviation (σ) of the intensity from the measurement interval. The radial velocity was calculated using the 667 nm intensity, and cross-correlating radial channels. In the last step, a linear regression was performed through the points of maximum correlation for each LOS to get the radial velocity. For individual filaments, the mean radial velocity is $183\,\mathrm{m\,s^{-1}}$, with only two filaments above $500\,\mathrm{m\,s^{-1}}$.

The correlation graphs show that the intensity of the filament is weakly correlated with the temperature and density. This is in contrast to synthetic filament scans from Section 4.3, which showed a dominant dependency of the intensity perturbation on the density amplitude of the filament. The correlation of intensity with temperature can be explained by the fact that temperature and density are correlated, and a correlation between temperature and intensity follows. This does not contradict the synthetic data results, where temperature and density scans were uncorrelated.

The radial velocity is uncorrelated to the filament density and very weakly correlated to the filament temperature. This is very interesting, as all filament scaling laws (see section 2.4) show that the radial velocity scales with the normalized filament pressure $\tilde{P}_\mathrm{e}$ and the sound speed c_s, which depends on the temperature.

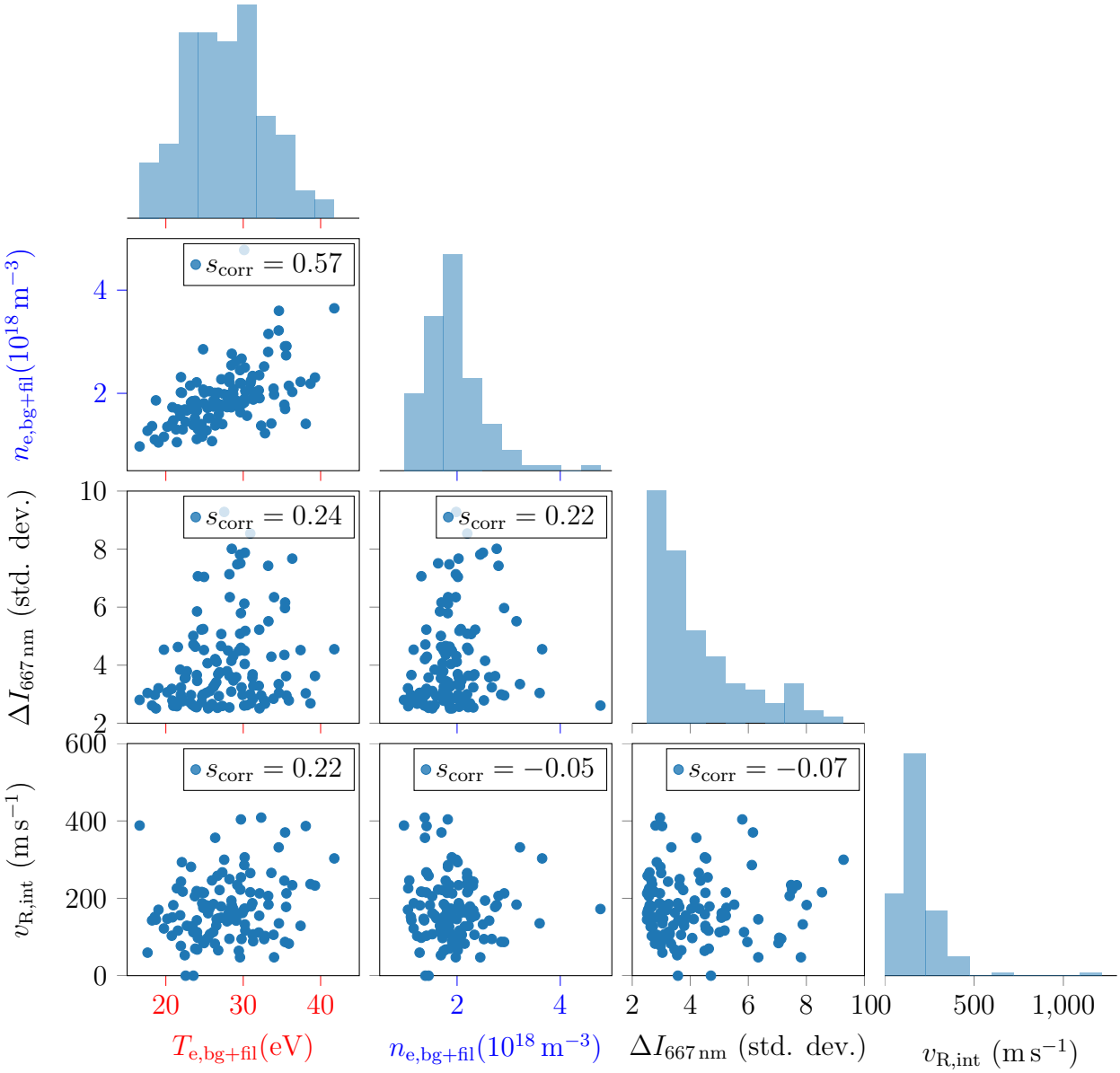

Figure 6.15.: Correlations between T_e and n_e with the amplitude of the intensity perturbation and the radial velocity. The background value is added to the reconstructed amplitude for the temperature and density. The histograms for each quantity are displayed on the diagonal, and the Spearman correlation [170] is calculated for the correlation plots.

6.4.3. Validating the experimental filter threshold for filament amplitudes

In this subsection, the individual filaments are used to validate the theoretical work on the filter criterion (2.5σ threshold) from Section 4.7 as a consistency check. For the selected discharge, a similar graph as Figure 4.13 together with the amplitudes of the individual filaments is shown in Figure 6.16.

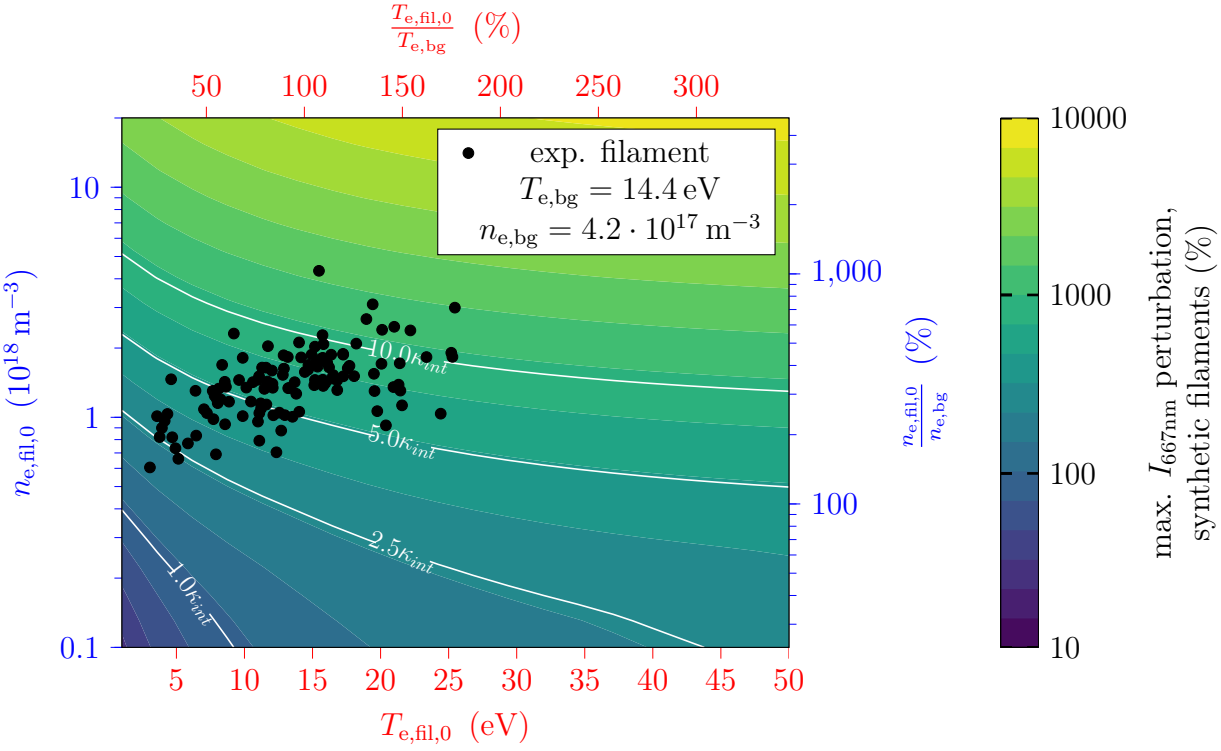

Figure 6.16.: The figure shows color coded the maximum intensity perturbation for synthetic filaments. Analogue to figure 4.13, contour lines of the normalized standard deviation κ_{int} are displayed. A filament above the $2.5\kappa_{int}$ line would result in an intensity perturbation above 2.5σ in the experiment. The experimentally reconstructed individual filaments (intensity range from 2.5σ to 10σ) are displayed as black dots for comparison. The synthetic filament has the following parameters: $z_{bco} = 9\,cm$ (exp. mean: $(9.0 \pm 0.4)\,cm$), $y_{bco} = 0\,cm$ (exp. mean: $(-0.1 \pm 0.6)\,cm$), $\sigma_{fil} = 0.8\,cm$ (exp. mean: $(0.8 \pm 0.3)\,cm$).

The synthetic filaments are placed on the identical background used for the experimental filament reconstruction. The mean values of the individual recon-

structed filaments are used for the filament size and position. The size for the synthetic filaments is $\sigma_{\mathrm{fil}} = 0.8\,\mathrm{cm}$, and the experimental mean is $\sigma_{\mathrm{fil}} = (0.8 \pm 0.3)\,\mathrm{cm}$. For the position, the filament is placed at $z_{\mathrm{bco}} = 9\,\mathrm{cm}$, $y_{\mathrm{bco}} = 0\,\mathrm{cm}$, with the experimental values beeing $z_{\mathrm{bco}} = (9.0 \pm 0.4)\,\mathrm{cm}$, $y_{\mathrm{bco}} = (-0.1 \pm 0.6)\,\mathrm{cm}$. Analog to Figure 4.13, multiples of the experimentally determined intensity fluctuation level κ_{int} are displayed, corresponding to the same value of σ in the experiment.

The individual filaments originate from the experimental reconstruction, selected by the intensity interval of 2.5σ to 10σ. Accordingly, individual filaments with their temperatures and densities are expected to be in the region between $2.5\kappa_{int}$ and $10\kappa_{int}$. This is for the majority of the filaments correct, with only 2 filaments below the $2.5\kappa_{int}$ line. Considering the mean uncertainty for the temperature and density reconstruction, $\pm 7.9\,\mathrm{eV}$ and $\pm 0.3 \cdot 10^{18}\,\mathrm{m}^{-3}$, into account, the gap between these outliers and the $2.5\kappa_{int}$ line is within the uncertainty of the reconstruction. The same is valid for most outliers above the $10\kappa_{int}$ line. Besides this, different filament positions and sizes influence the resulting intensity perturbation as well.

Despite the different assumptions made for the κ_{int} lines, they roughly represent the experimental range of filament amplitudes. All outliers are within acceptable limits considering the distribution of filament sizes and positions and the reconstruction uncertainties.

By comparing Figure 4.13 and Figure 6.16, corresponding to a near-SOL and far-SOL case, different characteristics are found. For both graphs, the intensity perturbation and the κ_{int} lines are horizontally spaced, with a slightly higher temperature dependency for the far-SOL case in Figure 6.16. For low T_{e}, the κ_{int} lines of both figures are at the same density amplitude. So despite the different background profiles, the filtered region of the filament amplitudes is still similar for both cases. This is important, as the relative intensity perturbation of the 667 nm line is up to a factor of 10 higher in the far-SOL case.

This comparison shows consistency between the synthetic filaments and the experimental measurements.

7. Summary and Outlook

Filaments are positive pressure perturbation structures aligned with the magnetic field. They appear in the scrape-off layer and cause convective transport due to their movement perpendicular to the magnetic field. This transport reduces the heat load on the divertor target and transfers heat and particles to other plasma-facing components. As a result, filaments are an essential transport mechanism for balancing the total power deposition on different regions in the plasma vessel. This power deposition is especially important for future fusion power plants, as they face the risk of too high power loads onto a small region of the target, impeding the plasma operation by melting and increased sputtering of these parts. Therefore, filamentary transport is an important tool to reduce these power loads. For an accurate understanding of this transport process, several filament properties must be measured. Of interest are the filament size, velocity, temperature, density, and frequency of occurrence. Due to the small size of the filaments in the poloidal cross-section combined with the high radial velocity, fast diagnostics are required. The thermal helium beam diagnostic at ASDEX Upgrade meets these criteria by measuring with a 5×5 grid of lines of sight in the scrape-off layer. For each line of sight, four helium transitions are measured simultaneously with a polychromator system. From these four intensities, the electron temperatures and densities are calculated using a collisional radiative model.

In the first part of this thesis, the interaction between the filament and the measured helium line emission intensities was studied. This is done by placing a synthetic filament in the scrape-off layer and calculating the resulting intensities using a collisional radiative model. For the amplitude of the filament intensity perturbation, it was found that the density is the parameter of highest impact. The temperature is relatively weakly correlated with the intensity perturbation. For the electron temperature and density, the relationship with the intensity perturbation is non-linear. In addition, the circular filament produces an elliptical intensity perturbation whose maximum perturbation position is shifted radially outwards with respect to the filament position. An investigation of the radial sensitivity to detect filaments showed that measurements in the far-scrape-off layer are preferred due to a good signal-to-noise ratio, and a higher relative perturbation amplitude in comparison to the near-scrape-off layer.

In the second part, the filament properties are reconstructed from the measured data. The reconstruction requires a dynamic collisional radiative model, since the

helium emission comes from an energy state population density that is not in collisional radiative equilibrium once the plasma density is low in the far-scrape-off layer where the measurements are performed. For the experimental reconstruction of filament size, position, electron temperature, and density, a discharge in the I-phase regime was chosen, as the discharge has superior conditions for a successful analysis. To improve the signal-to-noise ratio, the individual filaments are conditionally averaged, by combining the individual time traces of the filaments. For this measurement case, the relative temperature and density amplitude of the filament, compared to the filament-free background plasma are both on the order of 70 %, whereas individual filament measurements and previous electrical probe measurements have measured a significantly higher density than temperature perturbation. Sequential reconstruction of time points in the co-moving frame of the filament reveals a temporal decay of the filament temperature and density. The temperature decay can be explained by heat conduction along the magnetic field. For the density decay, the convective particle flux along the magnetic field explains the measured behavior.

Aside from the averaged filament, individual filaments can be reconstructed. Due to the challenging data quality with respect to the signal-to-noise ratio, this reconstruction is not successful for every measured filament. By comparing the successfully reconstructed filaments, different characteristics can be observed. The mean filament position is consistent with the mean of the individual filaments, while the conditionally averaged size is larger than the mean size of the individual filaments due to the effects of averaging and different velocities of individual filaments. While the mean of the temperature amplitude is consistent with conditional averaging, the mean of the density deviates due to strong background gradients, that cause for the different positions of the individual filaments strongly varying background values, which is not covered by the averaging. Besides this, the temperature and density of the individual filaments are correlated, but only the temperature is very weakly correlated with the radial filament velocity, which is expected from analytical scaling laws.

To investigate filamentary transport further, more discharges should be analyzed. This could lead to the following insights:

- *Correlation of filament properties with plasma edge parameters*: By studying more discharges, the correlation of the filament temperature, density, and size with plasma edge parameters can be studied, allowing for better delimiting of the radial range of filament creation.

- *Comparing filamentary heat flows in different scenarios*: By evaluating the filamentary heat flux and its relative share, the deposition on different components can be investigated. This microscopic picture could be compared to a global power distribution analysis [98].

- *Comparison of decay rates*: By performing the reconstruction of the temperature and density decay for different discharges, the decay rate models can be further validated, and the possible influence of ion-electron heat exchange can be studied.

To predict the filamentary transport of future fusion devices with higher accuracy, inter-machine validated knowledge, supported by comparisons with different simulation codes [171], is essential to strengthen the theoretical understanding and thus the predictive capability. Another important measurement is the ion fraction of the filament heat flux, which is larger than the electron fraction due to the higher ion temperatures in the scrape-off layer. Since the thermal helium beam diagnostic cannot determine ion temperatures, other diagnostics are needed to complete the picture of the filament heat flux.

A. Appendix

A.1. Drifts

In magnetized plasma, different drifts occur. according to [42], they are generally expressed as

$$\vec{v}_D = \frac{\vec{F} \times \vec{B}}{qB^2}.$$

The drift velocity is perpendicular to the force $\vec{F}$ as well as the magnetic field $\vec{B}$. Due to the charge dependence q, the drifts for electrons and ions are opposite for charge-independent forces.
Important drifts are the

- $\vec{E} \times \vec{B}$ drift

$$\vec{v}_D^{E\times B} = \frac{\vec{E} \times \vec{B}}{B^2}, \tag{A.1}$$

  which is caused by the electric field $\vec{E}$.

- Gradient drift

$$\vec{v}_D^{\nabla B} = \frac{-W_\perp}{q} \frac{\nabla_\perp B \times \vec{B}}{B^3}, \tag{A.2}$$

  which is caused by the inhomogeneous magnetic field B. The perpendicular energy is given as $W_\perp$.

- Diamagnetic drift

$$\vec{v}_D^{\text{dia}} = -\frac{\nabla p \times \vec{B}}{qB^2} \tag{A.3}$$

  caused by the pressure gradient ∇p, which has to be treated individually for electrons and ions.

A.2. Background profiles with and without filament timepoints

In Figure A.1, the background profiles for the selected interval used for the reconstruction (#40425, t =4.78 s to 5.78 s) are displayed. The background profiles are once calculated with and once without filament time points.

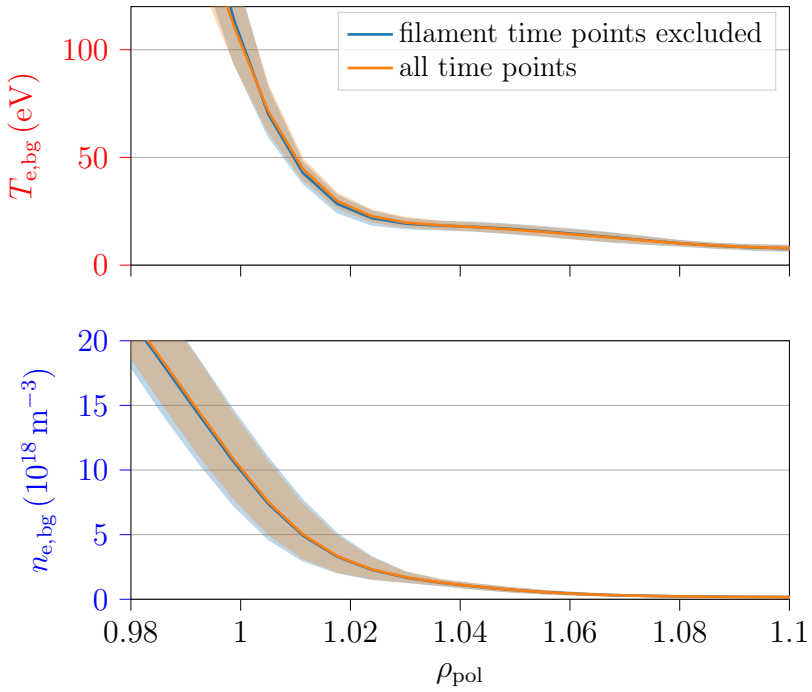

Figure A.1.: Comparison of the background profiles calculated with and without filament time points. They origin from # 40425,t =4.78 s to 5.78 s.

For the calculation without filaments, the entire time point is discarded if the intensity perturbation is on any LOS above the 2.5σ criterion (see section 6.1.3). In addition, the four neighboring time points (2 before, 2 after) for each filament time point are also discarded. Applying this criterion results in discarding 12 % of the time points.

Comparing the profiles with and without filament time points shows no significant difference for this evaluated interval. Nevertheless, the background without filament time points is used for the evaluation in Chapter 6.

A.3. Connection length profile

For discharge # 40425, at $t = 4.78\,\mathrm{s}$, the connection length L_c is calculated. As stated in section 2.1, we define the connection length as half the distance between the inner and outer target.

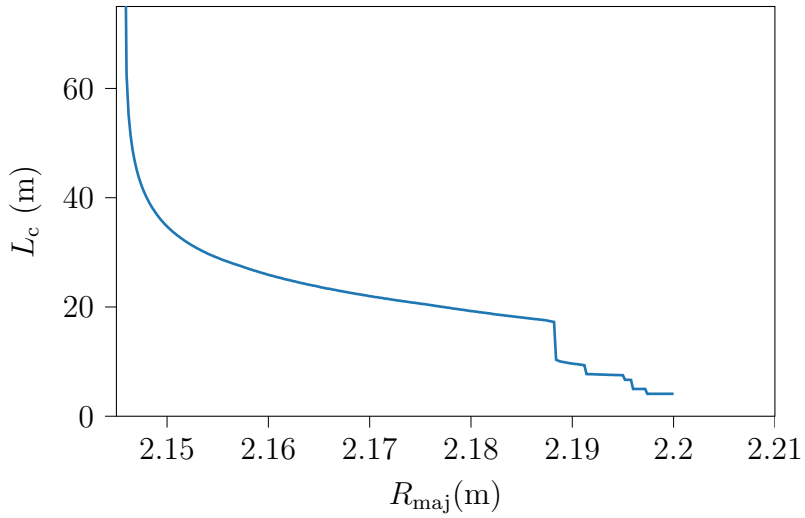

Figure A.2.: The connection length of # 40425, $t = 4.78\,\mathrm{s}$. The profile is plotted over the midplane radius R_maj. The step at $R_\mathrm{maj} = 2.185\,\mathrm{m}$ is caused by the field lines hitting a limiter. The secondary/upper X-point causes the divergence of the connection length towards $R_\mathrm{maj} = 2.14\,\mathrm{m}$.

Different features can be seen in the connection length profile. In the confined region, the field lines are closed, which would correspond to an infinite L_c. The field lines just outside the LCFS are close to the magnetic X-point, where the field line makes many toroidal turns and which significantly increases the length. Field lines further out are less affected by the X-point. Here, the shape of the vessel components dominantly determines the length of the magnetic field line. For the corresponding equilibrium, the connection length is plotted over the major axis, which is the R value of the tokamak at the height of the magnetic axis. For the corresponding profile, the effect of the secondary/upper X-point can be seen at $R_\mathrm{maj} = 2.14$. At $R_\mathrm{maj} = 2.185$ the field lines hit an auxiliary limiter which causes an abrupt shortening of L_c. Further steps are caused by additional in-vessel structures, limiting the field line length.

A.4. Intensity distribution of the trigger signal

In Figure A.3, the intensity distribution of the trigger signal, originating from the evaluated interval in Chapter 6 is displayed.

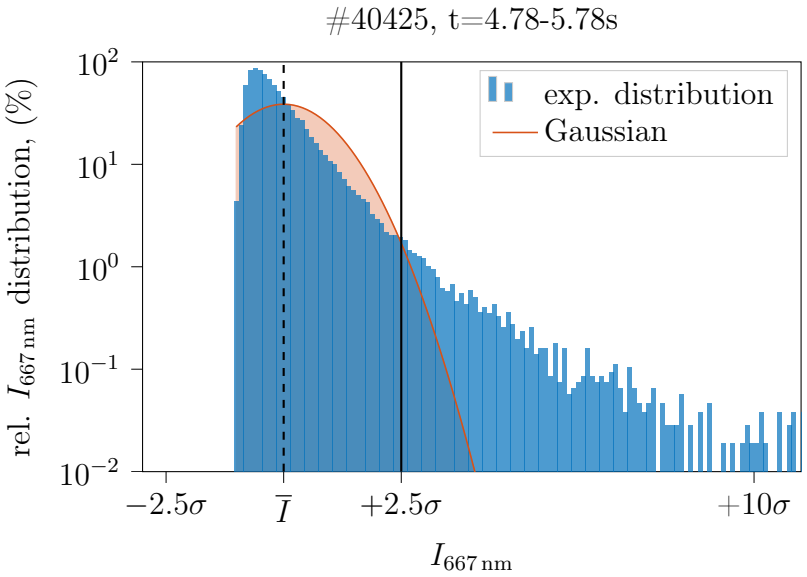

Figure A.3.: Intensity distribution of the time trace for the central LOS of the 5×5 grid, in a logarithmic representation. The dashed line represents the mean intensity, and the solid line is the mean plus 2.5 standard deviations. As the intensity is always positive, a cut restricts the intensity range below the mean. The kurtosis is 49 for the measured distribution, and the skewness is 4.9, while both values are zero for a Gaussian distribution.

A Gaussian curve is fitted to the measured signal. The slight mismatch shows that the signal of the plasma interval is not well described by random noise, which would cause a perfect Gaussian distribution. As described in subsection 6.1.3, the deviation is a result of the filamentary transport. For an intensity amplitude higher than the mean plus 2.5σ, the Gaussian curve decreases faster than the measured distribution. Therefore, the signals above 2.5σ are more likely to come from the filaments, which modify the random distribution, than from the Gaussian.

Abbreviations

AUG ASDEX Upgrade :
ASDEX Upgrade [34] is a medium-size tokamak and the successor of ASDEX(AxialSymmetrisches Divertor EXperiment). It is located in Garching. See subsection 1.2.2

bco beam coordinate system:
Coordinate system used in the extended CRM. See figure 3.5.

CA conditional averaging

CRE collisional radiative equilibrium:
Condition in an atomic system/CRM, where the relative state populations are constant and solely determined by the local parameters, typically the electron temperature and density.

CRM collisional radiative model
Used to describe the light emission caused by neutrals being injected into plasma. For the thermal helium beam diagnostic, the model is used to determine the electron temperature and density, see subsection 3.1.3.

DIII-D Doublet III-D:
DIII-D is a medium-size tokamak operated by General Atomics in San Diego.

ECE electron cyclotron emission

ECRH electron cyclotron resonance heating

ELM edge localized mode

FWHM Full Width at Half Maximum :
For a Gaussian distribution, it is given as FWHM $= 2\sqrt{2\ln 2}\sigma$.

GPI gas-puff imaging:
Diagnostic which uses a gas-puff to measure plasma turbulence by it's local increased light emission [88].

H-mode high-confinement mode

ICRH ion cyclotron resonance heating

IDA integrated data analysis

ITER	International Thermonuclear Experimental Reactor: ITER is the worldwide largest tokamak, currently under construction in Cardarache. The first plasma is foreseen for the end of the 2020s.
JET	Joint European Torus: JET is currently the largest operating tokamak, performing experiments since 1983, and is located in Culham.
LCFS	Last Closed Flux Surface: magnetic flux surface dividing the confined region and the SOL. In the divertor configuration, the LCFS is also called separatrix.
LFS	low field side
L-H transition	transition from L-mode to H-mode
LIB	Lithium beam diagnostic
LOS	line of sight
L-mode	low-confinement mode
MHD	magnetohydrodynamic: a fluid theory, used to describe plasmas [25].
NBI	neutral beam injection
n_e	electron density, in (m^{-3})
NIF	National Ignition Facility: The world's largest inertial fusion facility at the Lawrence-Livermore National Laboratory.
PEC	photon emissivity coefficient
PFC	plasma-facing components: all components in the vessel, getting in contact with the plasma
PFR	private flux region: region between the two divertor legs, containing no hot plasma
PRE	pedestal relaxation event
QCE	quasi-continuous exhaust regime

RFX-mod	Reversed Field eXperiment-mod
ρ_{pol}	the normalized poloidal magnetic flux coordinate
R_{ne}	density-sensitive line ratio: ratio from two helium transitions, given as $\frac{I_{667\,\mathrm{nm}}}{I_{728\,\mathrm{nm}}}$
R_{Te}	temperature-sensitive line ratio: ratio from two helium transitions, given as $\frac{I_{728\,\mathrm{nm}}}{I_{706\,\mathrm{nm}}}$
σ	standard deviation
SNR ratio	signal-to-noise ratio
SOL	scrape-off layer: Region between the confined region and the plasma vessel, characterized by open magnetic field lines. As the contact layer, it is important for the power exhaust. The physics in the SOL is further explained in section 2.1.
T_{e}	electron temperature, in (eV) 1 eV equals 11 605 K
TEXTOR	Tokamak Experiment for Technology Oriented Research: TEXTOR was a tokamak operating from 1983-2013 in Juelich.
THB	thermal helium beam diagnostic
UV	ultra violet
W7-X	Wendelstein 7-X: W7-X is a stellarator operated by the Max-Planck-Institut für Plasmaphysik and located in Greifswald.
WCM	weekly coherent mode
XPR	X-Point radiator

List of Figures

List of Tables

Bibliography

[1] K. Calvin, D. Dasgupta, G. Krinner *et al.*, *IPCC, 2023: Climate Change 2023: Synthesis Report. Contribution of Working Groups I, II and III to the Sixth Assessment Report of the Intergovernmental Panel on Climate Change [Core Writing Team, H. Lee and J. Romero (eds.)]. IPCC, Geneva, Switzerland.*, Technical report, Intergovernmental Panel on Climate Change (2023), doi:10.59327/IPCC/AR6-9789291691647, URL https://www.ipcc.ch/report/ar6/syr/

[2] International Energy Agency, Https://Www.Iea.Org/Reports/World-Energy-Outlook-2022/Executive-Summary page 524, URL https://www.iea.org/reports/world-energy-outlook-2022

[3] G. Audi and A. Wapstra, Nuclear Physics A **595** (1995) 409–480, ISSN 03759474, doi:10.1016/0375-9474(95)00445-9, URL https://linkinghub.elsevier.com/retrieve/pii/0375947495004459

[4] H.-S. Bosch and G. Hale, Nuclear Fusion **32** (1992) 611–631, ISSN 0029-5515, doi:10.1088/0029-5515/32/4/I07, URL https://iopscience.iop.org/article/10.1088/0029-5515/32/4/I07

[5] M. A. Abdou, in *Nuclear Data for Science and Technology*, pages 293–312, Springer Netherlands, Dordrecht (1983), ISBN 9027715602, doi:10.1007/978-94-009-7099-1_63, URL http://link.springer.com/10.1007/978-94-009-7099-1{_}63

[6] L. Giancarli, M. A. Abdou, D. Campbell *et al.*, Fusion Engineering and Design **87** (2012) 395–402, ISSN 09203796, doi:10.1016/j.fusengdes.2011.11.005, URL https://linkinghub.elsevier.com/retrieve/pii/S0920379611006090

[7] G. Gamow, Zeitschrift für Physik **51** (1928) 204–212, ISSN 1434-6001, doi:10.1007/BF01343196, URL http://link.springer.com/10.1007/BF01343196

[8] D. R. Morrison, Physics Letters A **185** (1994) 498–502, ISSN 03759601, doi:10.1016/0375-9601(94)91133-9, URL https://linkinghub.elsevier.com/retrieve/pii/0375960194911339

[9] H.-S. Bosch, G. Wurden, J. Gernhardt *et al.*, Journal of Fusion Energy **9** (1990) 165–186, ISSN 1572-9591, doi:10.1007/BF02627582, URL https://doi.org/10.1007/BF02627582

[10] J. D. Lawson, Proceedings of the Physical Society. Section B **70** (1957) 6–10, ISSN 0370-1301, doi:10.1088/0370-1301/70/1/303, URL https://iopscience.iop.org/article/10.1088/0370-1301/70/1/303

[11] E. M. Burbidge, G. R. Burbidge, W. A. Fowler *et al.*, Reviews of Modern Physics **29** (1957) 547–650, ISSN 0034-6861, doi:10.1103/RevModPhys.29.547, URL https://link.aps.org/doi/10.1103/RevModPhys.29.547

[12] H. A. Bethe, Physical Review **55** (1939) 434–456, ISSN 0031-899X, doi:10.1103/PhysRev.55.434, URL https://link.aps.org/doi/10.1103/PhysRev.55.434

[13] K. Miyamoto, *Plasma Physics for Controlled Fusion*, volume 92 of *Springer Series on Atomic, Optical, and Plasma Physics*, Springer Berlin Heidelberg, Berlin, Heidelberg (2016), ISBN 978-3-662-49780-7, doi:10.1007/978-3-662-49781-4, URL http://link.springer.com/10.1007/978-3-662-49781-4

[14] S. E. Wurzel and S. C. Hsu, Physics of Plasmas **29**, ISSN 1070-664X, doi:10.1063/5.0083990, 2105.10954, URL https://pubs.aip.org/pop/article/29/6/062103/2847827/Progress-toward-fusion-energy-breakeven-and-gain

[15] A. B. Zylstra, A. L. Kritcher, O. A. Hurricane *et al.*, Physical Review E **106** (2022) 025202, ISSN 2470-0045, doi:10.1103/PhysRevE.106.025202, URL https://link.aps.org/doi/10.1103/PhysRevE.106.025202

[16] A. B. Zylstra, O. A. Hurricane, D. A. Callahan *et al.*, Nature **601** (2022) 542–548, ISSN 0028-0836, doi:10.1038/s41586-021-04281-w, URL https://www.nature.com/articles/s41586-021-04281-w

[17] L. Spitzer, Physics of Fluids **1** (1958) 253, ISSN 00319171, doi:10.1063/1.1705883, URL https://pubs.aip.org/aip/pfl/article/1/4/253-264/941214

[18] P. Lobner, *Return of the Stellarator* (2020), URL https://lynceans.org/tag/stellarator/

[19] G. Grieger, H. Renner, and H. Wobig, Nuclear Fusion **25** (1985) 1231–1242, ISSN 0029-5515, doi:10.1088/0029-5515/25/9/040, URL https://iopscience.iop.org/article/10.1088/0029-5515/25/9/040

[20] R. Arnoux, *Which was the first "tokamak"—or was it "tokomag"?* (2008), URL https://www.iter.org/newsline/55/1194

[21] N. J. Peacock, D. C. Robinson, M. J. Forrest *et al.*, Nature **224** (1969) 488–490, ISSN 0028-0836, doi:10.1038/224488a0, URL https://www.nature.com/articles/224488a0

[22] B. B. Kadomtsev, Physics-Uspekhi **39** (1996) 419–427, ISSN 1063-7869, doi:10.1070/PU1996v039n05ABEH000143, URL https://iopscience.iop.org/article/10.1070/PU1996v039n05ABEH000143

[23] A. D. Sakharov, *Теория магнитного термоядерного реактора*, volume 93 (1967), doi:10.3367/UFNr.0093.196711p.0564, URL https://ufn.ru/ru/articles/1967/11/p/

[24] F. Mink, *Structure and Nonlinear Development of Edge Localized Magnetohydrodynamic Instabilities on the ASDEX Upgrade Tokamak*, Ph.D. thesis, Technische Universität München (2018)

[25] H. Zohm, *Magnetohydrodynamic Stability of Tokamaks*, Wiley (2014), ISBN 9783527412327, doi:10.1002/9783527677375, URL https://onlinelibrary.wiley.com/doi/book/10.1002/9783527677375

[26] V. D. Shafranov, Journal of Nuclear Energy. Part C, Plasma Physics, Accelerators, Thermonuclear Research **5** (1963) 251–258, ISSN 0368-3281, doi:10.1088/0368-3281/5/4/307, URL https://iopscience.iop.org/article/10.1088/0368-3281/5/4/307

[27] F. Wagner, G. Becker, K. Behringer *et al.*, Physical Review Letters **49** (1982) 1408–1412, ISSN 0031-9007, doi:10.1103/PhysRevLett.49.1408, URL https://link.aps.org/doi/10.1103/PhysRevLett.49.1408

[28] M. Keilhacker, G. Becker, K. Bernhardi *et al.*, Plasma Physics and Controlled Fusion **26** (1984) 49–63, ISSN 0741-3335, doi:10.1088/0741-3335/26/1A/305, URL https://iopscience.iop.org/article/10.1088/0741-3335/26/1A/305

[29] J. W. Connor and H. R. Wilson, Plasma Physics and Controlled Fusion **42** (2000) R1–R74, ISSN 0741-3335, doi:10.1088/0741-3335/42/1/201, URL https://iopscience.iop.org/article/10.1088/0741-3335/42/1/201

[30] U. Plank, R. McDermott, G. Birkenmeier *et al.*, Plasma Physics and Controlled Fusion **65** (2023) 014001, ISSN 0741-3335, doi:10.1088/1361-6587/aca35b, URL https://iopscience.iop.org/article/10.1088/1361-6587/aca35b

[31] F. Wagner, G. Fussmann, T. Grave *et al.*, Physical Review Letters **53** (1984) 1453–1456, ISSN 0031-9007, doi:10.1103/PhysRevLett.53.1453, URL https://link.aps.org/doi/10.1103/PhysRevLett.53.1453

[32] M. Keilhacker, Nuclear Fusion **25** (1985) 1045–1054, ISSN 0029-5515, doi:10.1088/0029-5515/25/9/008, URL https://iopscience.iop.org/article/10.1088/0029-5515/25/9/008

[33] M.-P.-I. fuer Plasmaphysik, *Fusionsanlage ASDEX Upgrade*, URL https://www.ipp.mpg.de/987591/AUG{_}deutsch.pdf

[34] U. Stroth, D. Aguiam, E. Alessi *et al.*, Nuclear Fusion **62** (2022) 042006, ISSN 0029-5515, doi:10.1088/1741-4326/ac207f, URL https://iopscience.iop.org/article/10.1088/1741-4326/ab2211

[35] A. Stäbler, J. Sielanko, S. Götz *et al.*, Fusion Technology **26** (1994) 145–152, ISSN 0748-1896, doi:10.13182/FST94-A30338, URL https://www.tandfonline.com/doi/full/10.13182/FST94-A30338

[36] R. Neu, A. Kallenbach, M. Balden *et al.*, Journal of Nuclear Materials **438** (2013) S34–S41, ISSN 00223115, doi:10.1016/j.jnucmat.2013.01.006, URL https://linkinghub.elsevier.com/retrieve/pii/S0022311513000147

[37] E. R. Solano, E. Delabie, G. Birkenmeier *et al.*, Nuclear Fusion **62** (2022) 076026, ISSN 0029-5515, doi:10.1088/1741-4326/ac4ed8, URL https://iopscience.iop.org/article/10.1088/1741-4326/ac4ed8

[38] D. A. D'Ippolito, J. Myra, and S. J. Zweben, Physics of Plasmas **18** (2011) 060501, ISSN 1070-664X, doi:10.1063/1.3594609, URL http://aip.scitation.org/doi/10.1063/1.3594609

[39] N. Ben Ayed, A. Kirk, B. Dudson *et al.*, Plasma Physics and Controlled Fusion **51** (2009) 035016, ISSN 0741-3335, doi:10.1088/0741-3335/51/3/035016, URL https://iopscience.iop.org/article/10.1088/0741-3335/51/3/035016

[40] M. Griener, E. Wolfrum, G. Birkenmeier *et al.*, Nuclear Materials and Energy **25** (2020) 100854, ISSN 23521791, doi:10.1016/j.nme.2020.100854, URL http://www.sciencedirect.com/science/article/pii/S2352179120301204

[41] G. Birkenmeier, *Structure formation at the edge of high temperature plasmas*, Habilitation, Technische Universität München (2022)

[42] U. Stroth, *Plasmaphysik*, Springer Berlin Heidelberg, Berlin, Heidelberg, 2nd edition (2018), ISBN 978-3-662-55235-3, doi:10.1007/978-3-662-55236-0, URL http://link.springer.com/10.1007/978-3-662-55236-0

[43] P. Stangeby, *The Plasma Boundary of Magnetic Fusion Devices*, CRC Press, Bristol and Philadelphia, plasma phy edition (2000), ISBN 9780367801489, doi:10.1201/9780367801489, URL https://www.taylorfrancis.com/books/9781420033328

[44] L. Spitzer and R. Härm, Physical Review **89** (1953) 977–981, ISSN 0031-899X, doi:10.1103/PhysRev.89.977, URL https://link.aps.org/doi/10.1103/PhysRev.89.977

[45] M. Faitsch, *Divertor power load studies in ASDEX Upgrade and TCV*, Ph.D. thesis, Ludwig–Maximilians–Universität München (2018)

[46] S. Díaz Esteban, M. Griener, E. Wolfrum *et al.*, Plasma Physics and Controlled Fusion ISSN 0741-3335, doi:10.1088/1361-6587/ad106e, URL https://iopscience.iop.org/article/10.1088/1361-6587/ad106e

[47] H.-J. Sun, E. Wolfrum, T. Eich *et al.*, Plasma Physics and Controlled Fusion **57** (2015) 125011, ISSN 0741-3335, doi:10.1088/0741-3335/57/12/125011, URL https://iopscience.iop.org/article/10.1088/0741-3335/57/12/125011

[48] M. Faitsch, B. Sieglin, T. Eich *et al.*, Plasma Physics and Controlled Fusion **57** (2015) 075005, ISSN 0741-3335, doi:10.1088/0741-3335/57/7/075005, URL https://iopscience.iop.org/article/10.1088/0741-3335/57/7/075005

[49] T. Eich, A. Leonard, R. A. Pitts *et al.*, Nuclear Fusion **53** (2013) 093031, ISSN 0029-5515, doi:10.1088/0029-5515/53/9/093031, URL https://iopscience.iop.org/article/10.1088/0029-5515/53/9/093031

[50] R. A. Pitts, S. Carpentier, F. Escourbiac *et al.*, Journal of Nuclear Materials **438** (2013) S48–S56, ISSN 00223115, doi:10.1016/j.jnucmat.2013.01.008, URL https://linkinghub.elsevier.com/retrieve/pii/S0022311513000160

[51] A. Herrmann, T. Eich, S. Jachmich *et al.*, Journal of Nuclear Materials **313-316** (2003) 759–767, ISSN 00223115, doi:10.1016/S0022-3115(02)01422-8, URL https://linkinghub.elsevier.com/retrieve/pii/S0022311502014228

[52] T. Eich, B. Sieglin, A. Thornton *et al.*, Nuclear Materials and Energy **12** (2017) 84–90, ISSN 23521791, doi:10.1016/j.nme.2017.04.014, URL https://linkinghub.elsevier.com/retrieve/pii/S2352179116302927

[53] R. A. Pitts, J. P. Coad, D. Coster *et al.*, Plasma Physics and Controlled Fusion **47**, ISSN 07413335, doi:10.1088/0741-3335/47/12B/S22

[54] F. Maviglia, M. Siccinio, C. Bachmann *et al.*, Nuclear Materials and Energy **26** (2021) 100897, ISSN 23521791, doi:10.1016/j.nme.2020.100897, URL https://linkinghub.elsevier.com/retrieve/pii/S2352179120301587

[55] M. Bernert, S. Wiesen, O. Février *et al.*, Nuclear Materials and Energy **34** (2023) 101376, ISSN 23521791, doi:10.1016/j.nme.2023.101376, URL https://linkinghub.elsevier.com/retrieve/pii/S2352179123000157

[56] T. Pütterich, E. Fable, R. Dux *et al.*, Nuclear Fusion **59** (2019) 056013, ISSN 0029-5515, doi:10.1088/1741-4326/ab0384, URL https://iopscience.iop.org/article/10.1088/1741-4326/ab0384

[57] S. I. Krasheninnikov, A. S. Kukushkin, and A. A. Pshenov, Physics of Plasmas **23**, ISSN 1070-664X, doi:10.1063/1.4948273, URL https://pubs.aip.org/pop/article/23/5/055602/964531/Divertor-plasma-detachment

[58] S. J. Zweben, J. A. Boedo, O. Grulke *et al.*, Plasma Physics and Controlled Fusion **49** (2007) S1–S23, ISSN 0741-3335, doi:10.1088/0741-3335/49/7/S01, URL https://iopscience.iop.org/article/10.1088/0741-3335/49/7/S01

[59] H. Zohm, Plasma Physics and Controlled Fusion **38** (1996) 105–128, ISSN 0741-3335, doi:10.1088/0741-3335/38/2/001, URL https://iopscience.iop.org/article/10.1088/0741-3335/38/2/001

[60] P. Manz, T. T. Ribeiro, B. D. Scott *et al.*, Physics of Plasmas **22**, ISSN 1070-664X, doi:10.1063/1.4908272, URL https://pubs.aip.org/pop/article/22/2/022308/109878/Origin-and-turbulence-spreading-of-plasma-blobs

[61] P. Manz, *The Microscopic Picture of Plasma Edge Turbulence*, Habilitation, Technische Universität München (2018)

[62] M. Spolaore, N. Vianello, M. Agostini *et al.*, Physical Review Letters **102** (2009) 165001, ISSN 0031-9007, doi:10.1103/PhysRevLett.102.165001, URL https://link.aps.org/doi/10.1103/PhysRevLett.102.165001

[63] G. Harrer, M. Faitsch, L. Radovanovic *et al.*, Physical Review Letters **129** (2022) 165001, ISSN 0031-9007, doi:10.1103/PhysRevLett.129.165001, 2110.12664, URL https://link.aps.org/doi/10.1103/PhysRevLett.129.165001

[64] G. Harrer, E. Wolfrum, M. Dunne *et al.*, Nuclear Fusion **58** (2018) 112001, ISSN 0029-5515, doi:10.1088/1741-4326/aad757, URL https://iopscience.iop.org/article/10.1088/1741-4326/aad757

[65] J. Stober, P. Lomas, G. Saibene *et al.*, Nuclear Fusion **45** (2005) 1213–1223, ISSN 0029-5515, doi:10.1088/0029-5515/45/11/001, URL https://iopscience.iop.org/article/10.1088/0029-5515/45/11/001

[66] N. Leuthold, W. Suttrop, R. Fischer *et al.*, Plasma Physics and Controlled Fusion **59** (2017) 055004, ISSN 0741-3335, doi:10.1088/1361-6587/aa5f70, URL https://iopscience.iop.org/article/10.1088/1361-6587/aa5f70

[67] E. Viezzer, M. Austin, M. Bernert *et al.*, Nuclear Materials and Energy **34** (2023) 101308, ISSN 23521791, doi:10.1016/j.nme.2022.101308, URL https://linkinghub.elsevier.com/retrieve/pii/S2352179122001892

[68] J. W. Connor, Plasma Physics and Controlled Fusion **40** (1998) 531–542, ISSN 0741-3335, doi:10.1088/0741-3335/40/5/002, URL https://iopscience.iop.org/article/10.1088/0741-3335/40/5/002

[69] L. Radovanovic, M. Dunne, E. Wolfrum *et al.*, Nuclear Fusion **62** (2022) 086004, ISSN 0029-5515, doi:10.1088/1741-4326/ac6d6a, URL https://iopscience.iop.org/article/10.1088/1741-4326/ac6d6a

[70] G. Fuchert, G. Birkenmeier, D. Carralero *et al.*, Plasma Physics and Controlled Fusion **56** (2014) 125001, ISSN 0741-3335, doi:10.1088/0741-3335/56/12/125001, URL https://iopscience.iop.org/article/10.1088/0741-3335/56/12/125001

[71] D. G. Whyte, A. E. Hubbard, J. W. Hughes *et al.*, Nuclear Fusion **50** (2010) 105005, ISSN 0029-5515, doi:10.1088/0029-5515/50/10/105005, URL https://iopscience.iop.org/article/10.1088/0029-5515/50/10/105005

[72] F. Ryter, R. Fischer, J. C. Fuchs *et al.*, Nuclear Fusion **57** (2017) 016004, ISSN 0029-5515, doi:10.1088/0029-5515/57/1/016004, URL https://iopscience.iop.org/article/10.1088/0029-5515/57/1/016004

[73] T. Happel, M. Griener, D. Silvagni *et al.*, Nuclear Materials and Energy **18** (2019) 159–165, ISSN 23521791, doi:10.1016/j.nme.2018.12.022, URL https://doi.org/10.1016/j.nme.2018.12.022

[74] R. Bielajew, G. D. Conway, M. Griener *et al.*, Physics of Plasmas **29** (2022) 052504, ISSN 1070-664X, doi:10.1063/5.0088062, URL https://pubs.aip.org/aip/pop/article/2847917

[75] G. D. Conway, C. Angioni, F. Ryter *et al.*, Physical Review Letters **106** (2011) 065001, ISSN 0031-9007, doi:10.1103/PhysRevLett.106.065001, URL https://link.aps.org/doi/10.1103/PhysRevLett.106.065001

[76] E. R. Solano, N. Vianello, E. Delabie *et al.*, Nuclear Fusion **57** (2017) 022021, ISSN 0029-5515, doi:10.1088/0029-5515/57/2/022021, URL https://iopscience.iop.org/article/10.1088/0029-5515/57/2/022021

[77] D. Réfy, E. R. Solano, N. Vianello *et al.*, Nuclear Fusion **60** (2020) 056004, ISSN 0029-5515, doi:10.1088/1741-4326/ab7594, URL https://iopscience.iop.org/article/10.1088/1741-4326/ab7594

[78] K. Itoh, S.-I. Itoh, and A. Fujisawa, Plasma and Fusion Research **8** (2013) 1102168–1102168, ISSN 1880-6821, doi:10.1585/pfr.8.1102168, URL https://www.jstage.jst.go.jp/article/pfr/8/0/8{_}1102168/{_}article

[79] G. Birkenmeier, M. Cavedon, G. D. Conway *et al.*, Nuclear Fusion **56** (2016) 086009, ISSN 0029-5515, doi:10.1088/0029-5515/56/8/086009, URL https://iopscience.iop.org/article/10.1088/0029-5515/56/8/086009

[80] D. Silvagni, J. L. Terry, W. McCarthy *et al.*, Nuclear Fusion **62** (2022) 036004, ISSN 0029-5515, doi:10.1088/1741-4326/ac4296, URL https://iopscience.iop.org/article/10.1088/1741-4326/ac4296

[81] S. I. Krasheninnikov, Physics Letters A **283** (2001) 368–370, ISSN 03759601, doi:10.1016/S0375-9601(01)00252-3, URL https://linkinghub.elsevier.com/retrieve/pii/S0375960101002523

[82] S. I. Krasheninnikov, D. A. D'Ippolito, and J. Myra, Journal of Plasma Physics **74** (2008) 679–717, ISSN 0022-3778, doi:10.1017/S0022377807006940, URL https://www.cambridge.org/core/product/identifier/S0022377807006940/type/journal{_}article

[83] P. Manz, D. Carralero, G. Birkenmeier *et al.*, Physics of Plasmas **20** (2013) 102307, ISSN 1070-664X, doi:10.1063/1.4824799, URL http://aip.scitation.org/doi/10.1063/1.4824799

[84] J. Myra, D. A. Russell, and D. A. D'Ippolito, Physics of Plasmas **13**, ISSN 1070-664X, doi:10.1063/1.2364858, URL https://pubs.aip.org/pop/article/13/11/112502/262030/Collisionality-and-magnetic-geometry-effects-on

[85] N. Offeddu, W. Han, C. Theiler *et al.*, Nuclear Fusion **62** (2022) 096014, ISSN 0029-5515, doi:10.1088/1741-4326/ac7ed7, URL https://iopscience.iop.org/article/10.1088/1741-4326/ac7ed7

[86] N. Vianello, D. Carralero, C. K. Tsui *et al.*, Nuclear Fusion **60** (2020) 016001, ISSN 0029-5515, doi:10.1088/1741-4326/ab423e, URL https://iopscience.iop.org/article/10.1088/1741-4326/ab423e

[87] D. Carralero, M. Siccinio, M. Komm *et al.*, Nuclear Fusion **57** (2017) 056044, ISSN 0029-5515, doi:10.1088/1741-4326/aa64b3, URL https://iopscience.iop.org/article/10.1088/1741-4326/aa64b3

[88] S. J. Zweben, J. L. Terry, D. P. Stotler *et al.*, Review of Scientific Instruments **88** (2017) 041101, ISSN 0034-6748, doi:10.1063/1.4981873, URL http://dx.doi.org/10.1063/1.4981873http://aip.scitation.org/doi/10.1063/1.4981873

[89] C. Killer, B. Shanahan, O. Grulke *et al.*, Plasma Physics and Controlled Fusion **62** (2020) 085003, ISSN 0741-3335, doi:10.1088/1361-6587/ab9313, URL https://iopscience.iop.org/article/10.1088/1361-6587/ab9313

[90] F. M. Laggner, *Electron Density Perturbations at the Plasma Edge of the ASDEX Upgrade Tokamak*, Ph.D. thesis, Technische Universität Wien (2013)

[91] T. Farley, N. R. Walkden, F. Militello *et al.*, Review of Scientific Instruments **90** (2019) 093502, ISSN 0034-6748, doi:10.1063/1.5109470, URL https://doi.org/10.1063/1.5109470http://aip.scitation.org/doi/10.1063/1.5109470

[92] G. Grenfell, J. Adámek, M. Komm *et al.*, Review of Scientific Instruments **93**, ISSN 0034-6748, doi:10.1063/5.0075846, URL https://pubs.aip.org/rsi/article/93/2/023507/2843841/High-heat-flux-ball-pen-probe-head-in-ASDEX

[93] N. Asakura, Y. Koide, K. Itami *et al.*, Journal of Nuclear Materials **241-243** (1997) 559–563, ISSN 00223115, doi:10.1016/S0022-3115(97)80099-2, URL https://linkinghub.elsevier.com/retrieve/pii/S0022311597800992

[94] B. Lipschultz, B. LaBombard, C. S. Pitcher *et al.*, Plasma Physics and Controlled Fusion **44** (2002) 309, ISSN 07413335, doi:10.1088/0741-3335/44/6/309, URL https://iopscience.iop.org/article/10.1088/0741-3335/44/6/309

[95] D. Carralero, G. Birkenmeier, H. Müller *et al.*, Nuclear Fusion **54** (2014) 123005, ISSN 0029-5515, doi:10.1088/0029-5515/54/12/123005, 1407.3618, URL https://iopscience.iop.org/article/10.1088/0029-5515/54/12/123005

[96] D. Carralero, P. Manz, L. Aho-Mantila *et al.*, Physical Review Letters **115** (2015) 215002, ISSN 0031-9007, doi:10.1103/PhysRevLett.115.215002, 1505.07741, URL https://link.aps.org/doi/10.1103/PhysRevLett.115.215002

[97] M. Faitsch, T. Eich, G. Harrer *et al.*, Nuclear Materials and Energy **26** (2021) 100890, ISSN 23521791, doi:10.1016/j.nme.2020.100890, URL https://linkinghub.elsevier.com/retrieve/pii/S2352179120301526

[98] A. Redl, T. Eich, N. Vianello *et al.*, Nuclear Materials and Energy **34** (2023) 101319, ISSN 23521791, doi:10.1016/j.nme.2022.101319, URL https://linkinghub.elsevier.com/retrieve/pii/S2352179122002009

[99] G. Birkenmeier, P. Manz, D. Carralero *et al.*, Nuclear Fusion **55** (2015) 033018, ISSN 0029-5515, doi:10.1088/0029-5515/55/3/033018, URL https://iopscience.iop.org/article/10.1088/0029-5515/55/3/033018

[100] D. L. Rudakov, J. A. Boedo, R. Moyer *et al.*, Nuclear Fusion **45** (2005) 1589–1599, ISSN 0029-5515, doi:10.1088/0029-5515/45/12/014, URL https://iopscience.iop.org/article/10.1088/0029-5515/45/12/014

[101] Y. Nakamura and I. Tsukabayashi, Physical Review Letters **52** (1984) 2356–2359, ISSN 0031-9007, doi:10.1103/PhysRevLett.52.2356, URL https://link.aps.org/doi/10.1103/PhysRevLett.52.2356

[102] A. B. Ehrhardt, H. R. Garner, G. A. Navratil *et al.*, The Physics of Fluids **24** (1981) 1859–1864, ISSN 0031-9171, doi:10.1063/1.863266, URL https://pubs.aip.org/pfl/article/24/10/1859/858957/Cross-field-diffusion-and-fluctuation-spectra-in-a

[103] H. M. Mott-Smith and I. Langmuir, Physical Review **28** (1926) 727–763, ISSN 0031-899X, doi:10.1103/PhysRev.28.727, URL https://link.aps.org/doi/10.1103/PhysRev.28.727

[104] F. Chen, *Lecture notes on Langmuir Probe Diagnostics*, Technical report, University of California, Los Angeles (2003), URL https://citeseerx.ist.psu.edu/document?repid=rep1{&}type=pdf{&}doi=eb0c532a0187a4ea4c2249f1b0d111f8810e5415

[105] B. LaBombard, Physics of Plasmas **9** (2002) 1300–1311, ISSN 1070-664X, doi:10.1063/1.1459060, URL https://pubs.aip.org/pop/article/9/4/1300/265490/An-interpretation-of-fluctuation-induced-transport

[106] E. Calderón, C. Hidalgo, M. A. Pedrosa *et al.*, Review of Scientific Instruments **75** (2004) 4293–4295, ISSN 0034-6748, doi:10.1063/1.1787575, URL https://pubs.aip.org/aip/rsi/article/75/10/4293-4295/1071438

[107] Y. H. Xu, S. Jachmich, R. R. Weynants *et al.*, Plasma Physics and Controlled Fusion **47** (2005) 1841–1855, ISSN 0741-3335, doi:10.1088/0741-3335/47/10/014, URL https://iopscience.iop.org/article/10.1088/0741-3335/47/10/014

[108] C. Ritz, D. Brower, T. L. Rhodes *et al.*, Nuclear Fusion **27** (1987) 1125–1134, ISSN 0029-5515, doi:10.1088/0029-5515/27/7/006, URL https://iopscience.iop.org/article/10.1088/0029-5515/27/7/006

[109] A. J. Wootton, M. Austin, R. Bengtson *et al.*, Plasma Physics and Controlled Fusion **30** (1988) 1479–1491, ISSN 0741-3335, doi:10.1088/0741-3335/30/11/010, URL https://iopscience.iop.org/article/10.1088/0741-3335/30/11/010

[110] S. J. Zweben, The Physics of Fluids **28** (1985) 974–982, ISSN 0031-9171, doi:10.1063/1.865069, URL https://pubs.aip.org/pfl/article/28/3/974/943845/Search-for-coherent-structure-within-tokamak

[111] S. Benkadda, T. D. de Wit, A. Verga *et al.*, Physical Review Letters **73** (1994) 3403–3406, ISSN 0031-9007, doi:10.1103/PhysRevLett.73.3403, URL https://link.aps.org/doi/10.1103/PhysRevLett.73.3403

[112] M. Endler, H. Niedermeyer, L. Giannone *et al.*, Nuclear Fusion **35** (1995) 1307–1339, ISSN 0029-5515, doi:10.1088/0029-5515/35/11/I01, URL https://iopscience.iop.org/article/10.1088/0029-5515/35/11/I01

[113] H. Johnsen, H. L. Pecseli, and J. Trulsen, Physics of Fluids **30** (1987) 2239, ISSN 00319171, doi:10.1063/1.866158, URL https://pubs.aip.org/aip/pfl/article/30/7/2239-2254/844397

[114] D. L. Rudakov, J. A. Boedo, R. A. Moyer *et al.*, Review of Scientific Instruments **72** (2001) 453–456, ISSN 0034-6748, doi:10.1063/1.1310577, URL https://pubs.aip.org/rsi/article/72/1/453/435990/Fast-electron-temperature-diagnostic-based-on

[115] Y. Xu, G. Wang, K. Zhai *et al.*, Physics of Plasmas **3** (1996) 1022–1028, ISSN 1070-664X, doi:10.1063/1.871757, URL https://pubs.aip.org/pop/article/3/3/1022/262908/Electrostatic-fluctuations-and-related-transport

[116] M. Greenwald, Plasma Physics and Controlled Fusion **44** (2002) 201, ISSN 07413335, doi:10.1088/0741-3335/44/8/201, URL https://iopscience.iop.org/article/10.1088/0741-3335/44/8/201

[117] J. A. Boedo, D. L. Rudakov, R. A. Moyer *et al.*, Physics of Plasmas **8** (2001) 4826–4833, ISSN 1070-664X, doi:10.1063/1.1406940, URL https://pubs.aip.org/pop/article/8/11/4826/264893/Transport-by-intermittent-convection-in-the

[118] M. Zuin, S. Dal Bello, L. Marrelli *et al.*, Nuclear Fusion **57** (2017) 102012, ISSN 0029-5515, doi:10.1088/1741-4326/aa61cc, URL https://iopscience.iop.org/article/10.1088/1741-4326/aa61cc

[119] M. Agostini, P. Scarin, R. Cavazzana *et al.*, Review of Scientific Instruments **86**, ISSN 0034-6748, doi:10.1063/1.4939003, URL https://pubs.aip.org/rsi/article/86/12/123513/856059/Fast-Thermal-Helium-Beam-diagnostic-for

[120] R. J. Fonck, D. S. Darrow, and K. P. Jaehnig, Physical Review A **29** (1984) 3288–3309, ISSN 0556-2791, doi:10.1103/PhysRevA.29.3288, URL https://link.aps.org/doi/10.1103/PhysRevA.29.3288

[121] R. C. Isler, Plasma Physics and Controlled Fusion **36** (1994) 171–208, ISSN 0741-3335, doi:10.1088/0741-3335/36/2/001, URL https://iopscience.iop.org/article/10.1088/0741-3335/36/2/001

[122] U. Fantz, Plasma Sources Science and Technology **15** (2006) S137–S147, ISSN 0963-0252, doi:10.1088/0963-0252/15/4/S01, URL https://iopscience.iop.org/article/10.1088/0963-0252/15/4/S01

[123] G. R. McKee, C. Fenzi, R. J. Fonck *et al.*, Review of Scientific Instruments **74** (2003) 2014–2019, ISSN 0034-6748, doi:10.1063/1.1535248, URL https://pubs.aip.org/rsi/article/74/3/2014/939067/Turbulence-imaging-and-applications-using-beam

[124] M. Griener, O. Schmitz, K. Bald *et al.*, Review of Scientific Instruments **88** (2017) 033509, ISSN 0034-6748, doi:10.1063/1.4978629, URL http://dx.doi.org/10.1063/1.4978629http://aip.scitation.org/doi/10.1063/1.4978629

[125] D. Wendler, R. Dux, R. Fischer *et al.*, Plasma Physics and Controlled Fusion ISSN 0741-3335, doi:10.1088/1361-6587/ac49f8, URL https://iopscience.iop.org/article/10.1088/1361-6587/ac49f8

[126] M. Griener, E. Wolfrum, M. Cavedon *et al.*, Review of Scientific Instruments **89** (2018) 10D102, ISSN 0034-6748, doi:10.1063/1.5034446, URL http://aip.scitation.org/doi/10.1063/1.5034446

[127] A. Kramida, Yu. Ralchenko, and J. Reader, *NIST Atomic Spectra Database (ver. 5.6.1)*, National Institute of Standards and Technology, Gaithersburg, MD. (2018), URL https://physics.nist.gov/asd

[128] J. M. Muñoz-Burgos, T. Barbui, O. Schmitz *et al.*, Review of Scientific Instruments **87** (2016) 11E502, ISSN 0034-6748, doi:10.1063/1.4955286, URL http://aip.scitation.org/doi/10.1063/1.4955286

[129] M. Brix, *Messung von Elektronentemperatur und -dichte mittels Heliumstrahldiagnostik im Randschichtplasma eines Tokamaks*, Ph.D. thesis, Ruhr-Universität Bochum (1998)

[130] M. Griener, J. M. Muñoz-Burgos, M. Cavedon *et al.*, Plasma Physics and Controlled Fusion **60** (2018) 025008, ISSN 0741-3335, doi:10.1088/1361-6587/aa97e8, URL https://iopscience.iop.org/article/10.1088/1361-6587/aa97e8

[131] J. M. Muñoz-Burgos, O. Schmitz, S. D. Loch *et al.*, Physics of Plasmas **19** (2012) 012501, ISSN 1070-664X, doi:10.1063/1.3672230, URL http://aip.scitation.org/doi/10.1063/1.3672230

[132] H. P. Summers and M. G. O'Mullane, in *AIP Conference Proceedings*, volume 1344, pages 179–187 (2011), ISBN 9780735409002, ISSN 0094243X, doi:10.1063/1.3585817, URL https://pubs.aip.org/aip/acp/article/1344/1/179-187/803400

[133] B. Schweer, G. Mank, A. Pospieszczyk *et al.*, Journal of Nuclear Materials **196-198** (1992) 174–178, ISSN 00223115, doi:10.1016/S0022-3115(06)80026-7, URL https://linkinghub.elsevier.com/retrieve/pii/S0022311506800267

[134] D. Wendler, G. Birkenmeier, M. Griener *et al.*, Physics of Plasmas **30**, ISSN 1070-664X, doi:10.1063/5.0164057, URL https://pubs.aip.org/pop/article/30/9/092509/2911597/Two-dimensional-reconstruction-of-filament

[135] J. Burkardt, *QUADMOM* (2017), URL https://people.sc.fsu.edu/{~}jburkardt/c{_}src/quadmom/quadmom.html

[136] R. Fischer, J. C. Fuchs, B. Kurzan *et al.*, Fusion Science and Technology **58** (2010) 675–684, ISSN 1536-1055, doi:10.13182/FST10-110, URL https://www.tandfonline.com/doi/full/10.13182/FST10-110

[137] B. Vanovac, S. Denk, E. Wolfrum *et al.*, EPJ Web of Conferences **203** (2019) 02011, ISSN 2100-014X, doi:10.1051/epjconf/201920302011, URL https://www.epj-conferences.org/10.1051/epjconf/201920302011

[138] H. J. Hartfuss, T. Geist, and M. Hirsch, Plasma Physics and Controlled Fusion **39** (1997) 1693–1769, ISSN 0741-3335, doi:10.1088/0741-3335/39/11/001, URL https://iopscience.iop.org/article/10.1088/0741-3335/39/11/001

[139] A. J. Lichtenberg, S. Sesnic, and A. W. Trivelpiece, Physical Review Letters **13** (1964) 387–388, ISSN 0031-9007, doi:10.1103/PhysRevLett.13.387, URL https://link.aps.org/doi/10.1103/PhysRevLett.13.387

[140] I. H. Hutchinson, *Principles of Plasma Diagnostics*, Cambridge University Press, 2nd edition (2002), ISBN 9780521803892, doi:10.1017/CBO9780511613630, URL https://www.cambridge.org/core/product/identifier/9780511613630/type/book

[141] K. Kadota, K. Tsuchida, Y. Kawasumi *et al.*, Plasma Physics **20** (1978) 1011–1023, ISSN 0032-1028, doi:10.1088/0032-1028/20/10/004, URL https://iopscience.iop.org/article/10.1088/0032-1028/20/10/004

[142] M. Willensdorfer, G. Birkenmeier, R. Fischer *et al.*, Plasma Physics and Controlled Fusion **56** (2014) 025008, ISSN 0741-3335, doi:10.1088/0741-3335/56/2/025008, URL https://iopscience.iop.org/article/10.1088/0741-3335/56/2/025008

[143] A. Mlynek, G. Schramm, H. Eixenberger *et al.*, Review of Scientific Instruments **81** (2010) 033507, ISSN 0034-6748, doi:10.1063/1.3340944, URL http://aip.scitation.org/doi/10.1063/1.3340944

[144] W. von der Linden, V. Dose, and U. von Toussaint, *Bayesian Probability Theory*, Cambridge University Press (2014), ISBN 9781139565608, doi:10.1017/CBO9781139565608, URL https://www.cambridge.org/core/product/identifier/9781139565608/type/book

[145] R. Fischer, A. Bock, S. Denk *et al.*, submitted to Nuclear Fusion ITER Special Issue

[146] R. Fischer, E. Wolfrum, and J. Schweinzer, Plasma Physics and Controlled Fusion **50** (2008) 085009, ISSN 0741-3335, doi:10.1088/0741-3335/50/8/085009, URL https://iopscience.iop.org/article/10.1088/0741-3335/50/8/085009

[147] M. Bergmann, R. Fischer, C. Angioni *et al.*, Nuclear Fusion **64** (2024) 056024, ISSN 0029-5515, doi:10.1088/1741-4326/ad3138, URL https://iopscience.iop.org/article/10.1088/1741-4326/ad3138

[148] P. J. McCarthy, Physics of Plasmas **6** (1999) 3554–3560, ISSN 1070-664X, doi:10.1063/1.873630, URL http://aip.scitation.org/doi/10.1063/1.873630

[149] P. J. McCarthy, P. Martin, and W. Schneider, *The CLISTE Interpretive Equilibrium Code*, Technical report, Max-Planck-Institut für Plasmaphysik., Garching bei München (1999), URL https://hdl.handle.net/11858/00-001M-0000-0027-6023-D

[150] R. Fischer, A. Bock, M. Dunne *et al.*, Fusion Science and Technology **69** (2016) 526–536, ISSN 1536-1055, doi:10.13182/FST15-185, URL https://www.tandfonline.com/doi/full/10.13182/FST15-185

[151] R. Fischer, A. Bock, A. Burckhart *et al.*, Nuclear Fusion **59** (2019) 056010, ISSN 0029-5515, doi:10.1088/1741-4326/ab0b65, URL https://iopscience.iop.org/article/10.1088/1741-4326/ab0b65

[152] E. Strumberger and M. Hölzl, *User Manual: Iterative Computation of 3D Ideal MHD Equilibria and Magnetic Fields*, Technical report, Max-Planck-Institut für Plasmaphysik., Garching bei München (2005), URL https://hdl.handle.net/11858/00-001M-0000-0027-16AA-6

[153] D. P. Stotler, S. Ku, S. J. Zweben *et al.*, Physics of Plasmas **27**, ISSN 1070-664X, doi:10.1063/5.0002876, URL https://pubs.aip.org/pop/article/27/6/062512/153574/Examination-of-synthetic-gas-puff-imaging

[154] E. de la Cal, Nuclear Fusion **56** (2016) 106031, ISSN 0029-5515, doi:10.1088/0029-5515/56/10/106031, URL https://iopscience.iop.org/article/10.1088/0029-5515/56/10/106031

[155] E. Brochu, V. M. Cora, and N. de Freitas, *A Tutorial on Bayesian Optimization of Expensive Cost Functions, with Application to Active User Modeling and Hierarchical Reinforcement Learning* (2010), doi:10.48550/ARXIV.1012.2599, URL https://arxiv.org/abs/1012.2599

[156] T. Zwettler, *Effect of calibration uncertainties on the evaluated electron density and temperature profiles from the thermal helium beam diagnostic*, Master, Technische Universität Wien (2019)

[157] C. Wüthrich, C. Theiler, N. Offeddu *et al.*, Nuclear Fusion **62** (2022) 106022, ISSN 0029-5515, doi:10.1088/1741-4326/ac8692, 2203.10907, URL https://iopscience.iop.org/article/10.1088/1741-4326/ac8692

[158] A. Coroado and P. Ricci, Physics of Plasmas **29** (2022) 032511, ISSN 1070-664X, doi:10.1063/5.0077336, URL https://pubs.aip.org/pop/article/29/3/032511/2847874/Numerical-simulations-of-gas-puff-imaging-using-a

[159] G. Grenfell, P. Manz, G. D. Conway *et al.*, Nuclear Materials and Energy **33** (2022) 101277, ISSN 23521791, doi:10.1016/j.nme.2022.101277, URL https://linkinghub.elsevier.com/retrieve/pii/S2352179122001582

[160] O. Grulke, J. L. Terry, B. LaBombard *et al.*, Physics of Plasmas **13** (2006) 012306, ISSN 1070-664X, doi:10.1063/1.2164991, URL http://aip.scitation.org/doi/10.1063/1.2164991

[161] G. Xu, V. Naulin, W. Fundamenski *et al.*, Nuclear Fusion **49** (2009) 092002, ISSN 0029-5515, doi:10.1088/0029-5515/49/9/092002, URL https://iopscience.iop.org/article/10.1088/0029-5515/49/9/092002

[162] G. S. Kirnev, V. P. Budaev, S. A. Grashin *et al.*, Plasma Physics and Controlled Fusion **46** (2004) 621–637, ISSN 0741-3335, doi:10.1088/0741-3335/46/4/004, URL https://iopscience.iop.org/article/10.1088/0741-3335/46/4/004

[163] H. Johnsen, H. L. Pecseli, and J. Trulsen, Plasma Physics and Controlled Fusion **28** (1986) 1519, doi:10.1088/0741-3335/28/9B/008, URL https://dx.doi.org/10.1088/0741-3335/28/9B/008

[164] S. J. Zweben, M. Lampert, and J. Myra, Physics of Plasmas **29**, ISSN 1070-664X, doi:10.1063/5.0097282, URL https://pubs.aip.org/pop/article/29/7/072504/2844209/Temporal-structure-of-blobs-in-NSTX

[165] M. Kočan, J. Gunn, M. Komm *et al.*, Review of Scientific Instruments **79**, ISSN 0034-6748, doi:10.1063/1.2955465, URL https://pubs.aip.org/rsi/article/79/7/073502/350639/On-the-reliability-of-scrape-off-layer-ion

[166] M. Kočan, F. P. Gennrich, A. Kendl *et al.*, Plasma Physics and Controlled Fusion **54** (2012) 085009, ISSN 0741-3335, doi:10.1088/0741-3335/54/8/085009, URL https://iopscience.iop.org/article/10.1088/0741-3335/54/8/085009

[167] D. A. D'Ippolito, J. Myra, and S. I. Krasheninnikov, Physics of Plasmas **9** (2002) 222–233, ISSN 1070-664X, doi:10.1063/1.1426394, URL https://pubs.aip.org/pop/article/9/1/222/264980/Cross-field-blob-transport-in-tokamak-scrape-off

[168] D. Carralero, S. Artene, M. Bernert *et al.*, Nuclear Fusion **58** (2018) 096015, ISSN 0029-5515, doi:10.1088/1741-4326/aacb04, URL https://iopscience.iop.org/article/10.1088/1741-4326/aacb04

[169] D. A. D'Ippolito and J. Myra, Physics of Plasmas **10** (2003) 4029–4039, ISSN 1070-664X, doi:10.1063/1.1606447, URL https://pubs.aip.org/pop/article/10/10/4029/458372/Blob-stability-and-transport-in-the-scrape-off

[170] C. Spearman, The American Journal of Psychology **18** (1907) 161, ISSN 00029556, doi:10.2307/1412408, URL https://www.jstor.org/stable/1412408?origin=crossref

[171] W. Zholobenko, J. Pfennig, A. Stegmeir *et al.*, Nuclear Materials and Energy **34** (2023) 101351, ISSN 23521791, doi:10.1016/j.nme.2022.101351, URL https://linkinghub.elsevier.com/retrieve/pii/S2352179122002320

Author's publications

ORCID ID: 0000-0002-8838-0137

First author:

- D. Wendler, R. Dux, R. Fischer et al., Plasma Physics and Controlled Fusion ISSN 0741-3335, doi:10.1088/1361-6587/ac49f8, URL https://iopscience.iop.org/article/10.1088/1361-6587/ac49f8
- D. Wendler, G. Birkenmeier, M. Griener et al., Physics of Plasmas 30, ISSN 1070-664X, doi:10.1063/5.0164057, URL https://doi.org/10.1063/5.0164057

Co-author:

- R. Bielajew, G. D. Conway, M. Griener et al., Physics of Plasmas 29 (2022) 052504, ISSN 1070-664X, doi:10.1063/5.0088062, URL https://pubs.aip.org/aip/pop/article/2847917
- S. Diaz Esteban, M. Griener, E. Wolfrum et al., Plasma Physics and Controlled Fusion ISSN 0741-3335, doi:10.1088/1361-6587/ad106e, URL https://iopscience.iop.org/article/10.1088/1361-6587/ad106e
- M. Griener, E. Wolfrum, G. Birkenmeier et al., Nuclear Materials and Energy 25 (2020) 100854, ISSN 23521791, doi:10.1016/j.nme.2020.100854, URL https://doi.org/10.1016/j.nme.2020.100854
- M. Griener, J. Kalis, D. Wendler et al., Nuclear Materials and Energy 34 (2023) 101346, ISSN 23521791, doi:10.1016/j.nme.2022.101346, URL https://linkinghub.elsevier.com/retrieve/pii/S2352179122002277
- J. Kalis, G. Birkenmeier, P. Manz et al., Nuclear Fusion ISSN 0029-5515, doi:10.1088/1741-4326/ad0d32, URL https://doi.org/10.1088/1741-4326/ad0d32
- T. Nishizawa, M. Griener, R. Dux et al., Review of Scientific Instruments 92 (2021) 1–8, ISSN 10897623, doi:10.1063/5.0062436, URL https://doi.org/10.1063/5.0062436
- T. Nishizawa, P. Manz, G. Grenfell et al., Physics of Plasmas 29 (2022) 1–8, ISSN 1070-664X, doi:10.1063/5.0098294, URL https://doi.org/10.1063/5.0098294
- M. Usoltceva, S. Heuraux, H. Faugel et al., Fusion Engineering and Design 192 (2023) 113783, ISSN 09203796, doi:10.1016/j.fusengdes.2023.113783, URL https://doi.org/10.1016/j.fusengdes.2023.113783

Danksagung

Auf dem Weg zu dieser Dissertation möchte ich mich besonders bei einigen Personen bedanken, die mir diesen Weg ermöglicht haben und mich dabei unterstützt haben.

Zuallererst möchte ich mich bei meinen beiden Betreuern Michael Griener und Gregor Birkenmeier bedanken. Ohne sie wäre diese Arbeit nie entstanden und so weit gekommen. Danke für die super Betreuung, das immer offene Ohr, das Ertragen meiner Formulierungsschwäche, den Glauben an das Projekt, euer Fachwissen, eure Hilfe und euren Humor. Neben all dem gibt es noch so viele andere Punkte, in denen ihr mich persönlich, beruflich und in meiner Doktorarbeit weitergebracht habt. Ohne sie alle aufzählen zu können, einfach nur Danke!

Die meiste Zeit hatte ich die Möglichkeit im Bereich von Ulrich Stroth zu arbeiten, der immer einen kritischen und konstruktiven Blick auf die Arbeit hatte. Durch seine Erfahrung und die Quartalsgespräche hat er dazu beigetragen, diese Dissertation auf den richtigen Weg zu bringen. Ebenso möchte ich mich bei meiner neuen Bereichsleiterin Rachael McDermott für ihre Unterstützung am Ende der Arbeit bedanken.

Bei meiner Gruppenleiterin Elisabeth Wolfrum möchte ich mich für die fruchtbaren, inspirierenden und hilfreichen Diskussionen und Inputs bedanken, die mich immer weitergebracht haben. Zusammen mit der Pedestal Physics Gruppe, mit ihrer Kritik und Unterstützung zu meinem Projekt, hat mir das sehr geholfen. Mit Hilfe von Ralph Dux, Rainer Fischer und Dirk Stieglitz konnte ich das Stoß-Strahlungsmodell modifizieren und so die Filamentrekonstruktion erfolgreich entwickeln. Vielen Dank für diese Hilfe und all die kleinen und großen Punkte, die mich auf diesem Weg weitergebracht haben.

Während der nicht-Lockdown Zeit, hatte ich das Vergnügen mit Pilar Cano Megias und Sebastian Hörmann im gleichen Büro zu sein. Die beiden haben mir bei vielen kleinen Sachen geholfen, und das gemeinsame Lachen hat viel Arbeit angenehmer gemacht. Besonders möchte ich mich aber bei Klara Höfler bedanken, die die längste Zeit meine Bürokollegin war, und die neben all den kleinen und großen Hilfen immer für eine gute Stimmung im Büro gesorgt hat. Zusammen mit Michael Bergmann, Jonas Puchmayr, Christian Schuster und Benedikt Zimmermann bin ich ihr für die Unterstützung während meiner Doktorandenzeit, den kritischen und hilfreichen Blick von aussen auf mein Thema und die schönen Zeit die man am Institut, auf Konferenzen und nach der Arbeit verbracht hat dankbar.

Innerhalb meiner Doktorandenzeit war ich Teil des ASDEX Upgrade Teams. Insbesonders Arne Kallenbach, Matthias Bernert, Aleander Bock, Dominik Brida, Mike Dunne, Thomas Eich, Michael Faitsch, Luis Gil, Thomas Pütterich, Francesco Sciortino, Davide Silvagni, Philip Schneider und Matthias Willensdorfer haben mir, neben den anderen Teammitgliedern, besonders geholfen. Danke für die krit-

ischen Diskussionen, die Unterstützung bei den Experimenten, die Datenauswertung und das produktive Umfeld. Für die technische Unterstützung während meiner Doktorandenzeit möchte ich mich bei den AUG-Technikern bedanken, insbesondere bei Michael Ebner und Andreas Bollandt.

Die Zeit am IPP war auch deshalb so angenehm, weil ich mit Magdalena Bauer, Tabea Gleiter, Vanessa Harnisch, Paul Heinrich, Manuel Herschel, Lea Hollendonner, Joey Kalis, David Kulla, Michaela Mayer, Andreas Redl, Raphael Schramm, Michael Sieben und Fabian Solfronk Mittag essen gehen konnte. Danke für die tolle Zeit, das Tratschen am Mittagessen, die Diskussionen in der Kaffepause und das tolle Weihnachtsfeiervideo.

Zuletzt möchte ich mich bei meinen Eltern Martina und Roland Wendler, sowie bei meinem Bruder Lukas bedanken, die mich auf meinem gesamten Weg unterstützt haben !